Investigation of Hypersonic Retropropulsion using Planar Laser-Induced Iodine Fluorescence

---

A Dissertation

Presented to

the faculty of the School of Engineering and Applied Science

University of Virginia

In partial fulfillment of the requirements for the degree

Doctor of Philosophy of Mechanical and Aerospace Engineering

by

Joshua R. Codoni

May, 2014

APPROVAL SHEET

The dissertation is submitted in partial fulfillment of the requirements for the degree of

Doctor of Philosophy

Joshua R. Codoni
AUTHOR

The dissertation has been read and approved by the examining committee:

James McDaniel
ADVISOR

Harsha Chelliah

Kevin Lehmann

Houston Wood

Chris Goyne

Scott Berry

Accepted for the School of Engineering and Applied Science:

Dean, School of Engineering and Applied Science

May, 2014

ABSTRACT

The upper limits of currently available technology to adequately slow high mass Mars entry systems during the entry, descent, and landing phase of missions are quickly being approached. Supersonic/hypersonic retropropulsion is one method being considered to bridge the technology gap to decelerate proposed high mass systems. However, the majority of work enhancing our understanding of the complex interaction of a supersonic or hypersonic freestream interacting with a retrorocket was conducted in the 1960s and 1970s, and limited in scope. Renewed interest has indicated the need to better understand fundamental aerodynamics of the flow, as well as extend the knowledge-base of possible retropropulsion configurations.

The following work utilizes a non-intrusive optical diagnostic technique, planar laser-induced fluorescence with iodine as the fluorescing species, to obtain qualitative planar visualizations for a range of thrust conditions, quantitative 2D velocity, and temperature for a central single-nozzle propulsive decelerator jet and novel peripheral quad-nozzle propulsive decelerator jet configuration in Mach 12 freestream flow. Quantitative planar propulsive decelerator jet mole fraction was also measured for the quad-nozzle configuration in Mach 12 freestream flow. This work provides a unique data set useful for computational verification and validation, and furthers the understanding of fundamental aerodynamics associated with the highly complex flowfield. Experimental measurements will be compared with computational fluid dynamics results from the University of Michigan.

ACKNOWLEDGEMENTS

First, I would like to thank my advisor, Professor Jim McDaniel. No matter how bad things have looked in the lab, even when equipment continues to fail for over a year and a half, I have left every meeting with Jim feeling nothing but complete confidence that we will fix it. Jim's patience, reassurance, and guidance with the measurement technique have been outstanding. A big thank you to Dr. Erin Reed, my colleague for over five years at the ARL, Erin is one of the most selfless people I have met, and even after graduating continued to help with edits and revisions to this monster. Thank you to David, a friend who just happens to be taking over the lab from me. I'm not quite sure Dave understands just how great it has been to have a "new" student I could trust to complete projects without my help; Dave, if Lindsey continues to ask how long until you finish, I'm sure Virginia can give her an answer. I can't promise Lindsey will like it. Thank you to my committee for agreeing to serve, and especially for making it a painless process of getting everyone in the same room, during the same block of time – I was told that usually takes a miracle. Also, thank you to everyone at the ARL over the years, especially Brian, Kristin, Mike, and Roger, you have all helped me at some point, and you have definitely made my time in Charlottesville more enjoyable. One special thanks to Gaetano, who was invaluable in helping me use the UVa cluster for my data analysis, and has been a great friend.

I have met some people I consider to be among my best friends during this time. Max, the constant driving force to get everyone off the couch, Pat, who introduced me to the glory of kickball and McGrady's trivia, and Brendyn, who put up with living with me for three years and with whom there are honestly just too many memories to list (yearly Halloween pumpkin carving, Disneyworld, planning for the "inevitable" zombie apocalypse), I really couldn't ask for better friends. To all my friends and family, thank you, this has been quite an experience, and I

wouldn't have finished without support from so many of you. Finally, to Virginia, who had seemingly limitless patience as I kept saying, "I might be able to finish this semester, if…" Well, I'm finally done, I ***finally*** proposed (thanks for saying yes, by the way), and now we can finally go on that backpacking trip.

This work was supported by NASA Hypersonics Project NRA grant NNX08AH37A, with Bryan Palaszewski from the NASA Glenn Research Center as the technical monitor. Further graduate student support from a NASA GSRP fellowship, and VSGC fellowship is greatly appreciated.

TABLE OF CONTENTS

LIST OF FIGURES

LIST OF TABLES

ACRONYMS

EDL	Entry, descent, and Landing
MSL	Mars Science Laboratory
HMMES	High-mass Mars entry systems
SRP	Supersonic retropropulsion
HRP	Hypersonic retropropulsion
PD	Propulsive deceleration
PLIIF	Planar laser-induced iodine fluorescence

LeMANS	CFD code from University of Michigan
CCD	Charge-coupled device
SSD	Shock stand-off distance

NOMENCLATURE

A	=	Empirically determined constant
A_{21}	=	Fluorescence emission rate [s^{-1}]
A_e	=	Exit area of propulsive deceleration jet [m^2]
b_{12}	=	Stimulated rate coefficient [s^{-1}]
B	=	Broadening parameter
c_b	=	Empirically determined broadening constant [GHz $K^{0.7}$ / kPa]
c_p	=	Specific heat of nitrogen at constant pressure [J Kg / K]
c_q	=	Empirically determined constant [$K^{0.5}$ / kPa]
C	=	Fluorescence signal constant
C_T	=	Coefficient of thrust
D	=	Detuning parameter
D	=	Orifice diameter [mm]
E_{ij}	=	Strain tensor [s^{-1}]
f_s	=	Iodine seeding fraction
$f_{J"}$	=	Boltzmann population fraction of rotational ground state
$f_{v"}$	=	Boltzmann population fraction of vibrational ground state
$f_{v",J"}$	=	Boltzmann population fraction
I	=	Laser intensity [W]
k	=	Boltzmann constant [J / K]
M	=	Mach number
n	=	Number density [m^{-3}]
N_1	=	Total population of ground electronic, X, state
N_1	=	Total population of excited electronic, B, state
p	=	Pressure [N / m^2]
T	=	Temperature [K]
T	=	Jet thrust [N]
q	=	Dynamic pressure [N / m^2]
Q	=	Collisional quenching rate [s^{-1}]
S	=	Surface area of aeroshell (Ch. 3) [m^s]
S	=	Uncertainty (Appendix B)
S_F	=	Fluorescence signal
u	=	Velocity [m / s]
V	=	Voigt function
V_x	=	Velocity component in x-direction of lab frame
V_y	=	Velocity component in y-direction of lab frame
x	=	Distance from orifice [mm]
x_0	=	Empirically determined constant [mm]
β	=	Mole fraction ratio constant of proportionality
χ	=	PD jet mole fraction
$\Delta\nu$	=	Detuning from absorption linecenter[GHz]
$\Delta\nu_C$	=	Collisional line width [GHz]

$\Delta\nu_D$	=	Dopper line width [GHz]
$\Delta\nu_{Dop}$	=	Dopper shift [GHz]
$\Delta\nu_I$	=	Impact shift [GHz]
$\Delta\nu_T$	=	Total frequency shift [GHz]
γ	=	Specific heat ratio
λ	=	Wavelength [nm]
ω	=	Vorticity [s^{-1}]
σ	=	Degeneracy of rotational state
θ_i	=	Laser sheet angle in i-direction [deg]
θ_j	=	Laser sheet angle in j-direction [deg]
θ_{rot}	=	Characteristic rotational temperature [K]
θ_{vib}	=	Characteristic vibrational temperature [K]
ν	=	Molecular linecenter frequency [GHz]
$\dot{m}$	=	Mass Flow Rate [kg / s]

Subscripts

∞	=	Freestream conditions
e	=	Jet exit condition

CHAPTER 1: INTRODUCTION

The Mars Science Laboratory (MSL) marked the seventh successful landing on Mars and set new benchmarks for capabilities, such as the heaviest rover to date which was landed with the most precision. One of the most challenging aspects of a Mars mission is the entry, descent, and landing (EDL) phase of the mission. In this portion, the lander must decelerate from hypersonic velocities to low enough speeds to facilitate a successful landing configuration. Unfortunately, the primary methods currently in use for decelerating are not as effective on Mars due to the average atmospheric density only being approximately 1% of Earth's.[1] Due to the low atmospheric density and scalability of current technologies, the upper limits of the current methods in use for landing on Mars – heritage Viking-era techniques, such as a 70-deg sphere-cone blunt body and supersonic parachutes – are quickly being approached.

It is estimated that current capabilities, along with use of yet unproven aerocapture (passing through the upper atmosphere to brake before initiating EDL) can be extended to missions requiring a 1,500 kg payload.[2] However, human missions to Mars will require landed masses one to two orders of magnitude larger.[3] Therefore, it is necessary to research alternative methods for decelerating these high mass Mars entry systems (HMMES). Proposed methods include drag augmentation via hypersonic and supersonic inflatables (trailing ballutes, or an expandable aeroshell) as well as supersonic and hypersonic retropropulsion (SRP & HRP). The latter method is the focus of this research.

SRP and HRP research initially began in the 1950s and continued through the 1970s,[4,5] as a concept to augment the aerodynamics deceleration the vehicle undergoes due to its blunt body shape when it first enters the atmosphere. But the concept was later discarded in the 1970s in favor of simply using a parachute to further slow landers down. Due to materials and sizing limits of parachutes, recently, interest has been renewed for retropropulsion.[6-11] However, previous and renewed experimental efforts in retropropulsion have largely consisted of Schlieren/shadowgraph visualization techniques, pressure taps and surface temperature measurements, which are limited in utility to understand flowfield aerodynamics. Furthermore, most recent research has been for SRP applications. Very recently, NASA has specifically stated that SRP should also be extended into HRP regimes in the entry, descent, and landing roadmap.[6] Obtaining more data, especially quantitative, non-intrusive data, is a crucial step to improve technology beyond current limited capabilities.

The proposed work will use planar laser-induced iodine fluorescence (PLIIF) to obtain 2D visualizations and quantitative temperature and 2D velocity measurements of a single-nozzle, central HRP configuration, as well as novel quad-nozzle configurations. The objective is to better understand the fundamental aerodynamics associated with the highly complex interaction of retropropulsion jets with a Mach 12 freestream. 2D HRP propulsive decelerator (PD) jet mole fraction for the quad-nozzle configurations were investigated and will be reported. Four experimental models were studied: two with a single PD jet located at the stagnation point on the forebody model of a 70-deg blunt body cone; and two with a quad-nozzle design, with four PD jets located off-centerline. Each design, single- and quad-nozzle, was further investigated by the use of sonic, and supersonic PD jets. The resulting high-resolution PLIIF data sets were then used for computational verification and validation, which was also an objective of this work.

1.1 Historical Context

An extensive survey of the available historical literature for SRP/HRP is discussed in Ref. 9. Initial experimental research for retropropulsion in the 1950s did not utilize blunt body geometries and in general focused on the effect of boundary layer transitions due to retrorockets.[12,13] Further work in the mid-50s provided pressure distributions and analysis of flow stability when a retrorocket interacts with a supersonic freestream.[14,15] Throughout the 1960s, blunt bodies equipped with retrorockets, typically a single PD jet at the stagnation point, began to establish the bulk of the experimental data available.[4,5,16,17] The major flow characteristics, shown in Figure 1.1 for a single, centrally located retrorocket, were established: the PD jet plume pushes the bow shock upstream of the model forebody, and a contact surface forms between the bow shock and jet plume. As the post shock freestream and jet plume flow decelerate approaching the contact surface, a free stagnation point forms. For large enough thrust, a recirculation region also forms near model the shoulder (outer edge of aeroshell). Flowfield features such as drag reduction, unsteady effects, heating, model sizing, and PD jet sizing effects, were also studied and partially characterized.[9] Unsteady effects were observed to be dependent on the pressure ratio of the retrorocket and freestream flow, with the flow being stable for low pressure ratios, then transitioning to unstable at larger pressure ratios, and finally back to stable again – although the exact relation was not quantified.[4]

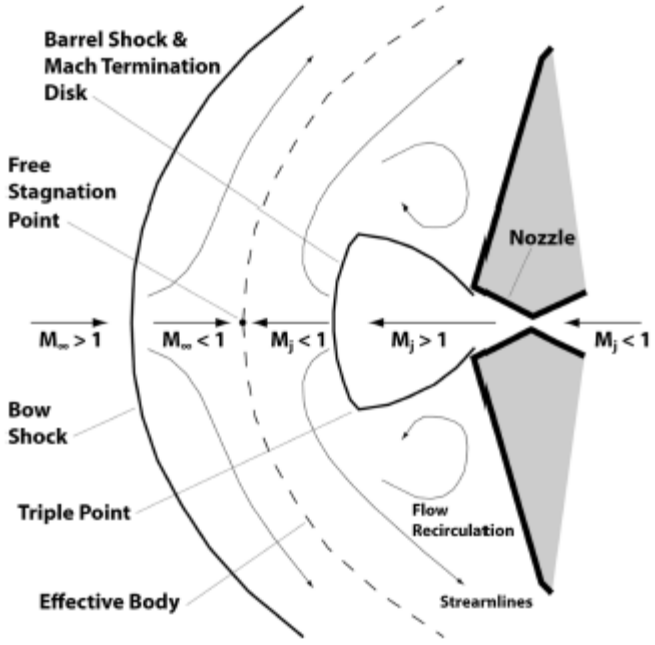

Figure 1.1: Conceptual sketch of SRP flow features[26]

In the late 1960s and early 1970s a limited number of experiments were conducted to study the effects of a tri-nozzle configuration, with the retrorockets placed near the periphery of the aeroshell forebody.[4,5,18] It was found that for a peripheral configuration, the bow shock between the retrorockets was detached from the forebody, maintaining a high pressure region on the model surface, and thus maintaining a large amount of aerodynamic drag. This is unlike a single-centrally located retrorocket, which shields the model surface from the flow behind the vehicle bow shock and reduces the aerodynamic drag. It is desirable to maintain as much aerodynamic drag as possible, on conjunction with reotro-thrust to decelerate a Mars lander; any loss of aerodynamic drag means a larger percent mass fraction of the payload would need to be dedicated to retrorocket fuel, or larger retrorockets would be needed to decelerate a lander. Differential throttling, using different thrust levels for individual retrorockets, was also investigated to produce pitching and yawing control moments.

Limiting factors, such as the inability to scale supersonic parachutes to adequate size, coupled with the desire to send manned missions to Mars (with landed masses estimated at 20-100 metric tons),[19-22] has prompted renewed interest in experimental and computational efforts to better understand the highly complex flow properties of SRP and HRP.[10,11,23-31] Experimental efforts by Palaszewski and Bencic have tested 3-inch models with a single retrorocket on the vehicle stagnation point using Schlieren, pressure and temperature sensitive paint, pressure taps, and thermocouples in the NASA Glenn 1'x1' Supersonic Wind Tunnel at Mach 3, as a baseline for further testing of a peripheral tri-nozzle configuration.[11] Due to the 3-inch model causing blockage in the tunnel, model size was reduced to 2.5 inches for subsequent testing of a tri-nozzle configuration at Mach = 2.5, 3.0, 3.5, 4.0 and 5.0.[23] A recent joint effort was designed by experimentalists in conjunction with computationalists to provide a comprehensive set of validation and verification quality data and study the unsteady effects of the flow which has been reported.[10] Testing was carried out at NASA Langley's Unitary Plan Wind Tunnel for a 5-inch model at Mach 2.4, 3.5, and 4.6 using pressure taps, several of which are capable of 40 kHz measurements, thermocouples, and high speed schlieren. The experimental model was interchangeable between a single-nozzle, peripheral tri-nozzle, or novel quad-nozzle configuration, which was a combination of the first two configurations (a single central nozzle and three peripheral nozzles).[24] Follow-up testing was also conducted at the NASA Ames 9'x7' Supersonic Wind Tunnel using the same model and the schlieren technique in Mach 1.8 and 2.4 flow.[25] These test results have been vital for validation efforts of three Navier-Stokes computational codes, DPLR, FUN3D, and OVERFLOW. [28-30]

1.2 Research Approach

The primary objective of this research is to utilize the extensively developed planar laser-induced iodine fluorescence method to provide a new, fundamental aerodynamic data set for single-nozzle and quad-nozzle retropropulsion configurations interacting with a hypersonic freestream flow. The high-resolution flowfield datasets are the first non-intrusive measurement results for an HRP flowfield, and are valuable for CFD code validation. The proposed research under this objective has been divided into two research areas: qualitative flow visualization and quantitative PD jet mole fraction and planar temperature and velocity measurements. These experimental results present the first spatially resolved, non-intrusive flowfield measurements for a HRP flow, and thus provide a unique dataset useful for computational fluid dynamic code validation. A secondary objective is to use the experimental results for verification and validation of computational fluid dynamics computations done at the University of Michigan.[31]

1.2.1 Research Area 1: Qualitative Flow Visualization

The goal of this research area is two-fold:

1) To understand shock-shock interactions between the retrorocket model and the wind tunnel (model blockage effects). This is necessary for experimental results to be useful for computational comparisons. Desirable conditions to minimize these interactions will be established in order to perform quantitative measurements.
2) To provide qualitative measurements guiding further quantitative measurements and for comparison with computational fluid dynamics.

Since testing blunt body models in the UVa hypersonic wind tunnel is a relatively new endeavor, and testing of retrorockets has never been conducted in this facility, it was unknown

whether the moderately small hypersonic flow facility would be too restrictive on model sizing. This needed to be determined. While both quantitative and qualitative measurements are possible with planar laser-induced iodine fluorescence, visualizations are less time-intensive (approximately three hours less for 6 test conditions, than a quantitative measurement for a single test condition). It is clear that visualizations at a range of PD jet thrust levels would be the most efficient way to quantify the sizing limits of the models in the hypersonic wind tunnel for retropropulsion experiments (the model flowfields are larger for larger PD jet thrust levels). The resulting model sizes and thrust levels then provides the most appropriate conditions for quantitative mole fraction, temperature, and velocity measurements. Visualizations also provide a useful identification of flowfield features, such as shock stand-off distances (due to the retrorocket pushing the bow shock upstream of the model).

1.2.2 Research Area 2: Quantitative Measurement

The goal of this research area is to provide quantitative planar data sets. These data sets consist of planar PD jet mole fraction distributions for a novel quad-nozzle configuration, and planar temperature and velocity for both a single- and quad-nozzle configurations which can be used to compare with computational results.

Chapter 2 describes the theory behind the methods used for planar mole fraction, temperature, and velocity measurements: mole fraction is measured with a ratio of two PLIIF images, temperature is measured using a spectroscopic model for the iodine fluorescence, and velocity is measured using a molecular Doppler velocity shift.

1.3 Dissertation Outline

Chapter two will outline a brief formulation for the theory behind planar laser-induced iodine fluorescence, beginning from a rate equation model. Since the PLIIF method has been extensively developed,[32-42] the focus of the chapter will be to explain application of the technique for qualitative visualizations, and quantitative planar mole fraction, velocity, and temperature measurements in the PD jet flowfields.

Chapter three describes the experimental apparatus – the low density hypersonic wind tunnel, laser, optics, CCD camera, model design, and model thrust characterization.

Chapter four presents and discusses experimental flow visualization results: single-nozzle sonic and supersonic PD jet models, and quad-nozzle sonic and supersonic PD jet models. Mole fraction results for the quad-nozzle configuration are also presented and discussed.

Chapter five focuses on quantitative temperature and velocity measurements for the single sonic PD jet model. The overall characteristics of the flowfield are shown, and the high resolution of the technique will be demonstrated. Experimentally measured planar velocity and temperature will be compared with CFD results.

Chapter six includes quantitative velocity measurements, and temperatures computed from the inviscid energy equation for the single-supersonic PD model. The experimental results will be compared with CFD results from the University of Michigan.

Chapter seven presents the quantitative velocity results, and temperature computed from the invscid energy equation. Experimental results are compared with CFD velocity and temperature results from the University of Michigan.

CHAPTER 2: LASER-INDUCED IODINE FLUORESCENCE THEORY

Planar laser-induced iodine fluorescence (PLIIF) is an optical, non-intrusive, time-averaged spatially-resolved measurement technique which has been extensively studied, improved upon, and used for qualitative flow visualizations and quantitative species concentration, density, pressure, temperature, and velocity measurements over the past thirty years.[32-42] It is advantageous over line of sight techniques, such as schlieren, which have a lack of spatial resolution since the signal is integrated over the beam path length; however, PLIIF can resolve spatially within a plane, which is only limited by the laser sheet thickness. Furthermore, schlieren cannot be used in mixed rarefied/continuum flows, due to the low flow density and thus small changes in the index of refraction. The electron beam fluorescence technique has been used in rarefied flows, but lacks the ability to produce quantitative thermodynamic property measurements and velocity flowfields in mixed rarefied/continuum flows.[43] Another benefit of PLIIF is the ability to produce accurate velocity measurements in rarefied flows, unlike other methods such as particle image velocimetry, which are limited by velocity slip in these flows. This chapter will summarize the basic aspects of the theory of planar laser-induced fluorescence, using molecular iodine as a seeding species, and focus on the application to visualization, mole fraction, velocity, and temperature measurements.

2.1 Rate Equation and Iodine Model

When laser radiation is incident on a molecule and is resonant with the energy separation between two energy levels of the molecule, the radiation is absorbed and the molecule will transition from a lower state energy level to an upper state energy level. From the upper excited state, the molecule can de-excite back to the ground state by emitting a photon, termed

fluorescence. Properties of the molecule ground state, such as velocity, can be accurately measured by monitoring the emitted fluorescence.

Iodine molecules in the electronic ground, X, state will absorb radiation at 514.5 nm from an argon-ion laser and be excited to the upper electronic, B, state. From the upper excited state the iodine molecule will decay through various means back to the electronic ground state. A representation of the absorption and decay processes is shown in Figure 2.1. The total ground electronic state population is represented by N_1 and the total population of the upper excited electronic level is given by N_2. f_1 and f_2 represent the fractions of the rotational/vibrational levels of the ground and upper excited states that are in resonance with the laser. The rate at which iodine molecules are excited to the upper energy state is given by the stimulated rate coefficient, b_{12}. When an iodine molecule is in the upper excited state it can redistribute to nearby rotational quantum levels through molecular collisions, or decay back to the ground state through various processes. The primary processes of interest for the current work are spontaneous emission, or fluorescence, given by A_{21}, and inelastic collisions with other molecules returning excited state iodine to the ground state, known as collisional quenching, Q_{21}. Other possible processes for an excited upper state molecule to return to the ground state include stimulated emission, b_{21}, in which the molecule is stimulated to the ground state by the laser radiation. Also, predissociation, Q_{23}, is a decay transfer mechanism in Figure 2.1, and occurs if a third dissociative energy state overlaps the B state. It is estimated that fewer than 1% of the iodine molecules transition to the N_3 state shown in Figure 2.1, so predissociation is also considered neglible.[32] Dissociation can occur if an energy source is energetic enough to separate the iodine molecule directly into atomic iodine. But, dissociation is not considered because the laser photon excitation energy (frequency) of the 514.5 nm line of the argon-ion laser is not sufficiently energetic; however, dissociation

would be a concern with laser photons in the argon-ion laser line at 488 nm. Significant stimulated emission requires a powerful laser source. Since the maximum laser power used in the current study is 1.5W and only a fraction of this power is available to an iodine molecule, stimulated emission is considered negligible.

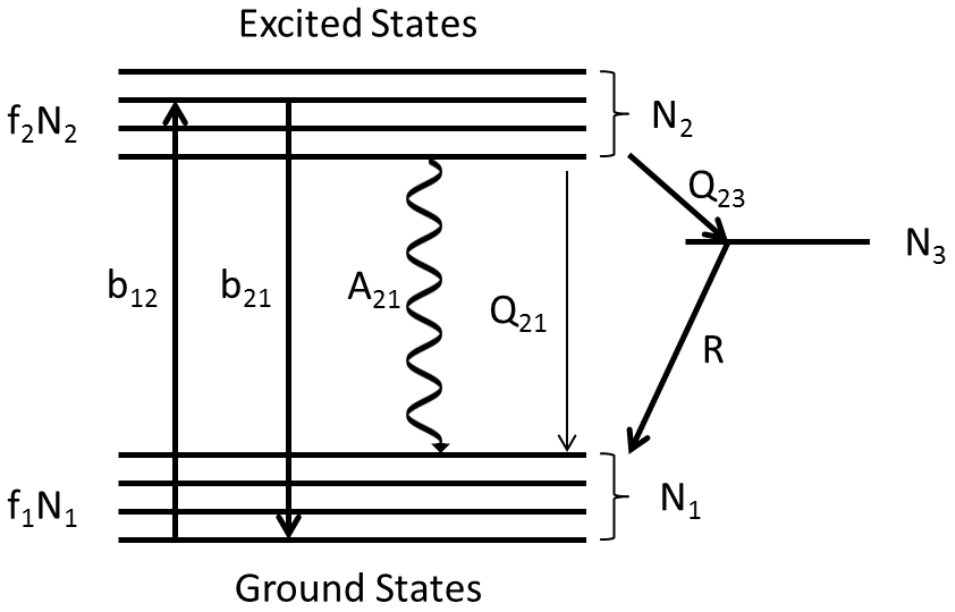

Figure 2.1: Energy transfer mechanisms between ground electronic X state and excited B state for iodine

Using the above energy level diagram and considering spontaneous emission and collisional quenching as the only possible decay mechanisms, it is possible to write a rate equation, given by equation 2.1, for the population decay from the upper excited energy level:[32]

$$\frac{dN_2}{dt} = b_{12} f_1 N_1 - (A_{21} + Q) N_2 \qquad (2.1)$$

The first term on the right hand side promotes the molecules to an excited vibrational/rotational level in the excited B state. The second term is the decay from that energy level to the X state

due to fluorescence and collisional quenching. (Note that, implicit in equation 2.1 is the assumption that the spontaneous emission coefficient is constant across all the energy levels populated in the upper excited state. This is valid because the fluorescence is collected from all upper states in this approach and the specifics of what vibrational/rotational levels are populated are not necessary.) A continuous wave (CW) laser is used for this study, therefore the time-dependent term on the left hand side of equation 2.1 is equal to 0. It can be shown that for a narrowband laser, where laser linewidth is less than the absorption linewidth of the iodine molecule, the solution of equation 2.1 can be written for the fluorescence signal resulting from excitation of a single ro-vibrational transition in the B-X state as:[32]

$$S_F = C f_{v''J''}(T) \left[\frac{A_{21}}{A_{21}+Q(p,T)}\right] \frac{V(p,T,u,v)}{\Delta\nu_D(T)} I f_s n \tag{2.2}$$

From equation 2.2, it is evident the fluorescence signal acquired, using a CCD camera in this work, is a function of flow temperature, pressure, velocity, and laser frequency. The fluorescence constant, C, is unique to each experimental set-up and is dependent on the camera and optical collection parameters. The spectroscopic parameters, i.e. Frank-Condon and Hönl-London factors, which are dependent on the absorption transitions, are also part of the constant C. The Boltzmann population fraction, $f_{v",J"}$ is a measure of the distribution of rotational/vibrational energy levels in the ground X state, and is dependent on flow temperature. The bracketed term is a measure of the fluorescence efficiency, the ratio of fluorescence to total decay processes, known as the Sterm-Volmer factor. Quenching, Q, is dependent on collision rate for each excited molecule, and is thus a function of pressure and temperature. The Voigt profile, V, is a convolution of Gaussian and Lorentzian broadening due to non-homogenous and homogenous processes, such as Doppler broadening (non-homogenous) and pressure broadening

(homogenous). The iodine seeding fraction, f_s, is constant for this work at approximately 1 part I_2 in 5,000 parts N_2, given by the vapor pressure of iodine at the conditions under which it is mixed with the N_2. The laser intensity is given by I, and the flowfield number density is given by n.

2.1.1 Iodine Transitions

One of the reasons why iodine is such an attractive molecule for PLIF studies is because it is a heavy diatomic with many absorption transitions available. The B-X transitions accessible under the argon-ion gain profile for the present work are shown in Figure 2.2. Note that the frequency scale is relative to the center of the argon-ion gain profile, so the P13/R15 transition is approximately +2 GHz off-center of the gain-profile. The vibrational quantum numbers are given by v, where double-prime refers to the ground state and single prime to the excited state. The rotational quantum number is designated by J. The rotational ground state quantum number, J", is given by the subsequent number, ie R13 refers to J" = 13. The P and R designations refer to transition from the ground rotational transition from J" to J' and is given as J" + 1 for R branch transitions and J" - 1 for the P branch. Therefore, for example, P13(v' = 43, v" = 0) refers to a transition from J" = 13 to J' = 12 and from v" = 0 to v' = 43. It is evident from Figure 2.2 that the transitions under the gain profile of the argon-ion laser are primarily in the v" = 0 ground vibrational state, with the exception of the hot band (v" = 1). Particularly of interest are the P48/P103 (J" = 48 and 103) and P13/R15 (J" = 13 and 15) transitions for velocity and temperature measurements, which will be discussed further in sections 4 and 5. As previously mentioned, Equation 2.2 is for a single ro-vibrational transition in the X electronic state. To resolve an absorption profile, as shown in Figure 2.2, it is necessary to scan the narrowband laser over the iodine transitions under the argon-ion laser gain profile.

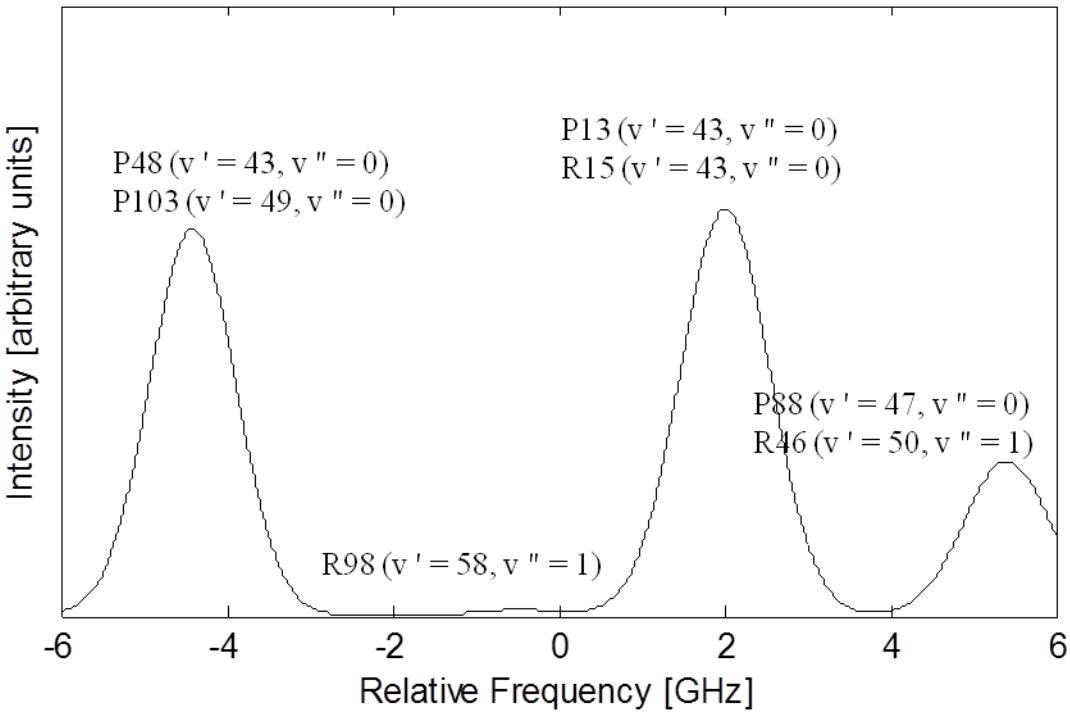

Figure 2.2: Calculated iodine absorption transitions available under argon-ion gain profile

2.1.2 Boltzmann Population Fraction

The Boltzmann population fraction is separated into the rotational and vibrational level contributions and given by the following set of equations:

$$f_{v",J"} = f_{v"} f_{J"} \tag{2.4}$$

$$f_{v"} = exp\left(-v" \frac{\theta_{vib}}{T}\right)\left[1 - exp\left(\frac{\theta_{vib}}{T}\right)\right] \tag{2.5}$$

$$f_{J"} = \frac{(2J"+1)\exp\left[-J"(J"+1)\frac{\theta_{rot}}{T}\right]}{\frac{1}{\sigma}\frac{T}{\theta_{rot}}} \tag{2.6}$$

where, for iodine, $$\theta_{vib} = 308.62\ K \tag{2.7}$$

$$\theta_{rot} = 0.0537\ K \tag{2.7}$$

In the equations, v" and J" correspond to the ground state vibrational and rotational quantum numbers. The characteristic vibrational and rotational temperatures are given by θ_{vib} and θ_{rot}, respectively, and σ is 2 for symmetric diatomic molecules. The distribution of the population for a range of vibrational and rotational quantum numbers at various temperatures is shown in Figures 2.3 and 2.4, respectively. As temperature increases, higher quantum number states begin to populate. In the temperature range for the following experiments, 10-300 K, the vibrational ground state, v" = 0, contains the majority of the population, as seen in Figure 2.3. As seen in Figure 2.4, at room temperature the maximum rotational population occurs at J" = 52; however, at the lower temperature ranges expected in this work, the maximum populated state occurs at lower rotational quantum numbers and J" = 9 becomes the most populated state at T = 10 K. The availability of low rotational quantum number transitions (i.e., J" = 13 ad 15) near the center of the argon-ion laser gain profile is what makes PLIIF such an attractive method for low temperature studies.

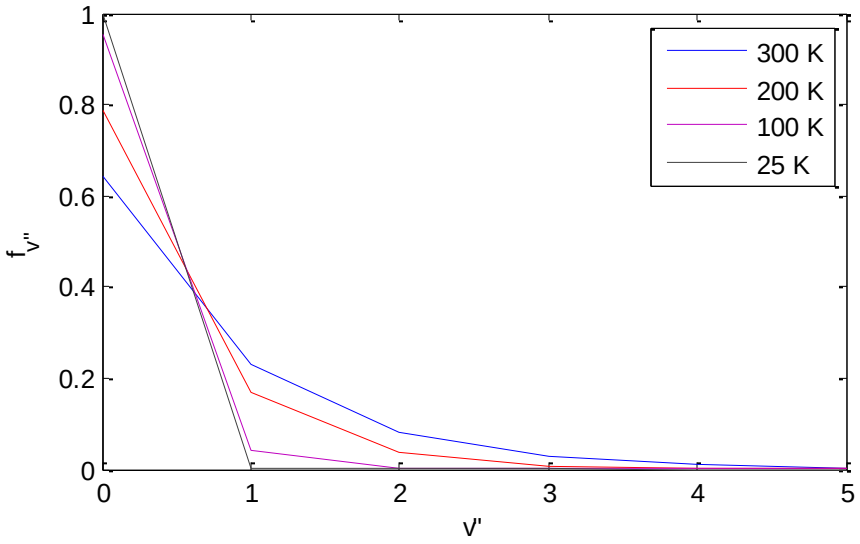

Figure 2.3: Vibrational Boltzmann populational fraction vs vibrational quantum number for several temperatures

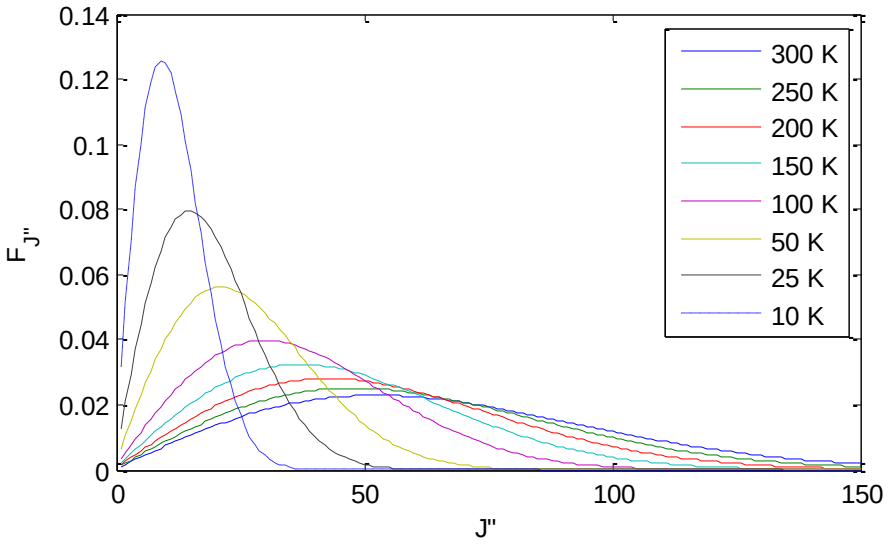

Figure 2.4: Rotational Boltzmann populational fraction vs rotational quantum number

2.1.3 Stern-Volmer Factor

As mentioned previously, the Stern-Volmer factor is a measure of the fluorescence efficiency, and depends only on the fluorescence decay rate and collisional quenching rate. Because the collisional quenching term depends on collisional frequency, and therefore on pressure and temperature, it is useful to re-write the Stern-Volmer factor in the following manner:

$$\frac{A_{21}}{A_{21}+Q} = \frac{1}{1+\frac{Q}{A_{21}}} \tag{2.9}$$

This relation gives the Stern-Volmer factor as the ratio of collisional quenching to fluorescence emission. Because the collisional quenching and emission coefficients are considered to be an average for all transitions considered, the following empirical relationship has been determined:[35]

$$\frac{Q}{A_{21}} = c_q \frac{p}{\sqrt{T}} \tag{2.10}$$

where the constant c_q was empirically determined by Hartfield to be equal to 2.1 $K^{0.5}$ / kPa.[35]

2.1.4 Voigt Lineshape Function

The Voigt lineshape function accounts for pressure and thermal broadening and is a convolution of the Lorentzian and Gaussian profiles. The Lorentzian profile accounts for homogenous, or pressure broadening, where the collisions in the flow perturb the absorption energies. Gaussian broadening is due to thermal, or Doppler, broadening and is in-homogenous. The random thermal motion of the molecules will cause individual molecules to absorb at slightly different wavelengths, and causes a frequency broadening effect of the profile. The Voigt function accounts for the convolution of both types of broadening, and is written as follows:

$$V(D,B) = \frac{B}{\pi}\int_{-\infty}^{\infty} \frac{e^{-y^2}}{B^2+(D-y)^2}\,dy \tag{2.11}$$

where D is the detuning parameter and B is the broadening parameter given by the following relations for the detuning and broadening parameters:

$$B = \sqrt{\ln(2)}\,\frac{\Delta\nu_c}{\Delta\nu_D} \tag{2.12}$$

$$D = 2\sqrt{\ln(2)}\,\frac{\Delta\nu}{\Delta\nu_c} \tag{2.13}$$

Detuning of the laser wavelength from the absorption linecenter is given by $\Delta\nu$. The collisional linewidth, $\Delta\nu_c$, was shown by Fletcher to be proportional to the pressure and inversely proportional to temperature to the 0.7 power, and is given in equation 2.14.[34]

$$\Delta\nu_c = C_b \frac{p}{T^{0.7}} \tag{2.14}$$

The constant C_b used for this work was measured by Donohue to be 4.1962 GHz $K^{0.7}$ / KPa.[36] The Doppler linewidth is only a function of temperature, and can be calculated from equation 2.15:

$$\Delta\nu_D = \sqrt{\frac{8\ln(2)kT}{mc^2}}\nu_0 \tag{2.15}$$

The mass of the molecule is given by m, c is the speed of light in vacuum, k is the Boltzmann constant, T the translational temperature, and ν_0 is the molecular center frequency. It is important to note that at high temperature and low pressure, Doppler broadening will dominate with a Gaussian lineshape. At high pressures collisional broadening will dominate and a Lorentzian profile results; however, fluid flows in this work typically occur between these two extremes, and thus the convolution is needed.

The Voigt lineshape function has been extensively calculated and various numerical methods are available for its evaluation. For the present work the method described in Ref. 44 has been converted from Fortran to Matlab and optimized for numerical efficiency. At very low pressure, the collisional broadening becomes negligible, and the hyperfine structure of the iodine absorption transitions become apparent, as shown in Figure 2.5 for the P13/R15 transition. Hyperfine components occur because of the interaction of the nuclear spin magnetic moment with the magnetic field from the electronic spin and orbital angular moment.[45] For odd rotational number there are 21 hyperfine components and 15 for even rotational quantum numbers. The 42 hyperfine components and relative line strengths due to the P13 and R15 transitions are shown in the hyperfine absorption spectrum in Figure 2.5. The frequency location and linestrength values

of each hyperfine component in the P13/R15 and P48/P103 are included in a model for the iodine absorption spectrum.[38] The spectral model of the iodine fluorescence developed in this section will be used to provide quantitative measurements in the flowfields of this work.

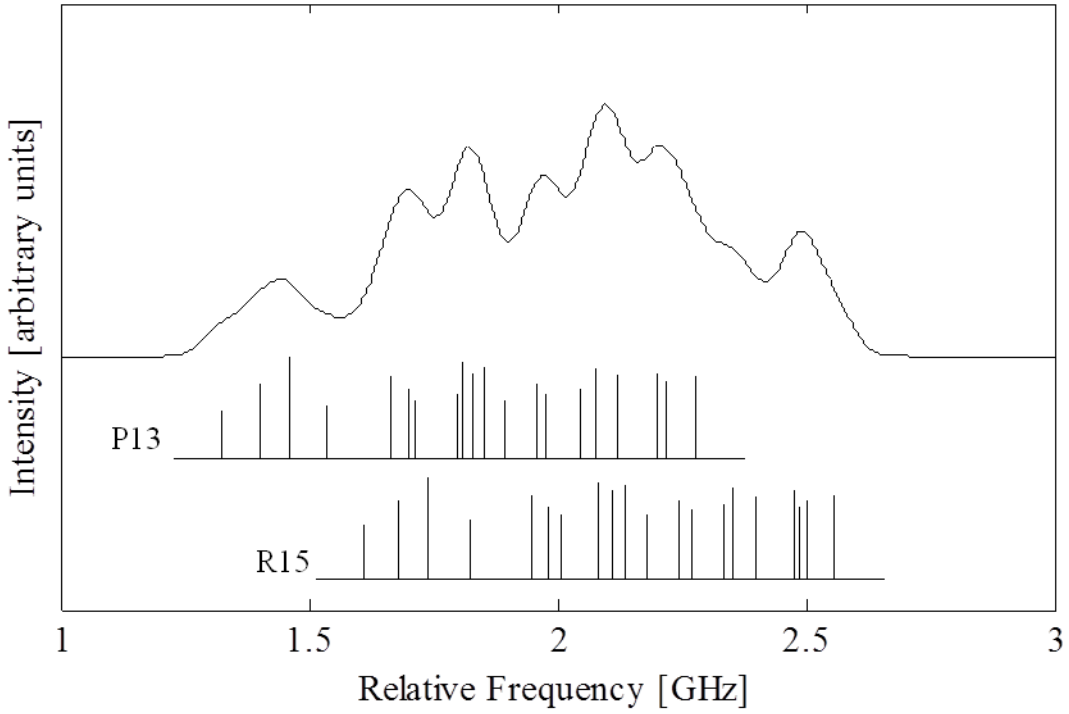

Figure 2.5: Hyperfine absorption spectra and relative hyperfine linestrengths and positions for the P13/R15 transition

2.2 Broadband Measurements

Broadband refers to the use of the argon-ion laser with an intracavity etalon (an etalon placed in the laser cavity beam path) removed. In this mode of operation all longitudinal modes under the 10 GHz laser gain profile are lasing at 514.5 nm. This results in the laser linewidth being much greater than the iodine absorption linewidth. Since, the Voigt lineshape function is normalized, it integrates across the gain profile to unity, and equation 2.2 simplifies to the following:

$$S_F = C f_{v''J''}(T) \left[\frac{A_{21}}{A_{21}+Q(p,T)}\right] I f_s n \tag{2.16}$$

Visualizations and mole fraction measurements rely on the broadband measurement technique, and will be discussed in the following two subsections.

2.2.1 Visualizations

Planar visualization measurements are useful for identifying key features in a flow, such as the location and interactions of shocks. In the present work, a hypersonic low density wind tunnel is used for the experimental work, discussed in Chapter 3. The wind tunnel provides an isentropic expansion from a sonic orifice, and testing is conducted in the isentropic core at Mach 12. Because the seeding fraction of iodine in the tunnel is so low, it is adequate to assume the test gas to be composed of nitrogen, and use a specific heat ratio of 1.4 and isentropic conditions to compute the pressure and temperature at various Mach numbers through the test section. The computed pressure and temperatures can be used to calculate the Stern-Volmer factor and Boltzmann population fractions to explain how the fluorescence signal in equation 2.16 varies with increasing Mach number. The computed Stern-Volmer factor and Boltzmann population fraction versus Mach number are shown in Figures 2.6 and 2.7 (assuming wind tunnel reservoir conditions of 300 K and 182 kPa). Note that as Mach number increases the temperature and pressure decrease, resulting in the collisional quenching term becoming negligible and the Stern-Volmer factor approaches unity by about Mach 8. Further, the Boltzmann population fraction is nearly constant in the Mach 8-14 range due to the decreasing flowfield temperature and rotational population shifting to lower rotational quantum states. Considering equation 2.16 with constant laser power, seeding fraction, Stern-Volmer approaching 1, and a relatively constant Boltzmann population fraction, it becomes apparent that in the Mach 8-14 range the fluorescence

signal will be directly proportional to the flowfield number density. Therefore, flowfield density can be accurately measured with planar broadband laser excitation. Results will be shown in Chapter 4.

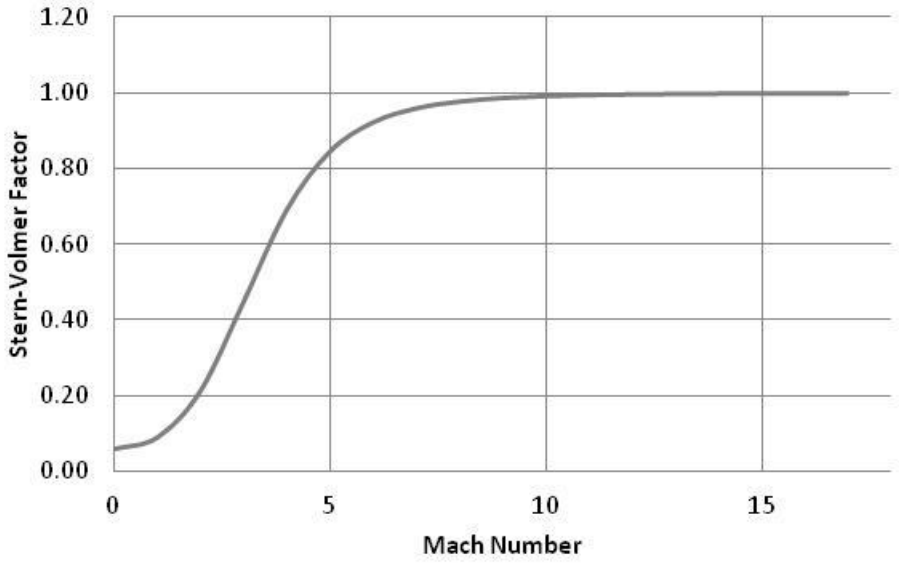

Figure 2.6: Stern-Volmer factor versus Mach number

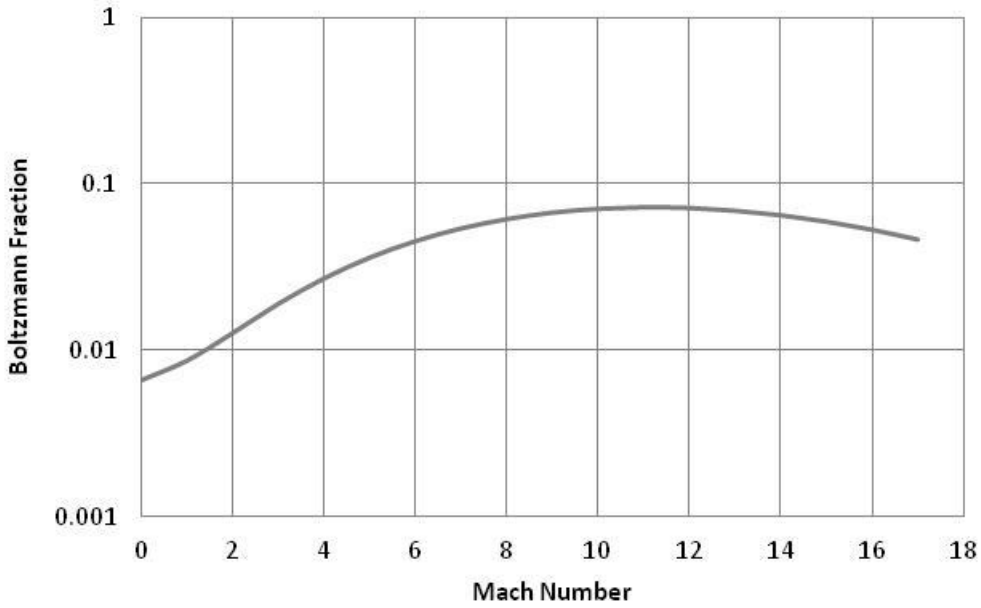

Figure 2.7: Boltzmann population fraction versus Mach number

2.2.2 Mole Fraction

In the present work PD jets thrust into a hypersonic Mach 12 flow. Either the PD jet, freestream, or both PD jet and freestream flow can be seeded with iodine. To analyze how the PD jet fluid mixes with the freestream, the PD jet mole fraction is calculated by taking the ratio of a PD jet-only seeded image, where no iodine molecules are present in the freestream flow, to a full-flow seeded image, with iodine present in both the PD jet and freestream flow. Since the thermodynamic dependencies are constant at a given pixel location within the flowfield for both images (only the seeding method will be different), the parameters, such as Stern-Volmer factor, Boltzmann population fraction, and signal constant, cancel in the ratio, as seen in equations 2.17-2.20.

$$S_{F_{Ratio}} = \frac{S_{F_{Jet}}}{S_{F_{Total}}} \tag{2.17}$$

$$S_{F_{Ratio}} = \frac{\cancel{C f_{v'',j''}(T) \frac{A_{21}}{A_{21}+Q(p,T)} I} \frac{f_{S_{Jet}}}{f_{S_{Total}}} \frac{n_{Jet}}{n_{Total}}}{\cancel{C f_{v'',j''}(T) \frac{A_{21}}{A_{21}+Q(p,T)} I}} \tag{2.18}$$

$$S_{F_{Ratio}} = \beta \frac{n_{Jet}}{n_{Total}} = \beta \chi_{Jet} \tag{2.19}$$

$$\beta = \frac{S_{F_{Ratio}}}{\chi_{Jet}|_1} = S_{F_{Ratio}} \tag{2.20}$$

where the subsequent "jet" refers to the jet values and "total" refers to the total flowfield values. The resulting fluorescence signal is now directly proportional to the PD jet number density normalized by the total number density, which is the PD jet mole fraction, X. The constant of proportionality is solved for by evaluating the equation where the PD jet mole fraction is unity, in this case, at the PD jet exit. Examples will be shown in Chapter 4.

2.3 Narrowband Measurements

A narrowband laser, with laser linewidth less than absorption linewidth, can be scanned over an absorption transition in discrete frequency step sizes. The resulting fluorescence emission intensity, as well as laser frequency, are known at each discrete step, so fluorescence emission intensity at each discrete frequency can be used to construct the absorption spectrum, shown in Figure 2.2 and 2.5. It is important to note here that the fluorescence intensity is used as a monitor of the absorption spectrum at each discrete pixel on the CCD chip. An intercavity etalon is installed in the laser to isolate single longitudinal modes under the laser gain profile, and a piezoelectric transducer is controlled to slightly vary the cavity length, resulting in the capability of 20 MHz frequency step sizes. This approach is illustrated in Figure 2.8. In the series of images the laser is scanned in frequency through the gain profile and an image is taken of the flowfield at each frequency. The intensity at a single pixel in the image, marked by a green circle with an X, is monitored through the series of images and plotted versus the relative frequency of the laser. In this way the absorption spectrum can be generated at each point in the flowfield. The location in the spectra corresponding to each image is labeled (a) through (f). The intensity variation in the images as the laser frequency is varied is due to the Doppler effect and will be discussed in the next section. Equation 2.2 can then be used to perform a non-linear least squares fit to the constructed absorption spectra, and relate the thermodynamic ground state properties, as well as molecular velocity, to the collected spectra. Since a single pixel in the CCD camera is being probed to create an absorption spectrum, the spatial laser intensity variation across the laser sheet does not need to be accounted for. In the subsequent sections, the Doppler shift seen

in Figure 2.8 will be discussed, as well as velocity and temperature measurements requiring operation of the laser in narrowband mode.

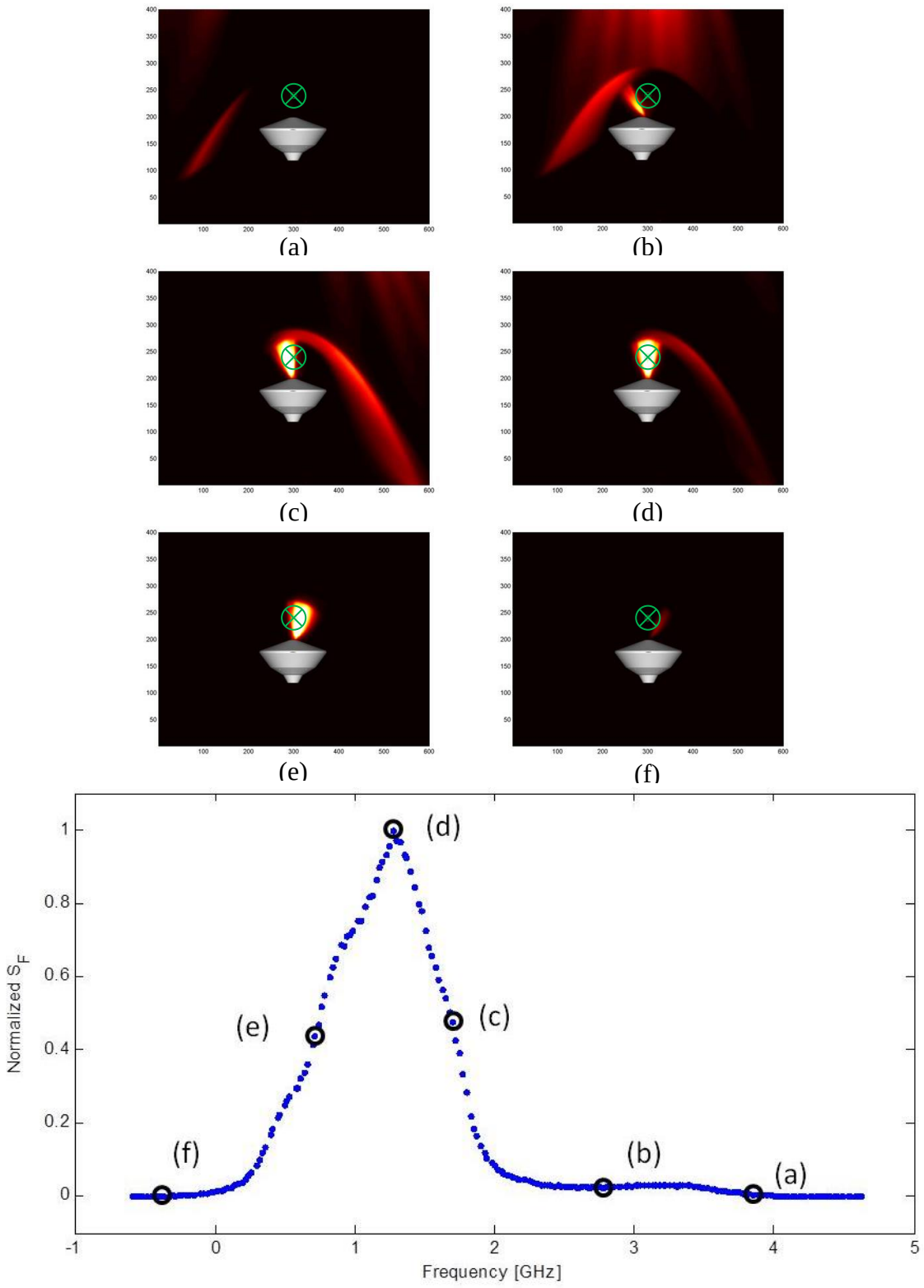

Figure 2.8: Compiling an absorption spectrum from image intensities at various laser frequencies, (a) – (f)

2.3.1 Velocity Measurements

This section will discuss how velocity can be measured with narrowband excitation using the Doppler effect. A complication arising from collisional impact will be discussed and ways to minimize this will be presented.

The velocity dependence of the PLIIF signal is caused by the molecular Doppler shift, where the absorbing iodine molecule interacts with the incident laser radiation at a shifted frequency from the molecular center frequency due to its motion relative to the laser sheet. Molecules moving toward the laser sheet will observe the laser radiation at a higher frequency, while molecules moving away from the laser sheet will observe the radiation at a lower frequency (molecules moving perpendicular to the laser sheet will not observe a shifted spectra). The Doppler shift for velocity in the direction of the laser sheet is given by equation 2.21:

$$\Delta\nu_{Dop} = -\frac{u}{\lambda} \tag{2.21}$$

where u is the velocity component in the direction of the laser, and λ is the wavelength of the laser. In order to obtain an absolute velocity for each point (pixel on the CCD camera), it is necessary that the Doppler shifted spectra be compared to a reference frequency. The reference frequency for this work is obtained by splitting a portion of the laser beam to a static cell filled with molecular iodine at zero velocity, and recording the resulting spectra with a photodiode. This process of comparing a static cell absorption spectrum to a flowfield spectrum is demonstrated in Figure 2.9, where the total measured frequency shift is given by $\Delta\nu_T$. The velocity calculated by equation 2.21 is only for motion in the direction of the laser sheet; therefore, it is necessary to use a second laser sheet to resolve a second velocity component, and thus measure the total planar velocity vector.

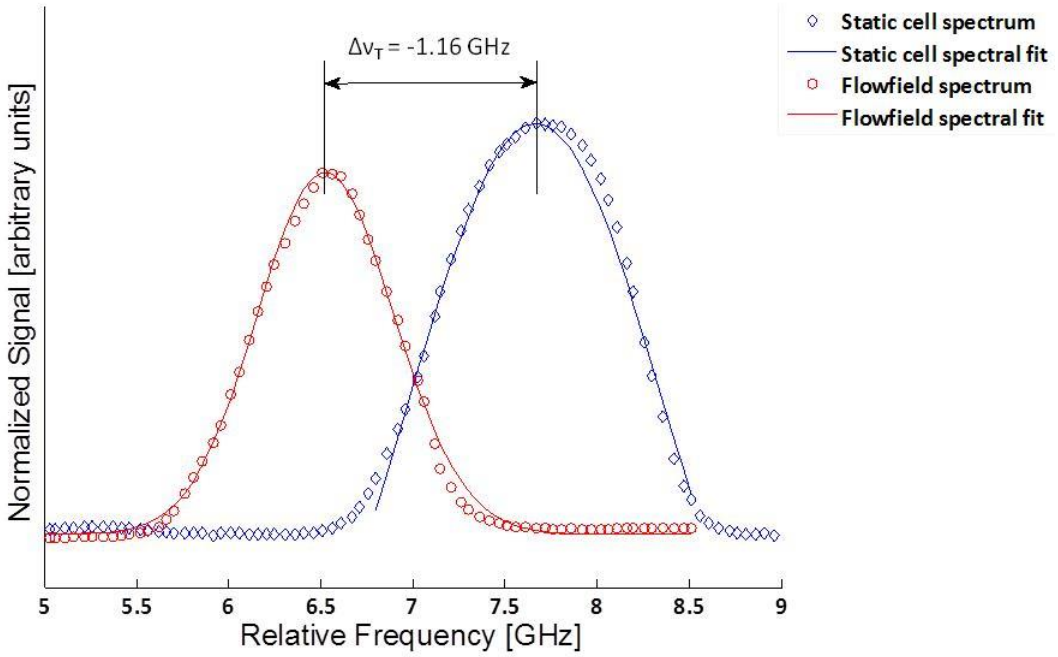

Figure 2.9: Total frequency shift observed from flowfield data point compared with un-shifted static cell spectrum (P13/R15 excitation)

The Doppler shift is only part of the total observed shift from the molecular center frequency. The overall frequency shift is due to the Doppler shift, and the impact shift, as shown in Equation 2.22.

$$\Delta\nu_T = \Delta\nu_{Dop} + \Delta\nu_I \tag{2.22}$$

While the Doppler shift is not a function of thermodynamic parameters and only the detuning parameter, $\Delta\nu$, the impact shift is a function of flowfield pressure and temperature. Since the impact shift is only a function of pressure and temperature, it is not laser sheet direction-dependent. The impact shift is always in the same direction. As flows become more rarefied, the impact shift will go to zero due to fewer molecular collisions; however, in higher temperature and pressure regions, the impact shift is non-negligible. Therefore to resolve the Doppler shift,

and thus the velocity vector from shifted spectra, it is necessary to either calculate the impact shift with a known pressure and temperature[34] or use some other method to eliminate the term.

Because the impact shift is not direction-dependent, it can be easily cancelled by using a counter-propagating beam approach. In this approach two laser sheets are used counter-propagating at exactly 180-deg. At each discrete point in the flowfield the impact shift is exactly equal from each laser sheet direction, but the Doppler shift is equal and opposite. Taking the difference of the absorption spectra from the two counter-propagating directions equations 2.21 and 2.22 can be used to resolve the Doppler shift in the one direction. To resolve a planar, two component, velocity field, 4 laser sheet angles are necessary. If the flowfield is symmetric, then a simulated counter-propagating beam approach can be used with two laser sheet directions.[46] It is assumed the thermodynamic properties at symmetry points (equidistant points from the line of symmetry) are the same, thus the impact shift will be the same, and can be cancelled. A counter-propagating beam approach is generally more desirable since the impact shift will directly cancel and it is unnecessary to make any assumptions about a plane of symmetry. However, in the present work a counter-propagating beam approach is not possible due to optical access to the test facility, so symmetry of the flowfield will be used (the flow will be shown to be symmetric in Chapters 5, 6, and 7).

A general diagram of the velocity vectors from two laser sheets i and j at symmetric points 1 and 2 in a flowfield is shown in Figure 2.10. By using the symmetry of the flow (about its centerline) two independent laser sheet angles, i and j, produce four velocity vector components at points 1 and 2. In the coordinate system of the lab (x-y coordinate system) it is evident the velocity component in the y-direction will be equal and the velocity component in the x-direction will be equal and opposite at points 1 and 2. Assuming the thermodynamic properties are the

same at points 1 and 2 due to the flow symmetry, and using the relationships for velocity components in the lab frame, the following equations can be written:

$$V_{1x} = -V_{2x} \tag{2.23}$$

$$V_{1y} = V_{2y} \tag{2.24}$$

$$\Delta\nu_{I_1} = \Delta\nu_{I_2} \tag{2.25}$$

Equations 2.22-2.25 can be used to write a general relationship of the Doppler components to the total measured frequency shift for the two laser sheet angles, thus negating the need for calculating impact shift. The relationship in a general form is given in equations 2.26 and 2.27 for the Doppler shifted velocity components at point 1 and 2 in the i and j laser sheet direction:[47]

$$\Delta\nu_{Dop_{1i}} = \frac{\frac{sin\theta_j}{sin\theta_i}\Delta\nu_{T_{1i}} + \frac{1}{2}\frac{cos\theta_j}{cos\theta_i}\left(\Delta\nu_{T_{1j}} - \Delta\nu_{T_{2j}}\right) - \frac{1}{2}\frac{sin\theta_j}{sin\theta_i}\left(\Delta\nu_{T_{1j}} + \Delta\nu_{T_{2j}}\right)}{\frac{sin\theta_j}{sin\theta_i} + 1} \tag{2.26}$$

$$\Delta\nu_{Dop_{1j}} = \frac{\frac{sin\theta_i}{sin\theta_j}\Delta\nu_{T_{1j}} + \frac{1}{2}\frac{cos\theta_i}{cos\theta_j}\left(\Delta\nu_{T_{1i}} - \Delta\nu_{T_{2i}}\right) - \frac{1}{2}\frac{sin\theta_i}{sin\theta_j}\left(\Delta\nu_{T_{1i}} + \Delta\nu_{T_{2i}}\right)}{\frac{sin\theta_i}{sin\theta_j} + 1} \tag{2.27}$$

where θ_i and θ_j are the laser sheet angles in the I and j directions, respectively, relative to the line of symmetry Once the Doppler shifts in the i and j directions have been calculated, equation 2.21 can be used to solve for velocity at point 1 in the laser sheet directions. Finally, it is necessary to convert the velocity in the direction of the laser sheet to the natural x-y coordinate system shown in Figure 2.10. A simple coordinate transform is used to convert the general i-j velocity components to an x-y coordinate system and results in equations 2.28 and 2.29.[48]

$$V_{1x} = \frac{-V_{1i}\cos\theta_j + V_{1j}cos\theta_i}{sin(\theta_i - \theta_j)} \tag{2.28}$$

$$V_{1y} = \frac{V_{1i}\sin\theta_j - V_{1j}sin\theta_i}{sin(\theta_i - \theta_j)} \tag{2.29}$$

The velocity vector components at points 2 are calculated using equations 2.28 and 2.29 with the relationships given in 2.23 and 2.24.

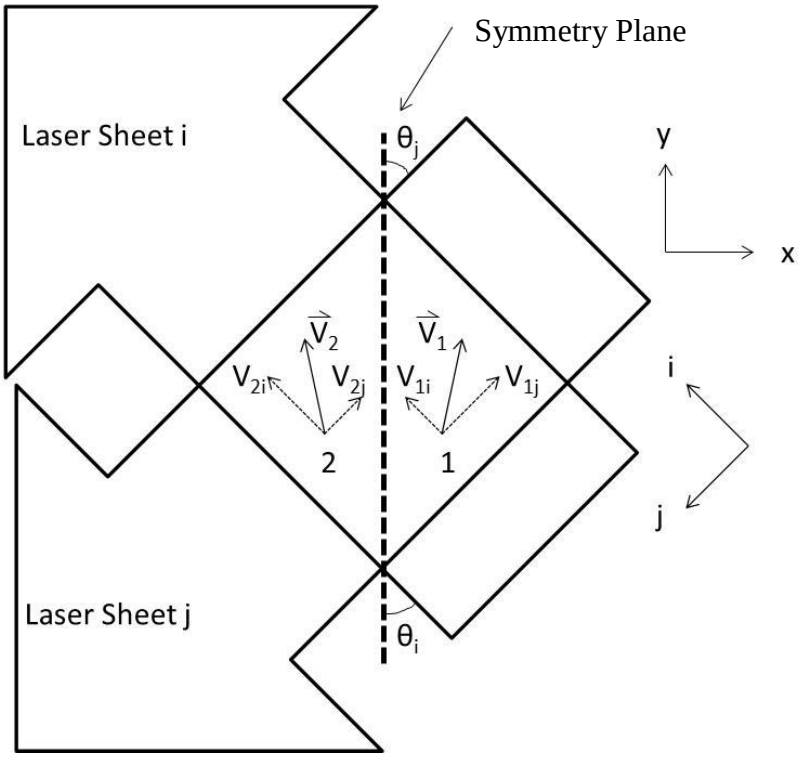

Figure 2.10: Velocity measurement diagram for symmetric flowfield, with points 1 and 2 chosen symmetrically about the symmetry line

2.3.2 Temperature Measurement

Two approaches to temperature measurement are needed, one in the region of the flow above about 50K and the other in the region where the flow temperature is less than 75K (between 50K and 75K both methods can be applied). These two approaches are discussed in this section.

The thermodynamic dependence of the absorption spectra is illustrated in Figure 2.11 for flowfield conditions expected in this work. Over the range of Mach numbers shown (the Mach number is variation is calculated for isentropic flow from reservoir conditions of 300K and 38 kPa) the spectrum changes dramatically, from collisionally and thermally broadened P13/R15 and P48/P103 peaks at Mach 1 conditions, to rarefied Mach 12 flow where the only thermal broadening remains and the hyperfine structure of the P13/R15 peak is resolved. Note the change in frequency scale in (c) and (d) relative to (a) and (b). The reason is that the P48/P103 transition on the left in (a) and (b) depopulates due to higher J" in low temperature regions. The frequency range is then over the P13/R15 transition only. In these vastly different flowfield conditions it is necessary to use two different methods to solve for temperature. At the higher temperatures where both P13/R15 and P48/P103 absorption transitions are highly populated it is possible to use a ratio of the relative peak heights. This ratio is temperature sensitive due to the vastly different rotational quantum numbers, discussed previously in section 2.1.2. However, as the flow becomes rarefied, and thus the ground state energy level distribution shifts to the lower rotational quantum level states, the two-peak method becomes impossible due to P48/P103 depopulation and a spectral fit to the hyperfine absorption spectrum using, equation 2.2 with the hyperfine line strengths, seen in Figure 2.5, is used to resolve the temperature.

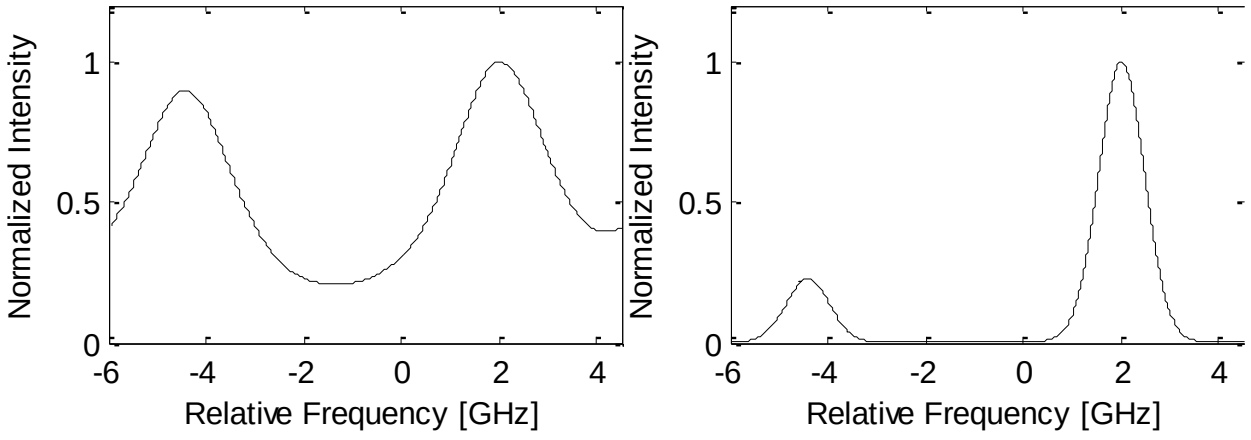

(a) Mach 1 conditions, T = 250 K, p = 20 kPa

(b) Mach 4 conditions, T = 71 K, p = 0.2 kPa

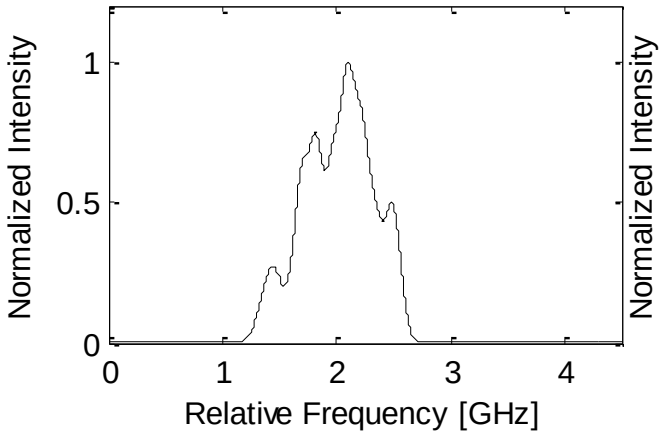

(c) Mach 8 conditions, T = 22 K, p = 0.003 kPa

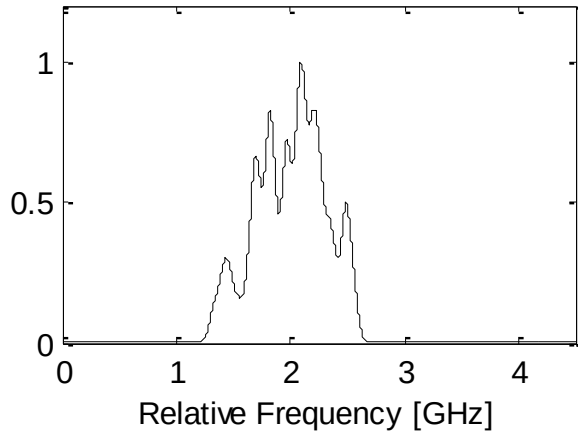

(d) Mach 12 conditions, T = 10 K, p = 0.0002 kPa

Figure 2.11: Thermodynamic dependence on absorption spectra

The two-peak ratio (T-ratio) method to solve for temperature works well in the range of about 50-300K, but at lower temperatures the P48/P103 rotational energy levels are largely depopulated and a ratio cannot be used. Figure 2.12(a) shows how the T-ratio is measured. In Figure 2.12(b) the fluorescence model (Eqn. 2.2) is used to compute the theoretical T-ratio versus temperature in the range of 50-300K, corresponding to the temperatures expected in the experimental flowfield. It was found by Donohue that an empirically-determined correction

factor is necessary to account for transition-dependent redistribution in the electronic B-state.[36] A simple correction factor can be calculated to account for the variations in the T-ratio due to the transition-dependent redistribution process if temperatures at discrete points in the static cell and flowfield can be reliably calculated.[36] In the current work, the temperature of the static cell is known, as well as multiple points along the centerline of an underexpanded jet, and a linear fit is performed to relate the measured T-ratio to known conditions at various points in the flowfield, and in the static cell; therefore, this correction factor is empirically determined from known T conditions and can be applied to the T-ratio in the high T regions of the flow (where above 50K).[49]

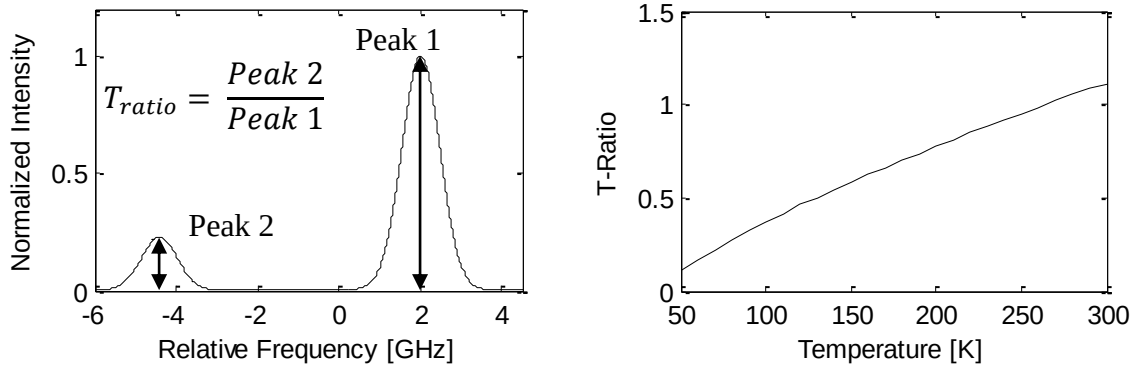

(a) Demonstration T-ratio

(b) Computed T-ratio from Eqn 2.2

Figure 2.12: T-ratio method used for computing temperature in the 50-300 K range.

For temperatures below approximately 75K, where the hyperfine structure is resolved, a non-linear, least squares fit of equation 2.2 to measured spectra is used. At these lower temperatures, the pressure is typically very low, and the broadening mechanism can be assumed to be completely due to thermal broadening.[37] In the overlapping range of 50-75 K both methods can be applied and compared.

CHAPTER 3: EXPERIMENTAL DESIGN AND PROCEDURES

In this chapter the experimental apparatus as well as experimental procedure, data acquisition format, and data analysis procedure will be discussed. The experimental apparatus can roughly be broken into three categories: the hypersonic wind tunnel, PD jet model, and optical components for PLIIF. The data acquisition has been thoroughly discussed in Ref. 52, so a brief overview of the necessary steps to take prior to an experiment will be discussed, as well as the data output format. Further, the data analysis method and program written for this work, as well as the work in Ref. 52, will be described. Finally, the start-up and shut-down procedures used to run the experiments will be described.

3.1 Hypersonic Wind Tunnel

The Aerospace Research Lab (ARL) hypersonic wind tunnel is a continuous-flow wind tunnel facility that provides a test section which is an underexpanded jet.[50] As shown in Figure 3.1, the underexpanded jet produces mixed continuum/rarefied flows with Knudsen numbers (ratio of molecular mean free path to jet orifice diameter) approaching 1 and Mach numbers from 1 to 16, before terminating in a Mach disk.[51] Nitrogen gas, seeded with approximately 200 ppm I_2, isentropically expands through a thin plate orifice of 2 mm diameter into a continuously-evacuated vacuum chamber. The underexpanded jet test section size is a function of mass flow rate and vacuum system pump efficiency, and can be determined based on the stagnation pressure, orifice size, and back pressure achieved (which are 1.8 atm, 2 mm, and approximately 280 mTorr, respectively). This results in an underexpanded jet test section length of approximately 8 cm.[49] Because this underexpanded flow is well modeled, testing at desired conditions can be achieved by placing the test model on the jet centerline a known distance from

the exit orifice. The distance necessary for a desired Mach number is calculated via the Ashkenas & Sherman relationship in equation 3.1:[49]

$$M = A\left(\frac{x-x_0}{D}\right)^{\gamma-1} - \frac{1}{2}\left(\frac{\gamma+1}{\gamma-1}\right)\left[A\left(\frac{x-x_0}{D}\right)^{\gamma-1}\right]^{-1} \quad (3.1)$$

where x_0 and A are constants (0.4 and 1.61, respectively) empirically determined by Ashkenas and Sherman for the specific heat ratio corresponding to N_2, the test section gas. For current work the model is placed at x/D of 21.0, corresponding to Mach 12.

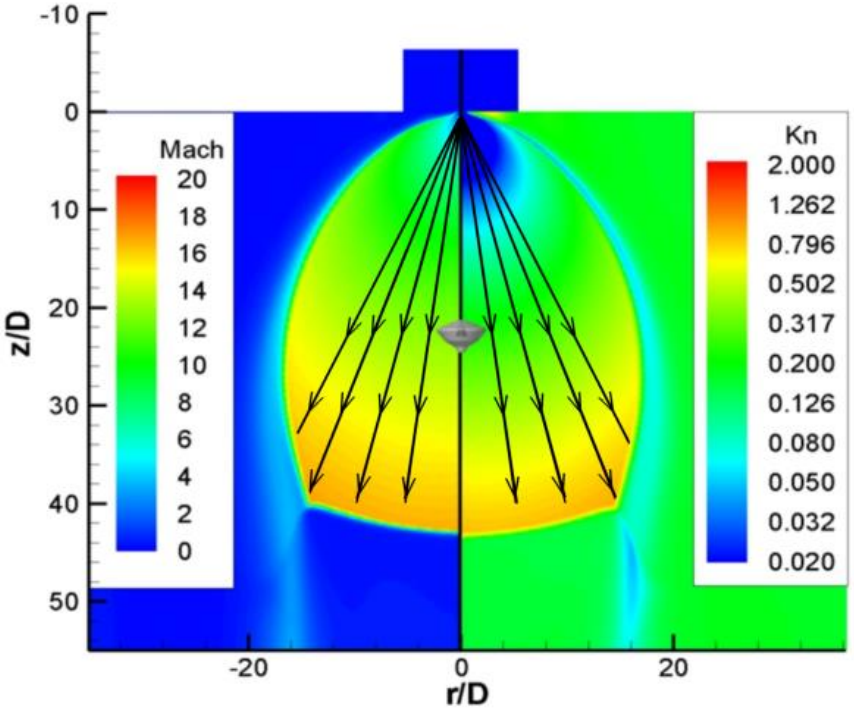

Figure 3.1: Calculation of Mach and Knudsen numbers in hypersonic test section.[51] Model position shown

The wind tunnel is continuously evacuated via three large vacuum pumps. The vacuum chamber allows optical access for the camera and various laser sheet angles via rows of 3 vertical

portholes spaced equidistant (90-deg offsets) around the cylindrical chamber (a diagram including the model mounting system and vacuum chamber will be shown in the next section). Flow to the facility comes from a bank of 18 nitrogen cylinders located outside the lab, and allows for experimental run times upwards of 30 hours. From the bank of cylinders the nitrogen gas can either enter into the iodine mixing vessel, or completely bypass the mixing vessel if iodine is not desired for a portion of the flow field (both the model and freestream are independently plumbed and can be run with or without iodine at any given time). Nitrogen gas entering the iodine mixing vessel pressurizes the vessel, typically to about 40 psia, and solid iodine beads sublimate to mix iodine gas with the nitrogen gas. The total pressure of the mixing vessel remains constant during experiments. Iodine seeding fraction is determined by the partial pressure of iodine at room temperature, and the total pressure of the iodine mixing vessel. Plenum pressure for the model and freestream are regulated via needle valves. Plenum pressure and temperature are monitored through two pressure transducers (an OmegaDyne Model PX409 0-15 psia range transducer for the model pressure, and OmegaDyne Model PX409 0-50 psia range transducer for freestream pressure), and type K thermocouples, respectively.

3.2 Model Design

Four models are used in the following work, as shown in Figures 3.2 and 3.3: a sonic and supersonic single-nozzle configuration with the PD jet located at the model stagnation point, as well as sonic and supersonic quad-nozzle configurations with the PD jets on the forebody midway between the stagnation point and model forebody shoulder. The models are 1 cm in diameter, which is 0.22% scale of the Mars Science Laboratory (MSL) frontal aeroshell. For initial visualization work models with a 2 cm diameter were used; however, these models were found to be too large for the wind tunnel test section. The jets for the sonic and supersonic

models are oriented parallel to the direction of freestream flow, which causes the jet exit orifice to be slightly elliptical for the quad-nozzle configurations. The sonic jet models have an equivalent jet exit diameter of 0.5 mm. The supersonic jet models have an equivalent jet exit diameter of 0.9 mm, with a throat diameter of 0.5 mm, corresponding to a jet exit Mach number of 2.66. The models are constructed of aircraft aluminum and painted matte black to minimize scattered light reflections from inside the chamber, as well as the model surface. Nitrogen seeded with iodine is supplied to the PD jets via a sting mounted to the aft body of the model. Different sting geometries were necessary due to machining constraints for the single-supersonic and quad-nozzle models.

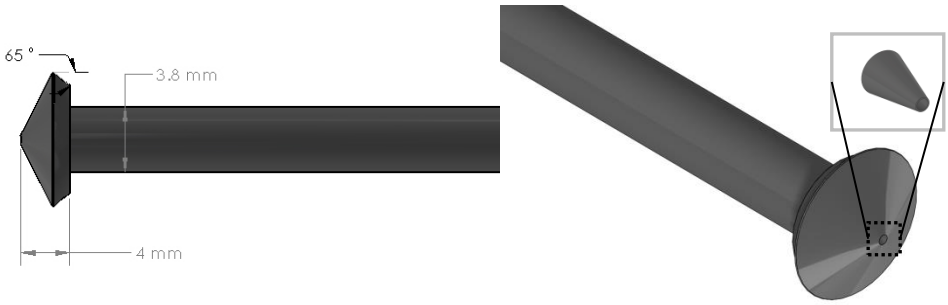

(a) Sonic Model Geometry (b) 3D View

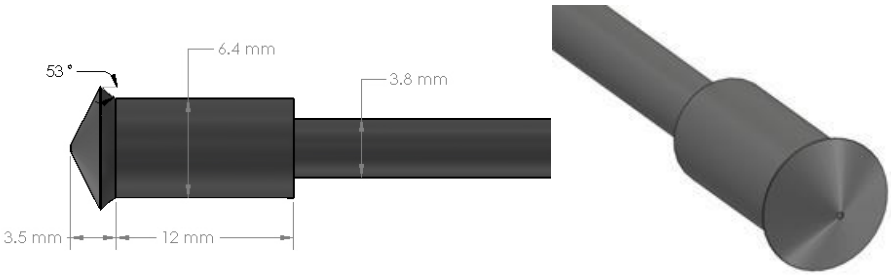

(c) Supersonic Model Geometry (d) 3D View

Figure 3.2: Single-nozzle model design geometry for the sonic nozzle model, (a) and (b), and supersonic nozzle model, (c) and (d). The 3-D view shows the PD jet centerline

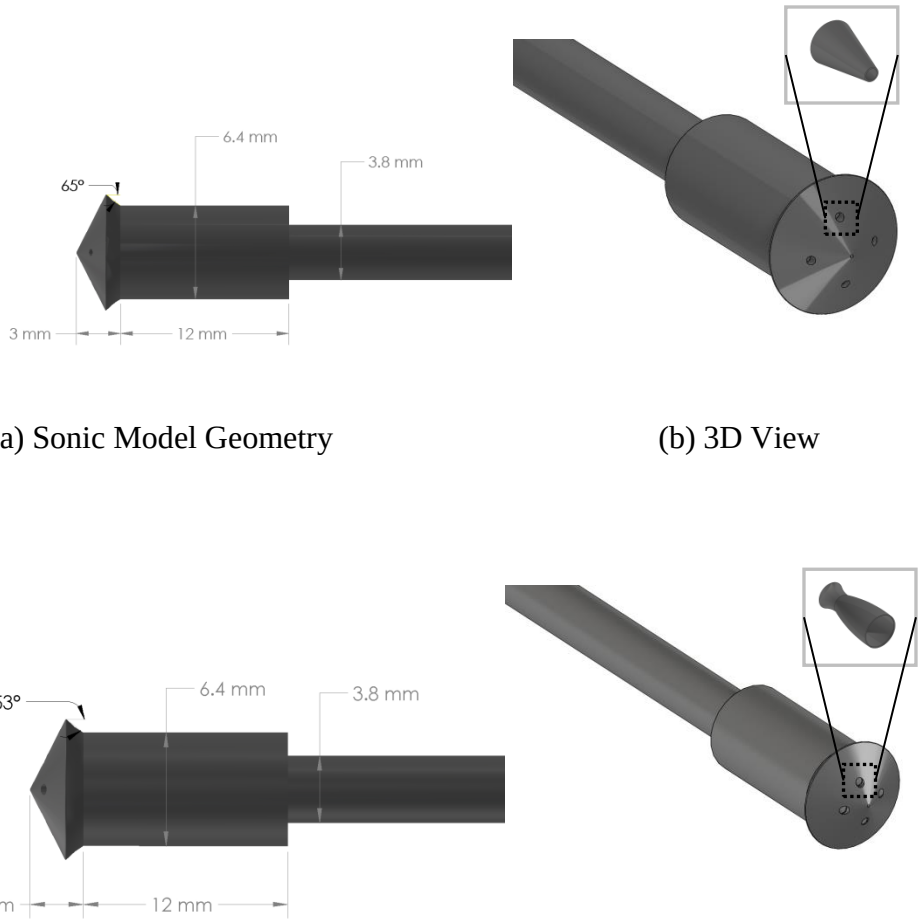

(a) Sonic Model Geometry (b) 3D View

(c) Supersonic Model Geometry (d) 3D View

Figure 3.3: Quad-nozzle model model design geometry for the sonic nozzle model, (a) and (b), and supersonic nozzle model, (c) and (d). The 3-D view shows the PD jet centerline

3.2.1 Model Mounting System

A model mounting system was designed and installed, as shown in Figure 3.4. The mounting system is directly connected to the inlet tube for the freestream flow, so when the vacuum pumps start and the chamber slightly compresses, the freestream exit orifice and model move together. The figure shows the vacuum chamber housing and model mounting system, as well as the

location of the camera viewing window and laser sheet access windows. To align the model for experiments it is essential to center the model under the freestream exit orifice. To confirm this alignment, 4 fields of view are possible: 1 from the tunnel door (left side of image), another from a camera image, a third by a telescope in the direction of the laser sheet, and a fourth, very limited view, from a bottom porthole window, not pictured in Figure 3.4 due to the cut away plane. With the mounting system the model can be centered under the freestream exit orifice, then the vertical z-direction adjustment can be largely made by determining how much of the model sting to feed through the mount. With the current model mounting system it is possible to consistently align the model to within ± 5 pixels (approximately 0.32 mm) in the frame of the camera.

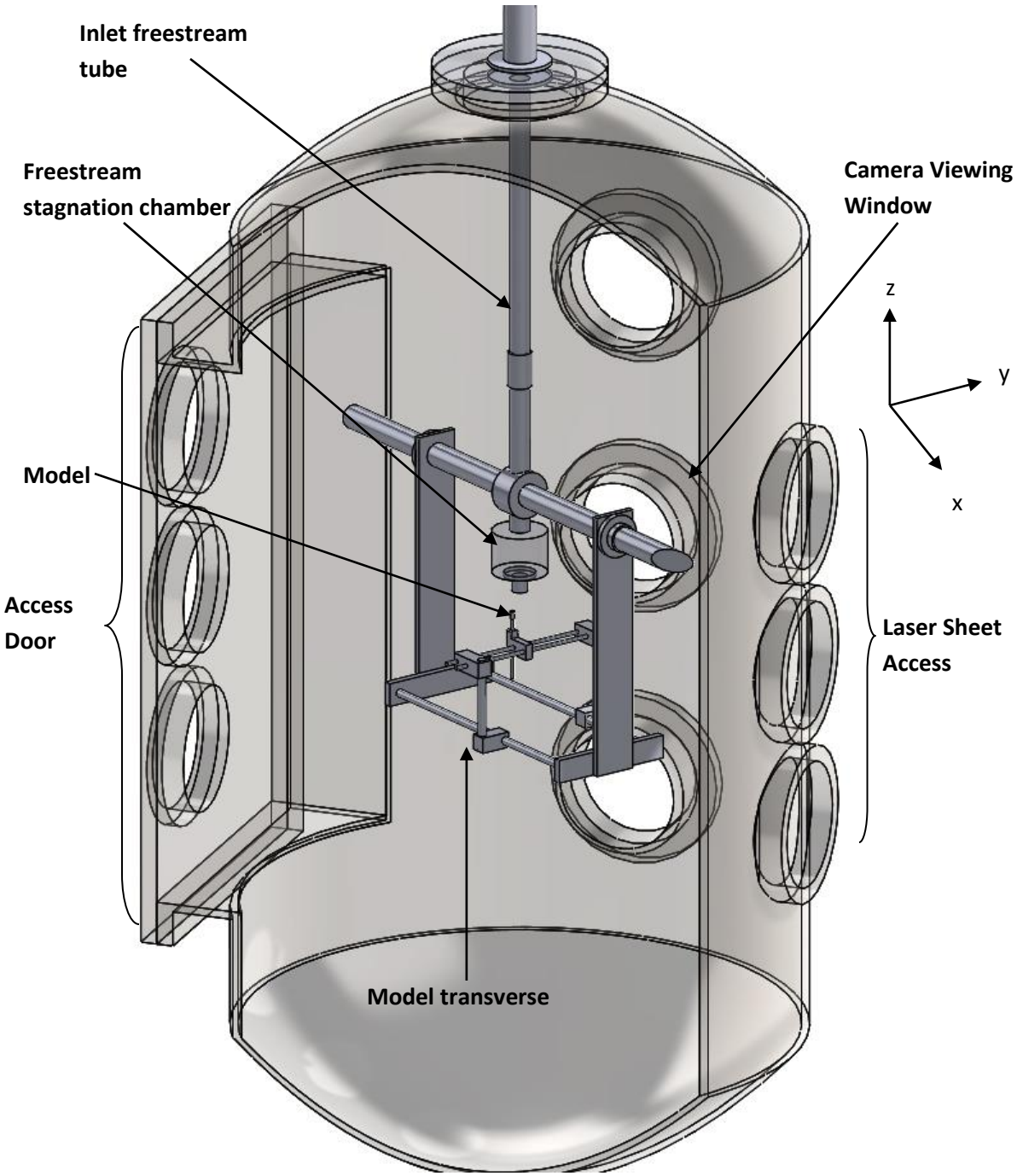

Figure 3.4: Cut-away view of vacuum chamber and model mounting system

3.2.2 Coefficient of Thrust

In order to compare experimental data from other facilities and CFD results, a non-dimensional coefficient of thrust (C_T) is used. C_T, defined by McGhee as the ratio of jet thrust to the freestream dynamic pressure times the frontal area of the model, is as follows:[17]

$$C_T = \frac{T}{q_\infty S} = \frac{\dot{m}u_e + (p_e - p'_\infty)A_e}{q_\infty S} \tag{3.2}$$

The thrust coefficient in equation 3.2 was calculated using isentropic relations and the Ashkenas and Sherman (eq. 3.1) relationship for the freestream conditions. Given equation 3.1, and knowing the freestream conditions (Mach 12 flow, 300K total temperature, and 26.5 psia total pressure), as well as the desired thrust coefficients of 0.5 to 3.0 in increments of 0.5, the necessary PD stagnation pressures can be calculated. Stagnation pressures for the various models and C_T values are tabulated in Table 3.1. Note that for these calculations the total jet exit area is used; therefore, the thrust for a single jet on the quad nozzle will be a quarter of the total thrust.

	Single-Nozzle		Quad-Nozzle	
C_T	Sonic (psia)	Supersonic (psia)	Sonic (psia)	Supersonic (psia)
0.5	2.9	2.4	0.7	0.7
1.0	5.9	4.8	1.4	1.2
1.5	8.8	7.1	2.1	1.8
2.0	11.7	9.5	2.9	2.4
2.5	14.6	11.8	3.6	3.0
3.0	17.5	14.1	4.3	3.6

Table 3.1: Calculated PD model stagnation pressures for various C_T and model configuration

3.3 Optical Systems

The overall optical setup necessary for quantitative experiments is shown in Figure 3.5. As shown, the laser beam is turned by various mirrors and a beam splitter sends the majority of laser power to the laser sheet formation optics (top of the image, external to the vacuum chamber) and a small portion to a power meter, a static cell and an interferometer. The static cell is a constant-pressure cell containing iodine vapor at a pressure of 0.3 torr (I_2 vapor pressure at room temperature), and is used primarily as a reference for velocity measurements, as described in Chapter 2. The photodiode records the fluorescence intensity from the static cell, and the interferometer tracks the relative laser frequency as the laser is tuned through the gain profile. For qualitative experiments, the static cell, photodiode, and interferometer are not necessary.

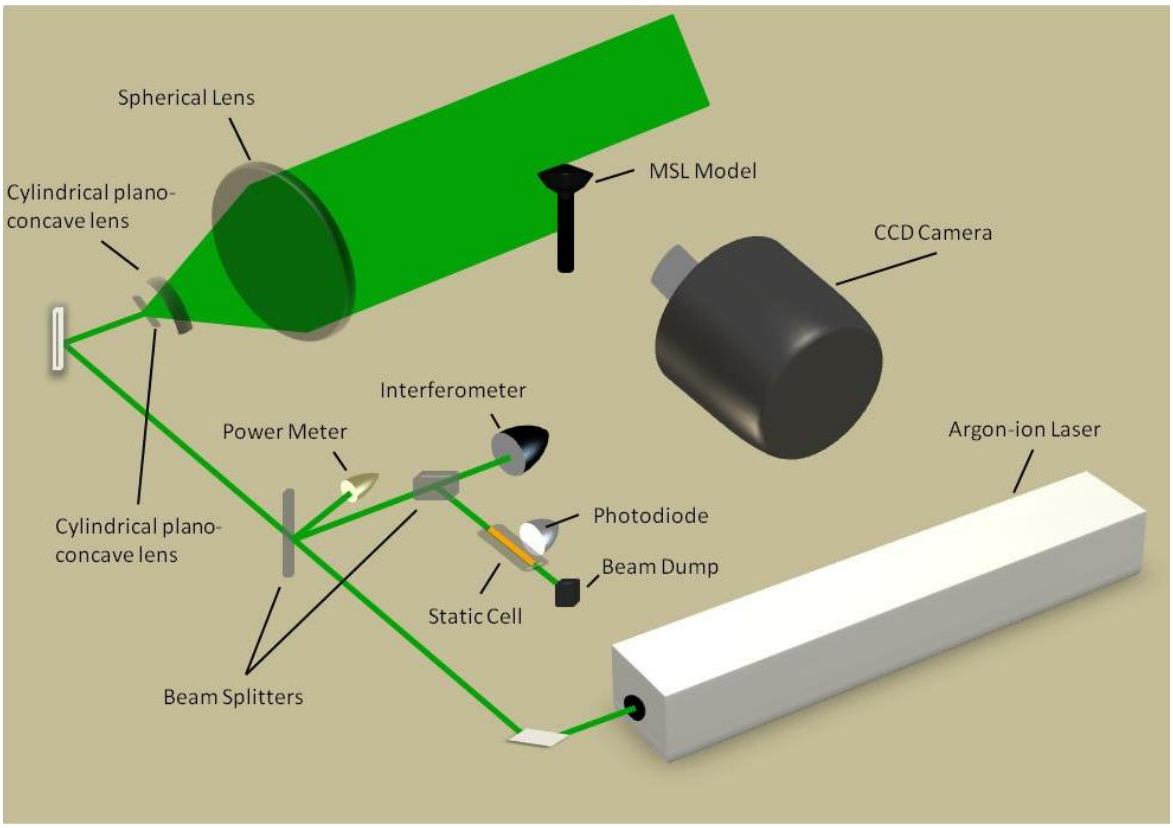

Figure 3.5: Optical setup for quantitative experiments

As mentioned previously, the laser beam is converted into a sheet and collimated with a series of three optics: a -9.7 mm cylindrical plano-concave lens, a -400 mm cylindrical plano-concave lens, and a large 330 mm spherical plano-convex lens. The focal point of the first plano-concave lens and the spherical lens are set to the same spatial point to collimate the sheet. The second cylindrical lens is used to adjust the beam waist thickness at the model, typically on the order of 0.2-0.3 mm, by modifying the location of the focal point in relation to the large spherical lens. For experiments with mirrors placed internally in the vacuum chamber, and thus with a longer path length to the model, it was necessary to change the 2nd lens to a -200 mm plano-convex lens to extend the minimal beam waist location to the position of the model.

3.3.1 CCD Camera

The imaging system used for fluorescence measurements is a 16 bit Andor iKon-L CCD camera with a resolution of 2048 x 2048 pixels, with to 15.5 ± 1.0 pixels / mm resolution in the flow and an image area of 131 x 131 mm. The camera has a high quantum efficiency of over 95% in the 500-650 nm range. Using liquid cooling, the camera is able to achieve temperatures as low as -100 °C, which reduces dark current buildup in the CCD chip, and thus the shot noise of the camera. An orange Heliopan #22 filter is used to block scattered laser radiation from the camera.

3.3.2 Laser Operation

The argon-ion laser used in the following work, a Spectra Physics 2080A, is operated in two different configurations: multi-mode operation, at flashpoint where all longitudinal modes of the laser under the gain profile are lasing, and with an intracavity etalon to select single laser modes. The laser is maintained at a constant 1.5W output for both visualizations and quantitative measurements; however, laser power does drop near the edges of the gain profile when operating

in single-mode. For single-mode operation, a Klinger stepper motor drives a mechanical gear to adjust the vertical tilt of the etalon in order to select modes of the argon-ion laser; meanwhile the laser J-lok is controlled by the DAQ system to minutely change the laser cavity length by controlling a piezoelectric transducer. If just etalon tuning is used, frequency resolution is only 87 MHz; however, by controlling the cavity length, the frequency resolution is as low as 20 MHz.

3.4 Data Collection and Analysis Method

Due to the large amount of data necessary for each experimental run, as well as the fine control of the laser cavity length, it is necessary to have a robust data acquisition system (DAQ). Reference 52 offers a thorough description of the DAQ system and processes, and only the main components will be discussed here. The DAQ system controls the laser (drives the stepper motor and piezoelectric transducer control) and camera systems, while recording various pressures and temperatures, relative laser frequency, laser power, static cell emission, and logs camera images. Recorded values are tracked in an output csv file. Images are tracked and logged (Andor Program file format, .sif images) according to data point identifiers within the csv file.

When an experiment is complete the output csv file and images are parsed, extraneous data points are deleted (repeat frequencies due to back-stepping the scan to re-adjust pressures, or laser alignment), and the corresponding images and edited csv files are moved to an individual folder for each laser-sheet angle. The image files are saved in a .sif format and the Andor computer program (camera controller program) must be used to open and convert the image files to .dat outputs. Three main components are necessary for data analysis from the csv file: laser frequency, laser power, and static cell intensity. These values are taken from the csv file and saved in an array .mat file to be used with Matlab. Relative laser frequency is common for all

spectral data (static cell and flowfield data), and is centered on the laser gain profile, with the static cell P13/R15 peak at +2 GHz (the frequency scale is relative, and the unshifted P13/R15 peak is known to be +2 GHz off-center of the argon-ion laser gain profile). A Matlab script, listed in Appendix C, loads the image files into Matlab, constructs a 3D matrix of the spectra, with x-y corresponding to fixed spatial pixel coordinates, and the z-direction being the intensity of the x-y pixel at the corresponding laser frequency. The saved Matlab matrix files are then uploaded to the UVa computer cluster and a meshgrid is constructed to run various portions of the flowfield in parallel over 100 cluster nodes. Spectra typically range from about 180 to 280 discrete frequency points, and while a spectrum is compiled for a 600x400 pixel region, the analysis region is typically 160 pixels above the model stagnation point, and 150 pixels to the left and right. This results in a total of 48,000 discrete experimental spectra to perform a least squares fit to the iodine fluorescence model, equation 2.2. To handle the large datasets, an automated data analysis script was created using Matlab, and the theoretical model was fit to the experimental data via least squares and a global optimization algorithm from Matlab's Global Optimization Toolbox. Analysis time on the cluster has been found to typically range from 8-24 hours; however, some nodes have run as long as 72 hours. Analysis quits running if the time exceeds 100 hours. A copy of the files necessary for analysis is given in Appendix B. The analysis output consists of matrix files for fitted temperature, pressure, frequency, computed frequency shift, and residual, so all fits can be re-constructed post-analysis.

CHAPTER 4: RESULTS – VISUALIZATIONS AND MOLE FRACTION

Experimental visualizations for the single- and quad-nozzle PD jet visualizations are presented and discussed in this chapter. Quantitative mole fraction results will also be presented and discussed.

4.1 Single-nozzle Retrorocket Results

4.1.1 Visualizations

A secondary objective of this research was to produce a data set that could be used for comparison with numerical results from the University of Michigan. Those computations assumed that the flow exhausted into a zero background pressure, so no shock system was computed around the freestream jet isentropic core. However, in the experiment, this shock system does exist and can interact with the PD jet model bow shock. In order for meaningful comparisons, this shock/shock interaction needed to be minimized. The model size was chosen as a compromise from being too small to fabricate and so large as to create strong interaction between the model bow shock and the freestream barrel shock. Figure 4.1 shows the shock/shock interaction (indicated by the circle) for a 2 cm aeroshell diameter PD jet model. As thrust is initiated, the bow shock is pushed away from the model forebody and the bow shock does not impinge on the model at any point. A triple point forms at the point of interaction of the model bow shock and the freestream barrel shock. It was found for even greater C_T that a large 2 cm model will eventually cause the triple point interaction to occur as high as the bow shock location itself, which caused the bow shock to appear normal instead of oblique. By comparison with preliminary CFD results it was determined that this interaction caused a strong perturbation of the shape of the model bow shock. For a 1 cm diameter model, this perturbation was deemed

small enough that no appreciable change in model bow shock occurred near the model, so a 1 cm model was selected for this research.

The current work is the second time blunt body research has been conducted in the ARL hypersonic wind tunnel. Previously, reaction control system research with a blunt body was completed, and model sizing effects were investigated. It was concluded that a 2 cm diameter model would be sufficiently small to avoid unwanted interactions of the model bow shock with the freestream barrel shock.[52] However, 2 cm models with a PD jet were found to be too large and produce significant unwanted interaction of the two shock systems. An example of the interaction of the model bow shock and freestream barrel shock is shown for a 2 cm diameter model in Figure 4.1. Freestream flow is from the top of the image down, and both the freestream and PD jet are seeded with iodine. The model stagnation point is placed at a position corresponding to Mach 12 freestream flow, and has a C_T of 1.0.

As discussed in Chapter 2, the argon-ion laser is operated without an etalon for the visualization experiments, which causes all longitudinal modes under the 514.5 nm gain profile to laze. As a result, all absorption lines of the iodine molecule under the gain profile are excited to an upper energy state and fluoresce. However, due to the Doppler effect, some absorption lines are shifted outside the laser gain profile (notably the P48/P103 peaks near the edge of the argon-ion gain profile). Also, the laser power may not be as strong near the edge of the laser gain profile (if the Doppler shift is positive, the P13/R15 peak would near the wing of the gain profile). This would result in an overall apparent loss of fluorescence, or signal level, in those areas of the flow. Due to this Doppler effect, the flowfield, as shown in Figure 4.2(a) appears asymmetric about the model centerline. Note, in Figure 4.2(a) the laser sheet propagates from the top right side of the image down to the bottom left, causing the relative motion of the iodine

molecules on the left side of the flowfield to have a positive Doppler shift, which would reduce the laser power available to the P13/R15 absorption line pair. However, there is symmetry in the PD jet flowfield (as will be shown in Chapters 5.1.1, 6.1.1, and 7.1.1), so the rest of the visualization images are all mirrored about the model centerline, as shown in Figure 4.2(b), to remove the undesired Doppler shift.

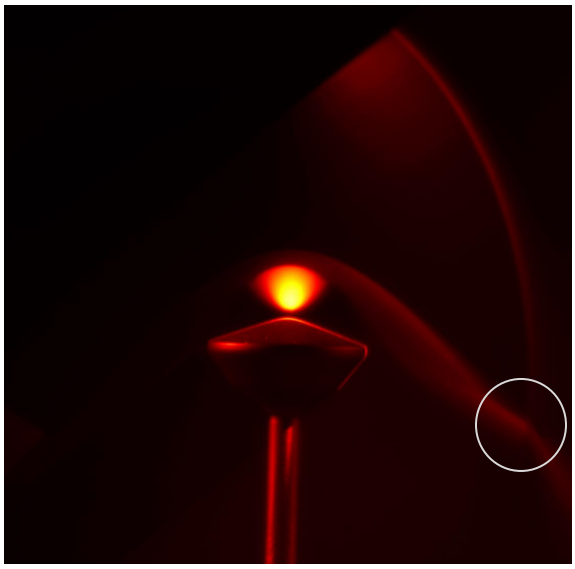

Figure 4.1: Interaction of model bow shock with freestream barrel shock due to model size, 2 cm model diameter, M_{∞} = 12.0, M_{jet} = 1.0, C_T = 1.0

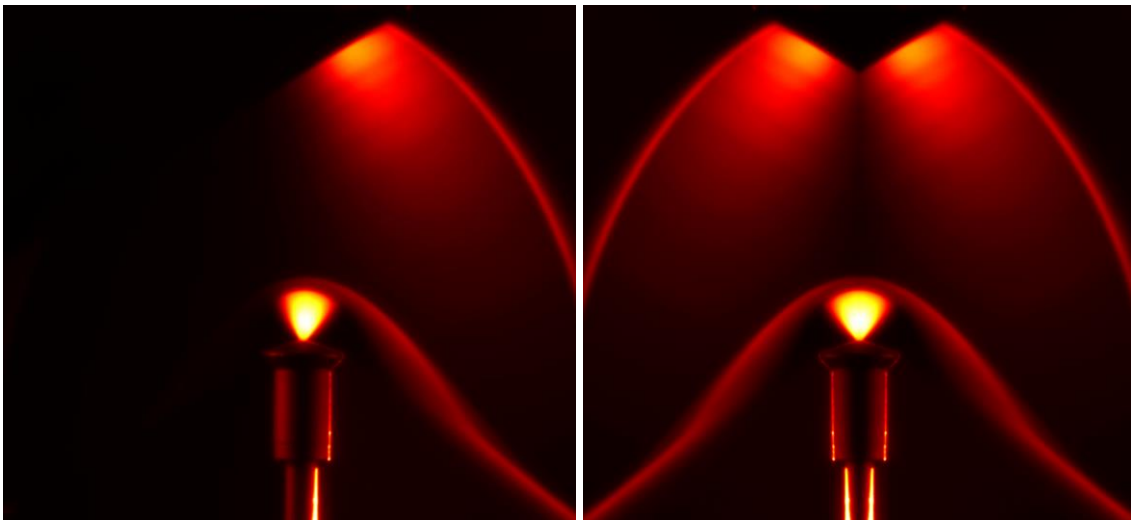

(a) Image with Doppler shift

(b) Image mirrored about model centerline

Figure 4.2: Symmetry of flowfield, 1 cm supersonic single-nozzle model, M_∞ = 12.0, M_{jet} = 1.0, C_T = 1.0

Visualization images for the sonic single-nozzle PD model ranging from C_T of 0.5 to 3.0 in increments of 0.5 are shown in Figure 4.3. Freestream flow is from top to bottom. The images are mirrored about the model centerline. From the visualizations it is evident that as C_T increases the PD jet increases in length and width, pushing the bow shock further upstream. At the lowest C_T the model bow shock nearly impinges on the model shoulder, but as C_T increases, the shock is moved farther from the shoulder. Due to the increasing width of the bow shock with increasing PD jet size, the triple point, formed by the interaction of the bow shock with the freestream barrel shock, moves upstream with increasing C_T. At the lowest C_T the triple point is located outside the laser sheet, but is visible at higher C_T, specifically for 2.5, and 3.0. Furthermore, at the greatest C_T of 3.0, the triple point has moved so far upstream that the shape of freestream barrel shock is actually affected. – it is evident the barrel shock is not as wide as for the lower C_T cases.

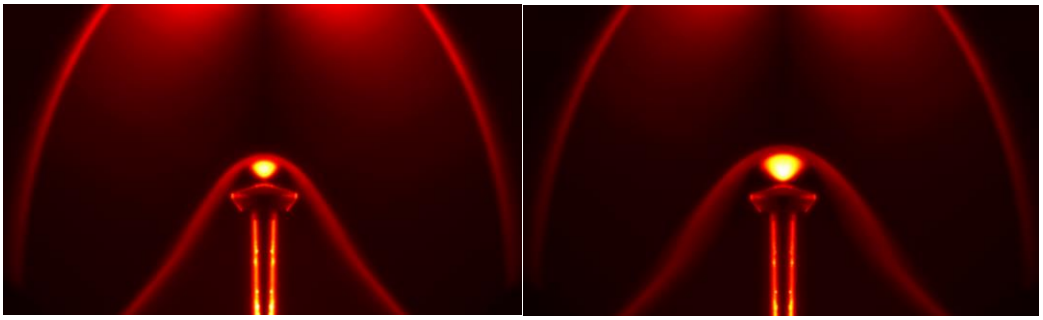

(a) C_T = 0.5 (b) C_T = 1.0

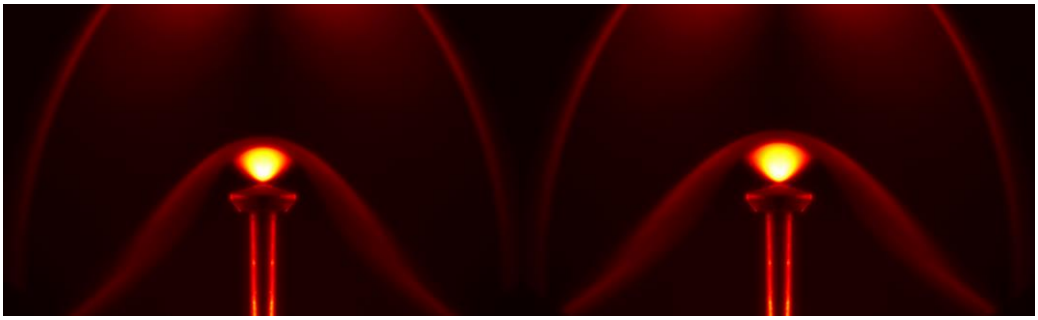

(c) C_T = 1.5 (d) C_T = 2.0

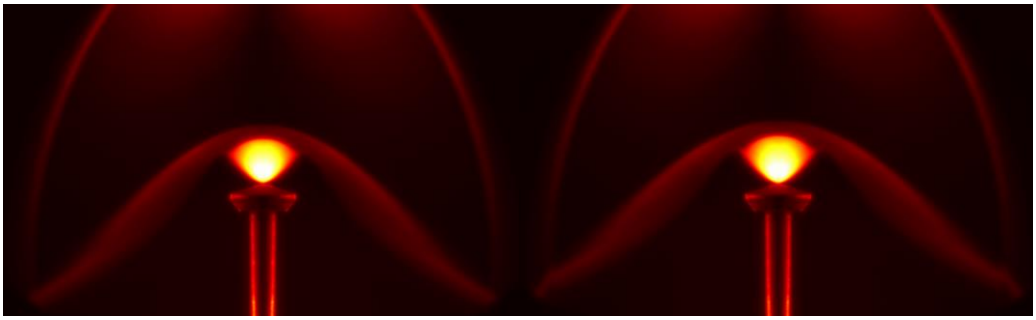

(e) C_T = 2.5 (f) C_T = 3.0

Figure 4.3: Sonic single-nozzle PD model, M_{jet} = 1.0, for range of C_T from 0.5 (a) to 3.0 (f).

Results for the supersonic single-nozzle PD jet model are shown in Figure 4.4. As expected, the supersonic jet (exit Mach number of 2.66) penetrates farther upstream than the sonic case, and thus pushes the bow model shock farther away from the model forebody than the sonic PD jet with equivalent C_T and mass flow rate. Note that, for both the single sonic and supersonic PD models, little fluorescence signal is detected outside of the PD jet boundary and above the aeroshell surface. Very few iodine molecules cross the PD shear layer to the recirculation region, and the PD jet itself shields this part of the model from the freestream flow. The significance of this will be discussed in the quad-nozzle visualization section of this chapter.

The effect of a supersonic nozzle compared with a sonic nozzle can be seen by comparing Fig 4.3(a) to 4.4(a). While the bow shock is in close proximity to the model shoulder for the sonic case at low C_T, this does not happen for the supersonic test case. Due to the greater jet penetration of the supersonic model, the triple point interaction becomes apparent at lower C_T for the supersonic test case, becoming evident by C_T of 2.0, as opposed to 2.5 in the sonic test case. Due to the increasing interaction with the freestream barrel shock at larger thrust, it was decided that quantitative experiments should be run at lower C_T to reduce the interaction because it will not be modeled by CFD. However, for realistic application of retropropulsion for a Mars lander, larger C_T would be desirable. So a C_T of 1.0 was found as a balance between a larger thrust, but still deemed sufficient to minimize interactions with the freestream barrel shock for single-nozzle models.

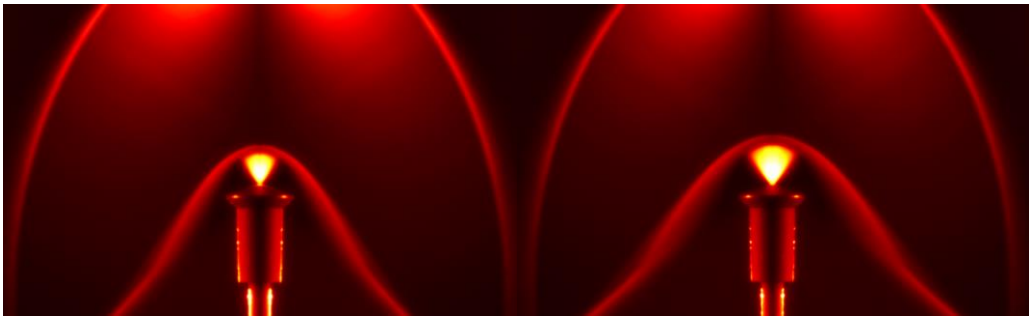

(a) C_T = 0.5 (b) C_T = 1.0

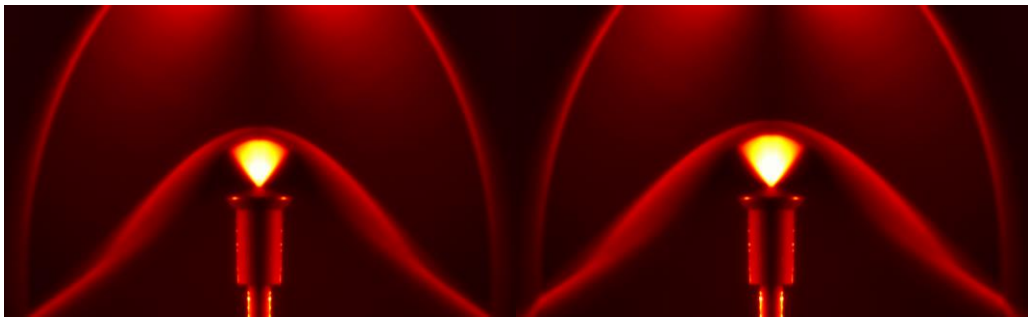

(c) C_T = 1.5 (d) C_T = 2.0

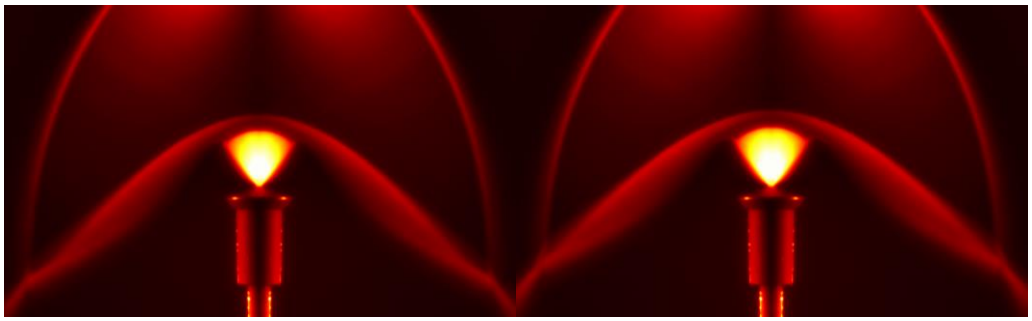

(e) C_T = 2.5 (f) C_T = 3.0

Figure 4.4: Supersonic single-nozzle PD model, M_{jet} = 2.66, for range of C_T from 0.5 (a) to 3.0 (f).

Table 4.1 is a comparison of the shock stand-off distance, SSD, for the sonic and supersonic test cases. In regions with Mach number greater than or equal to 8 the fluorescence signal is directly proportional to the number density as demonstrated in Chapter 2.[53] Thus, there is a gradient in fluorescence signal as the flow begins to pass through a shock. The SSD is taken as the point where the fluorescence signal has increased by 10% above the freestream "background" level. The SSD is normalized to the model frontal diameter for the sonic and supersonic cases. The uncertainty is measured as ±3 CCD camera pixels in the region between the shock and model surface locations, and ±3 pixels in the model diameter. Combining these uncertainties for the ratio of SSD to model diameter results in an uncertainty of ±0.03 for all cases and is indicated as a percentage uncertainty in the table. Evident from the images, the supersonic SSD is greater than the sonic SSD for all C_T, being between 28-32% greater.

	SSD / D_{model}	
C_T	Sonic	Supersonic
0.5	0.50 ± 6.0%	0.64 ± 4.7%
1.0	0.63 ± 4.8%	0.83 ± 3.6%
1.5	0.74 ± 4.1%	0.95 ± 3.2%
2.0	0.82 ± 3.7%	1.06 ± 2.8%
2.5	0.90 ± 3.3%	1.15 ± 2.6%
3.0	0.97 ± 3.1%	1.25 ± 2.4%

Table 4.1: Comparison of sonic and supersonic shock stand-off distance normalized by model diameter, with uncertainties shown

4.2 Quad-nozzle Retrorocket Results

4.2.1 Visualizations

Figures 4.5 and 4.6 are experimental PLIIF visualizations of the sonic and supersonic peripheral 4-jet PD models, respectively, at C_T from 0.5 to 3.0 in increments of 0.5. The visualization images were taken with iodine seeded in the freestream and PD jet. Freestream flow is from the top of the images to the bottom. The forebody of the model MSL aeroshell is placed at the Mach 12 location in the hypersonic underexpanded jet test flowfield. In these images only two of the four jets are visible since the laser sheet passes through the center of two jets only. Furthermore, the flowfields are symmetric, so the images are mirrored about the model centerline to remove the Doppler shift effect which is otherwise observed in the fluorescence images.

The sonic PD jets (Fig. 4.5) are underexpanded jets much like the freestream flowfield. The PD jets exit the orifice at Mach 1 and freely expand until they terminate in the jet shock. The bow shock is preserved above the stagnation region of the model forebody, but the PD jets cause the shock to be pushed away from the model forebody.

Figure 4.6 is the supersonic peripheral 4-jet PD model and has a jet exit Mach number of 2.66. Much like the sonic case, the bow shock is preserved above the stagnation region of the model but is pushed further upstream than the sonic case due to greater penetration by the supersonic jets. The sonic PD jets have a greater jet turning angle than the supersonic jets. Fluorescence downstream of the PD jets (around the shoulder of the model) is observed for both the sonic and supersonic cases up to $C_T = 1.5$, unlike for the single-jet models. By comparing visualizations to computational fluid dynamics, it was found that this fluorescence is from freestream jet fluid that compresses in the bow shock, moves to the model surface, and flows

outward on the surface of the model, separating around the PD jet, and re-attaching on the side of the PD jet near the shoulder. Fluorescence in this area isn't visible for higher C_T because as jet thrust increases the PD jet becomes larger, causing the re-attachment region to occur farther out towards the model shoulder, until finally no reattachment occurs. Thus no freestream fluid would be visible in the plane of the laser.[58]

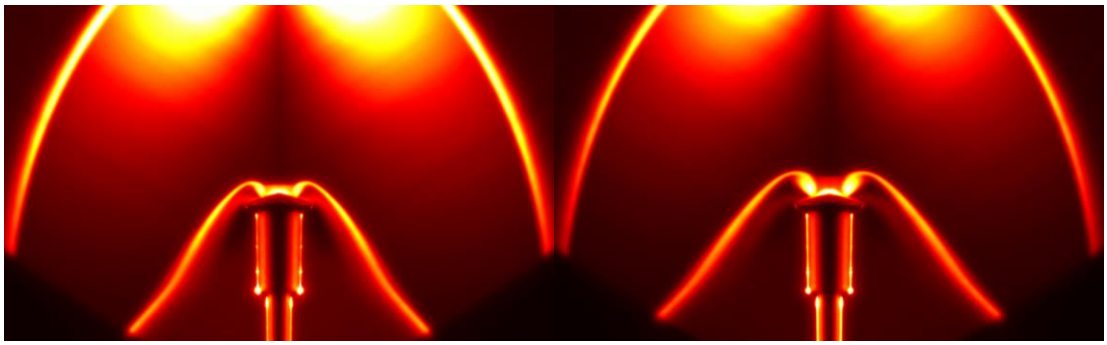

(a) C_T = 0.5 (b) C_T = 1.0

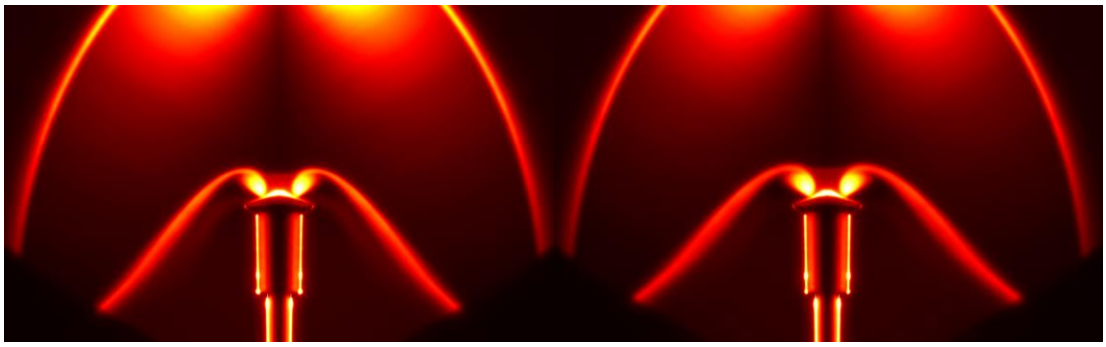

(c) C_T = 1.5 (d) C_T = 2.0

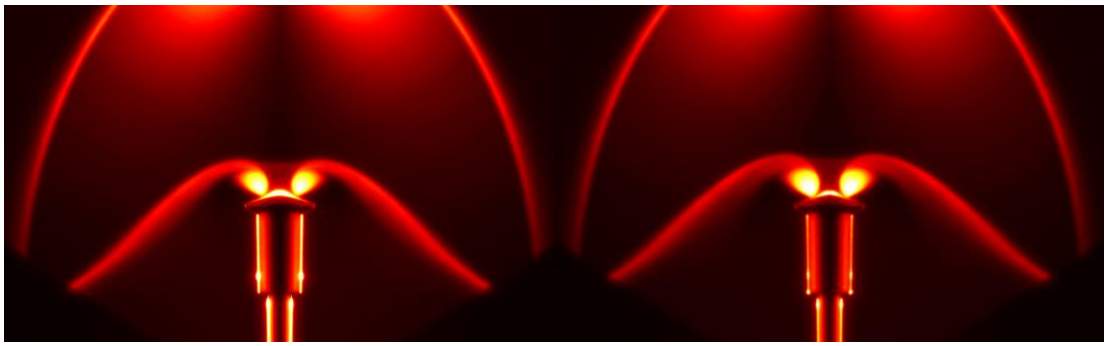

(e) C_T = 2.5 (f) C_T = 3.0

Figure 4.5: Sonic peripheral quad-nozzle PD model, M_{jet} = 1.0, for range of C_T from 0.5 (a) to 3.0 (f).

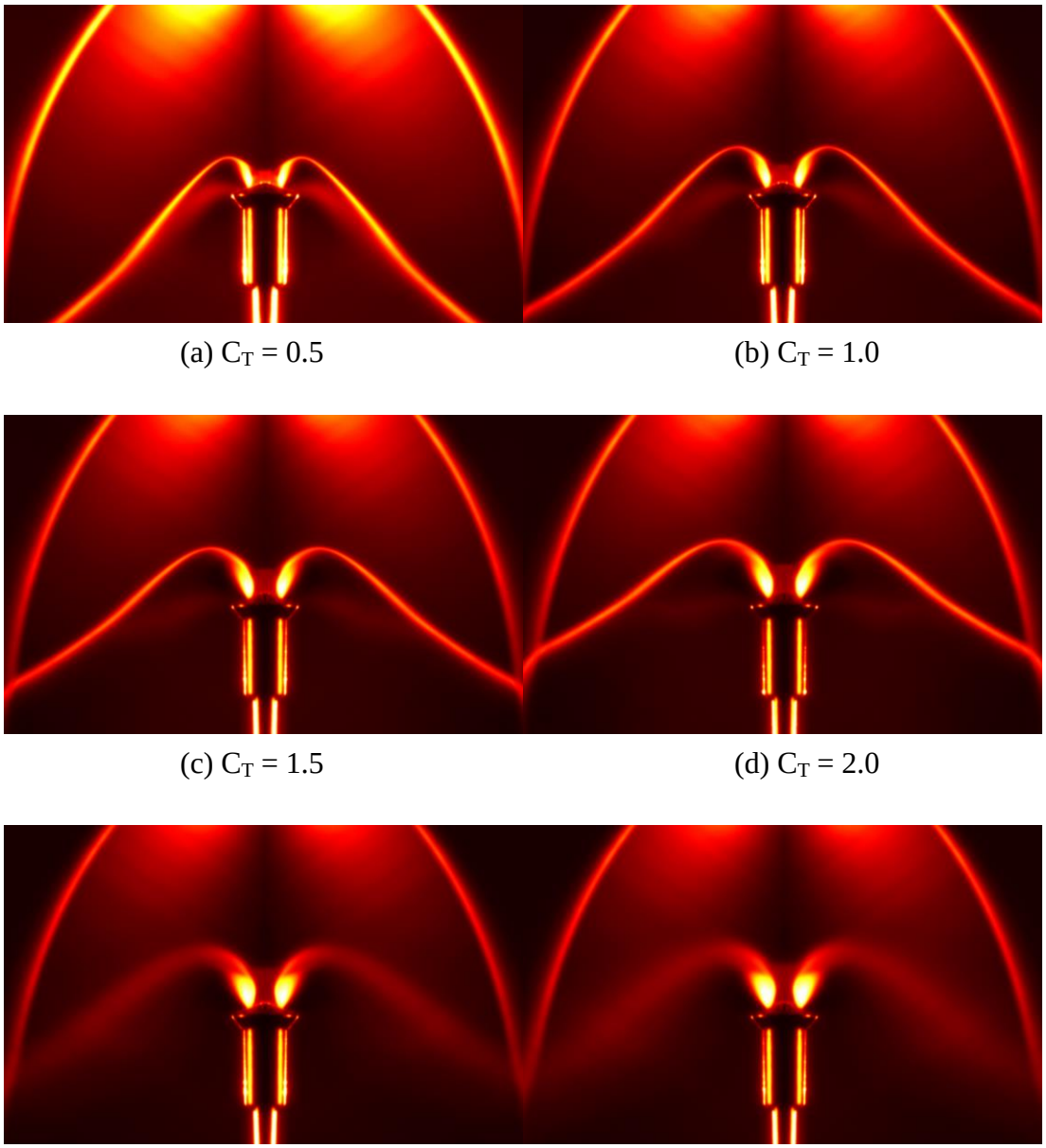

(a) C_T = 0.5 (b) C_T = 1.0

(c) C_T = 1.5 (d) C_T = 2.0

(e) C_T = 2.5 (f) C_T = 3.0

Figure 4.6: Supersonic peripheral quad-nozzle PD model, M_{jet} = 2.66, for C_T from 0.5 (a) to 3.0 (f).

Table 4.2 is a comparison of the SSD, and maximum upstream PD jet penetration distance for the sonic and supersonic quad-nozzle test cases. Unlike the single-nozzle cases, the stand-off distance for the quad-nozzle supersonic model is approximately the same as the sonic case until a C_T of 1.5. For C_T of 3.0 the shock stand-off distance is about 18% greater for the supersonic case. The same method for calculating SSD, described in the previous section, is used to obtain the maximum PD jet penetration, which is the point furthest upstream where the shock begins to form directly upstream of the PD jet. As seen in Table 4.2, the maximum PD jet penetration distance, normalized to the model aeroshell diameter, reflects the trends seen in the images. The supersonic jets extend further into the freestream than the sonic jets for all C_T tested, even for small C_T where the shock stand-off is roughly the same. The penetration distance for the supersonic case is approximately 50% greater than the sonic case at $C_T = 3.0$.

	SSD / D_{model}		Jet Penetration / D_{model}	
C_T	Sonic	Supersonic	Sonic	Supersonic
0.5	0.14 ± 21%	0.14 ± 21%	0.19 ± 16%	0.28 ± 11%
1.0	0.23 ± 13%	0.23 ± 13%	0.34 ± 8.8%	0.48 ± 6.3%
1.5	0.32 ± 9.4%	0.32 ± 9.4%	0.43 ± 7.0%	0.64 ± 4.7%
2.0	0.38 ± 7.9%	0.40 ± 7.5%	0.47 ± 6.4%	0.80 ± 3.8%
2.5	0.45 ± 6.7%	0.49 ± 6.1%	0.53 ± 5.7%	0.86 ± 3.5%
3.0	0.50 ± 6.0%	0.59 ± 5.1%	0.60 ± 5.0%	0.90 ± 3.3%

Table 4.2: Comparison of sonic and supersonic shock stand-off distance and jet penetration normalized by model diameter for quad-nozzle configuration, with uncertainties shown

4.2.2 Mole Fraction

Quantitative mole fraction images were also obtained using PLIIF. By taking the ratio of a jet-only seeded image to a full-flow seeded image (Fig 4.7(a) divided by 4.7(b)), and normalizing the ratio by the value at the PD jet exit where the jet mole fraction is unity, a jet mole fraction image results, as discussed in Chapter 2.[53] The fluorescence above the center of the model, between the PD jets, is only visible in the full flow seeded case (Fig 4.7(b)) which indicates the fluid in this region of the flowfield is primarily from compressed fluid behind the bow shock from the freestream, and thus that drag should be preserved in this area. Also, in Fig 4.7(a) with no freestream iodine, no fluorescence is evident near the shoulder of the model, which confirms attributing the fluorescence observed in freestream-seeded flows, to the recombination of the freestream fluid flowing over the model surface and around the PD jet, as discussed in the previous section.

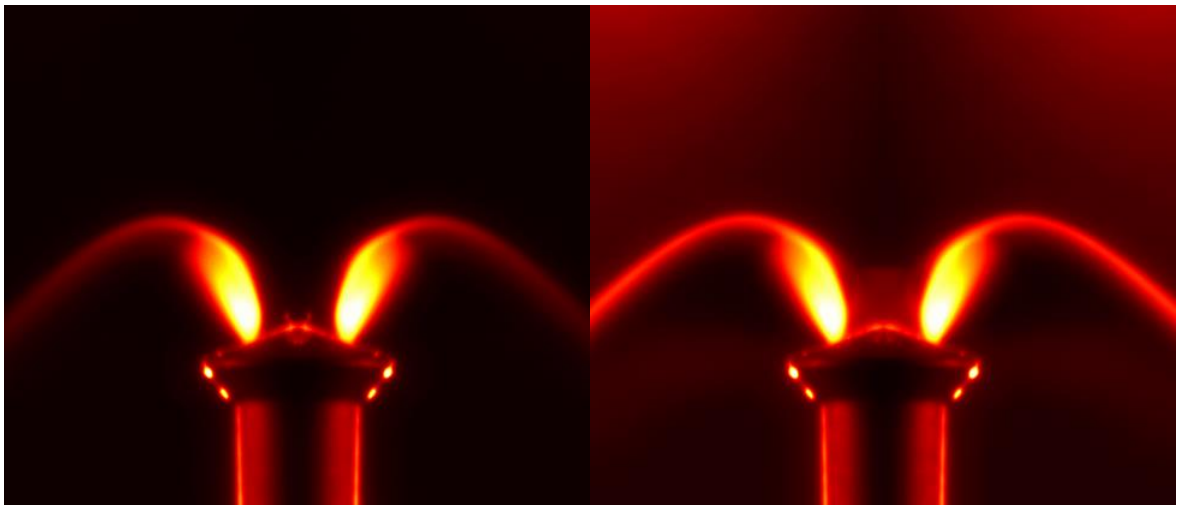

(a) C_T = 1.5, jet only seeded (b) C_T = 1.5, full flow seeded

Figure 4.7: Supersonic peripheral 4-jet PD model, M_{jet} = 2.66, for two iodine seeding cases

The resulting mole fraction images are shown in Fig 4.8 for the sonic and supersonic PD jet models for a C_T of 1.5. The color contours give spatially-resolved quantitative values of the local jet mole fraction at each CCD pixel (64 μm resolution), which are due to the PD jet mixing with the Mach 12 freestream. These quantitative images provide the opportunity to validate CFD results, as will be shown in the next section. For both the sonic and supersonic cases the PD jet mole fraction is unity, or near unity, throughout the entire PD jet core as would be expected. The PD jet fluid begins to turn and it mixes with the freestream flow, and continues to mix as both the freestream and PD fluid progress downstream. The area between the PD jets is shown to be less than 15% PD jet fluid, thus confirming the fluorescence seen in this area of the flow in the visualizations is due to the preserved bow shock between the PD jets.

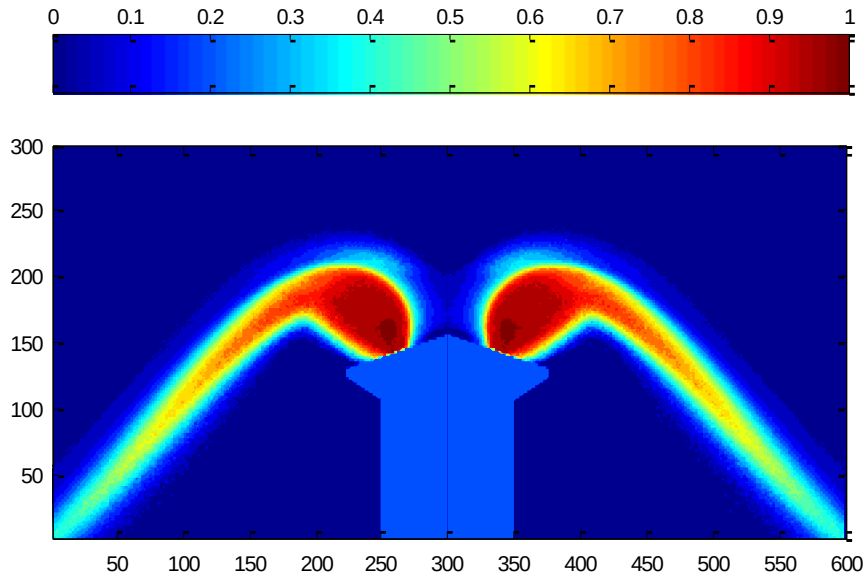

(a) Sonic peripheral 4-jet PD model, M_{jet} = 1.0

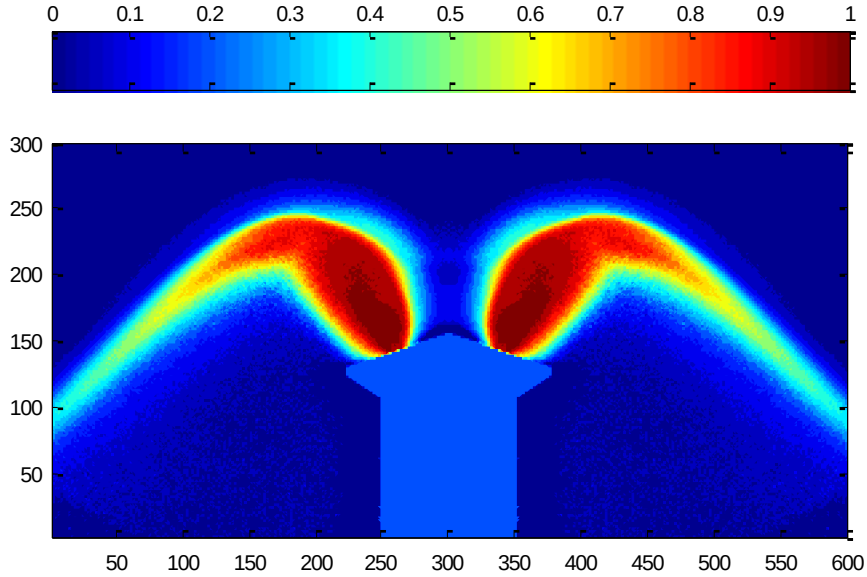

(b) Supersonic peripheral 4-jet PD model, M_{jet} = 2.66

Figure 4.8: Experimental 4-jet PD mole fraction images, C_T = 1.5

4.3 Numerical Simulation Comparisons

Experimental results will be compared with numerical simulations from the University of Michigan executed using LeMANS, a parallelized CFD code for simulating hypersonic reacting flows.[54-56] LeMANS solves the laminar three-dimensional Navier-Stokes equations on unstructured computational grids, including thermo-chemical nonequilibrium effects. The transport properties can be calculated using several options. For this study, mixture transport properties were calculated using Wilke's semi-empircal mixing rule with species viscosities calculated using Blottner's model and species thermal conductivities determined using Eucken's relation. The finite-volume method applied to unstructured grids is used to solve the set of partial differential equations. Time integration is performed using a point implicit or line implicit method.

The flow is modeled assuming that the continuum approximation is valid.[57] Furthermore, for this work it is assumed that the translational and rotational energy modes of all species can be described by two different temperatures, T_{Tra} and T_{Rot} while the vibrational and electronic energy modes of all species are frozen at the stagnation value. In order to accurately simulate the flow in the experimental facility, I_2-seeded N_2 gas is used in the numerical simulations with a seeding ratio of 200 ppm. In the freestream, the rotational temperature is assumed to be equal to the translational temperature. Also, the Ashkenas and Sherman relations for the freestream flow serves as input to LeMANS at the upstream boundary. Results from the experimental and CFD LeMANS calculations from the University of Michigan will be compared to assess the physical accuracy of the computations for the sonic and supersonic test cases discussed in Ref. 58.

4.3.1 Single-nozzle PD Comparison

Figure 4.9 and 4.10 are experimental images of the single-nozzle PD sonic and supersonic cases, respectively, with CFD calculated streamlines (top half) and of computed model bow shock locations (dashed lines in bottom half). The sting of the model is removed from the image and a rendering of the model superimposed for illustrative purposes. Shock comparisons are made for C_T of 0.5, 1.0, 2.0, and 2.5 and the freestream flow is from left to right in these images. The CFD calculations begin in the PD jet plenum and calculate the flow through the jet nozzle. The CFD shock contour, shown by the dashed line in the bottom of the images in Figure 4.9 and 4.10 corresponds to the location where density begins to increase from freestream values along the aeroshell centerline. The bow shock profile can also be determined by the velocity streamline profile as the location where the slope of each streamline changes abruptly.

Shown in Figure 4.9, the sonic PD jet fluid expands from the jet exit until a terminal shock and decelerates to subsonic speeds. The freestream fluid compresses in a normal bow shock over the subsonic region and decelerates to subsonic speeds. Between the PD terminal shock and freestream bow shock a free stagnation point forms, at which point the PD jet fluid and freestream fluid turn radially outward, and flow downstream past the model shoulder. Overall, there is good agreement in the shock stand-off distance directly above the central axis of the sonic model for all C_T tested. The streamlines agree well near the model centerline, but have a greater turning angle radially outward from the centerline of the model. The off-axis discrepancy is likely due to the interaction of the freestream barrel shock with the augmented bow shock, which is not accounted for in the CFD computations.

The supersonic comparison, shown in Figure 4.10, overall has the same flowfield characteristics the sonic case. Agreement between the experimentally measured bow shock and

CFD computed shock location is good for the lowest C_T compared, 0.5. At larger C_T the experimental SSD is consistently greater than the computational results and there is more discrepancy in the model bow shock shape. These discrepancies are due to the greater interaction of the augmented bow shock with the freestream shock system. The supersonic model jet penetrates farther upstream, causing the bowshock to move farther upstream and thus interaction between the model bow shock and the freestream shock structure to increase. It was observed in tests of the first blunt body models tests, with a 2 cm model diameter, that as the interaction of the model bow shock and freestream shock system increased the bow shock became more normal, and moved farther upstream. The discrepancy between the CFD results and experimental results are also evident in the computed streamlines, which consistently predict a greater jet turning angle, and hence a more oblique shock structure than that measured in the experiments. Because of the shock/shock interaction, it was decided to use smaller C_T for the following quantitative measurements; however, in general, larger C_T is desirable for actual PD applications, so, with the exception of mole fraction results, the quantitative results are for a C_T of 1.0, where the shock/shock interaction is not as significant.

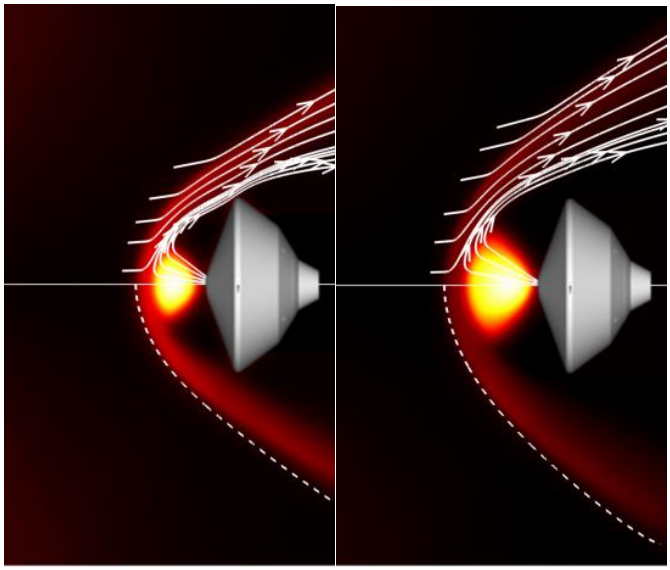

(a) $C_T = 0.5$ (b) $C_T = 1.0$

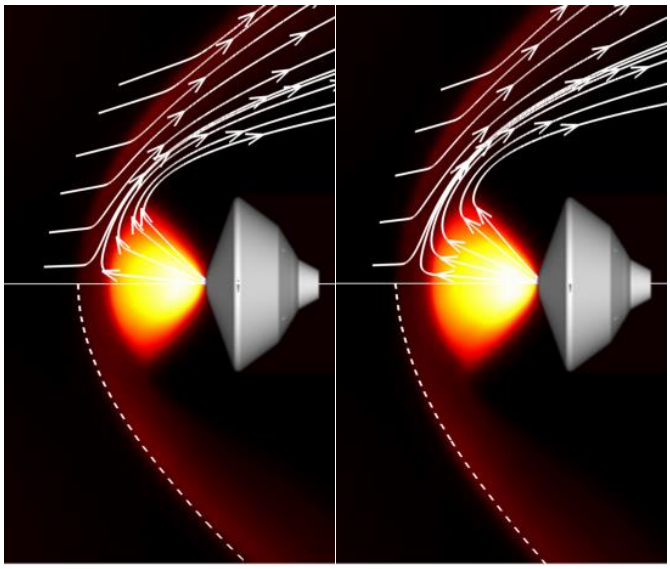

(c) $C_T = 2.0$ (d) $C_T = 2.5$

Figure 4.9: Numerical calculation of streamlines overlaid on experimental visualizations, $M_{jet} = 1.00$.[31] Streamlines are shown in the upper half of the image and model bow shock boundary is shown in the bottom half.

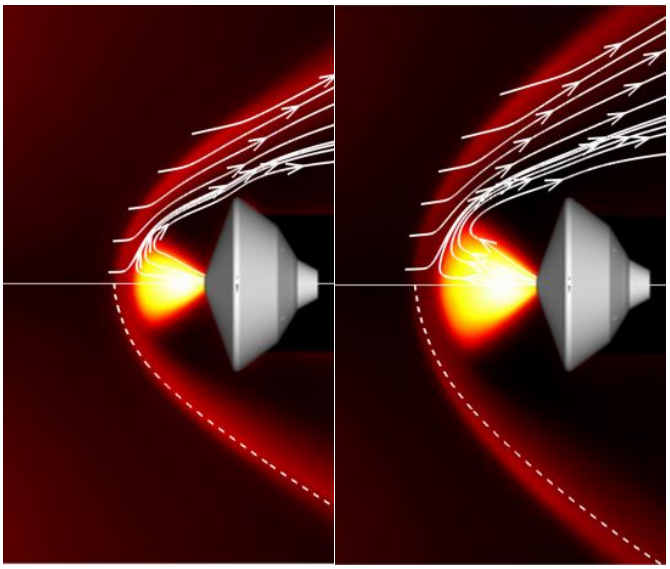

(a) $C_T = 0.5$ (b) $C_T = 1.0$

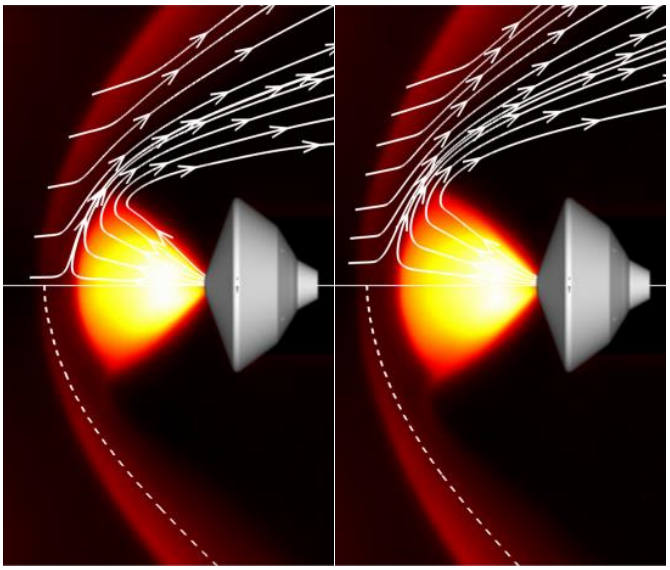

(c) $C_T = 2.0$ (d) $C_T = 2.5$

Figure 4.10: Numerical calculation of streamlines overlaid on experimental visualizations, $M_{jet} = 2.66$.[31] Streamlines are shown in the upper half of the image and model bow shock boundary is shown in the bottom half.

Experimentally measured SSD is compared with the computational results in Figure 4.11 for the single-sonic and supersonic PD models. Overall, there is good agreement in the SSD for the sonic mode for all C_T tested, with the computational results lying within the uncertainty (shown by the error brackets) of the experiment for the entire range of C_T. The supersonic model does not compare as well. The computed SSD is within experimental uncertainty for the lowest C_T tested, but diverges at larger C_T. As mentioned previously, this may be due to the interaction of the model bow shock with the freestream shock structure, which is not accounted for in the CFD results. Computed SSD for the supersonic model are within experimental uncertainty only for the lowest C_T., at larger C_T the experimental SSD is consistently greater than the computational results. This discrepancy may be due to the greater PD jet penetration distance upstream, which causes the shock/shock interaction to become more apparent.

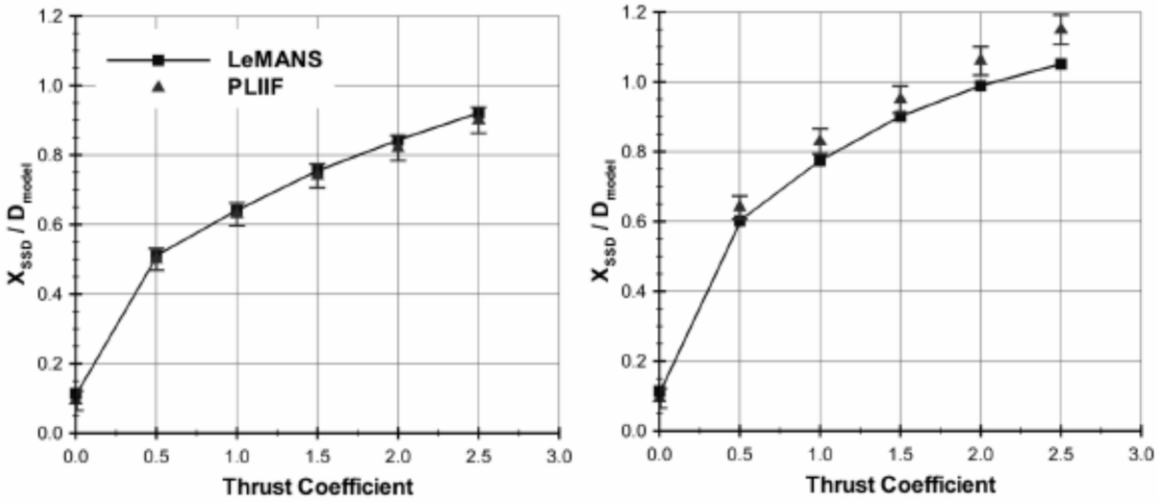

(a) Sonic Model (b) Supersonic Model

Figure 4.11: Numerical calculation of X_{SSD}/D_{Model} for single PD jet combined with experimental visualization measurement

4.3.2 Quad-nozzle PD Comparison

Figure 4.12 and 4.13 are experimental images of the quad-nozzle PD sonic and supersonic cases, respectively, with CFD calculated streamlines (top half) and of computed model bow shock locations (dashed lines in bottom half). The sting of the model is removed from the image and a rendering of the model superimposed for illustrative purposes. Shock comparisons are made for C_T of 0.5, 1.0, 2.0, and 2.5 and the freestream flow is from left to right in these images. The CFD calculations begin in the PD jet plenum and calculate the flow through the jet nozzle. The CFD shock contour corresponds to the location where density begins to increase from freestream values. The bow shock profile can also be determined by the velocity streamline profile as the location where the slope of each streamline changes abruptly.

For the quad-sonic PD model, Fig. 4.12, there is overall good qualitative agreement between the experimental PLIIF images and the velocity streamlines and density contours calculated by LeMANS, especially between the PD jets upstream of the aeroshell. Unlike the single-jet case, SSD over the centerline of the model is well-predicted and in good agreement with the experimental results. The supersonic comparison shown in Fig 4.13 also shows good agreement between LeMANS calculations and the experimental measurement for C_T of 0.5 and 1.0. However, for C_T of 2.0 and 2.5 it is seen that the computed shock location is farther downstream than in the measurement. Again, a possible explanation is that in the experiment there may be a strong interaction of the model bow shock and the shock structure of the freestream. As discussed earlier, the supersonic PD jets penetrate further upstream than the sonic case, which may cause greater interaction than in the sonic case.

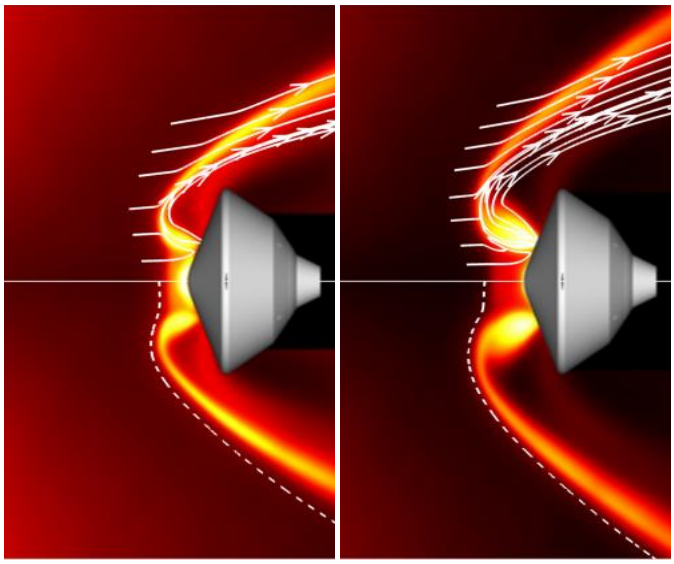

(a) $C_T = 0.5$ (b) $C_T = 1.0$

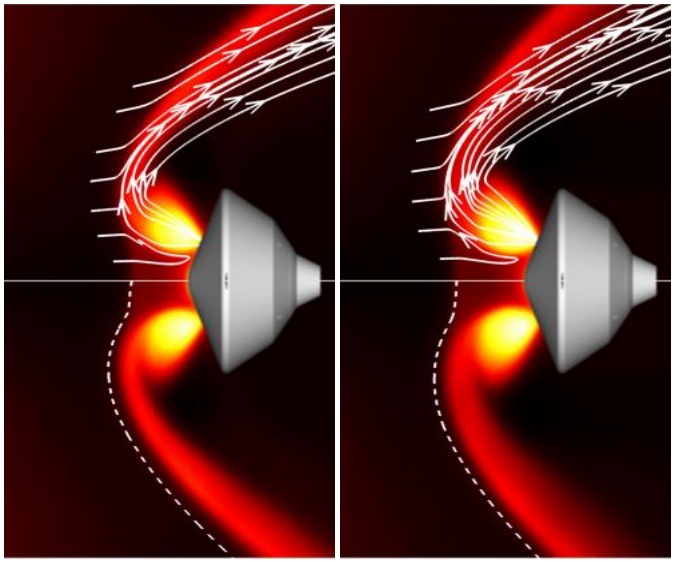

(c) $C_T = 2.0$ (d) $C_T = 2.5$

Figure 4.12: Numerical calculation of streamlines overlaid on experimental visualizations, $M_{jet} = 1.0$, quad-nozzle configuration

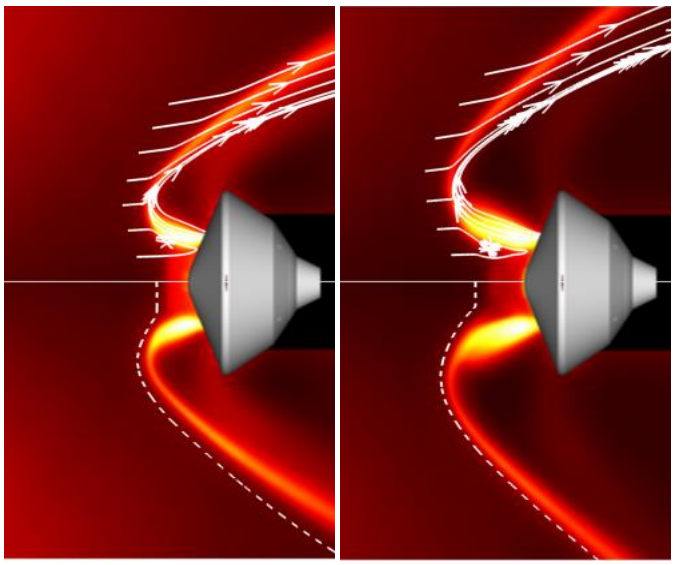

(a) $C_T = 0.5$ (b) $C_T = 1.0$

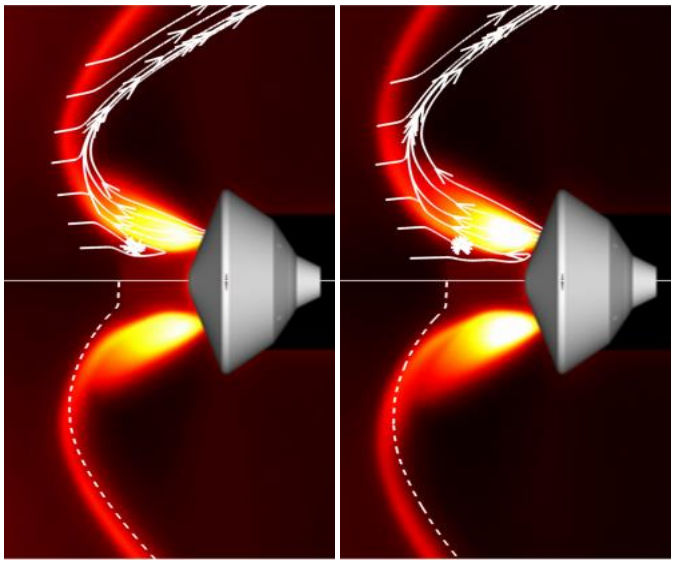

(c) $C_T = 2.0$ (d) $C_T = 2.5$

Figure 4.13: Numerical calculation of streamlines overlaid on experimental measurement, $M_{jet} = 2.66$, quad-nozzle configuration

The shock stand-off distance upstream of the aeroshell centerline versus C_T for CFD calculations and the experimental results is compared in Fig 4.14 for the sonic (a) and supersonic (b) quad-nozzle PD models. Once again the shock stand-off distance is normalized by the model

diameter. For the CFD results the shock location corresponds to the location where the density begins to increase above freestream values. The experimental shock location is calculated as previously described, by taking the point where fluorescence has increased 10% above the freestream fluorescence values. The error bars correspond to the uncertainty discussed previously. Comparisons of the numerical and experimental results shows differences of 12% and 17% for the sonic and supersonic cases, respectively, at C_T = 2.5. The good agreement suggests that shock/shock interactions away from the aeroshell centerline, as observed in Fig 4.13, may not have a significant effect on the flowfield properties near the aeroshell centerline.

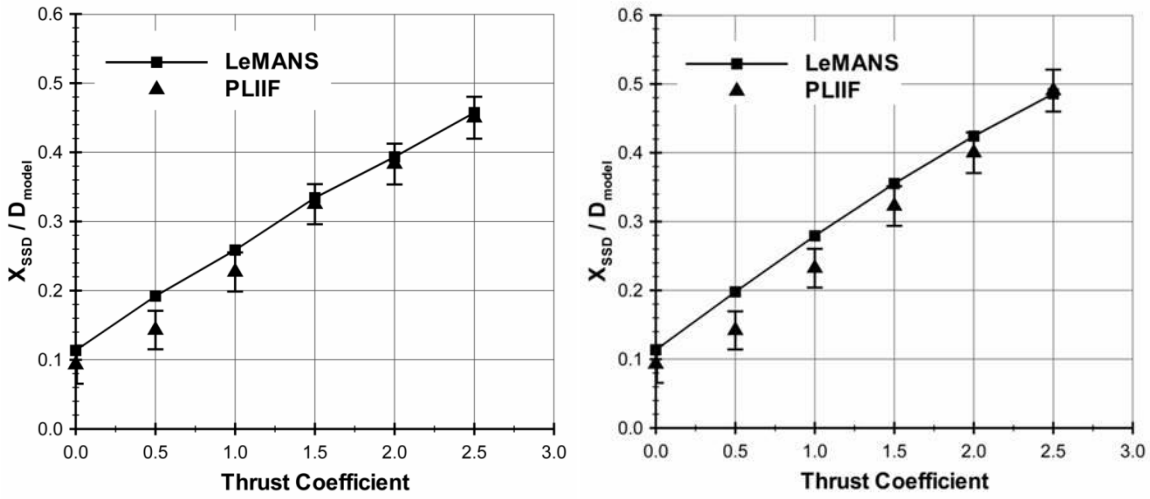

(a) Sonic Model (b) Supersonic Model

Figure 4.14: Numerical calculation of X_{SSD}/D_{Model} combined with experimental visualization measurement

4.3.3 Mole Fraction Comparison

Quantitative comparisons between CFD and experimental PD jet mole fraction for the sonic quad-nozzle PD jet model are shown in Fig 4.15 for a C_T of 1.5. Overall there is good agreement between the CFD calculations and the experimental results. Discrepancies arise after the shoulder of the model where the CFD shows greater turning of the jet fluid around the model shoulder. These differences could be attributed to multiple factors. The first of which is continuum breakdown which can occur for global Knudsen numbers greater than 0.05.[58] As shown in Ref 58, regions on the aftbody of the capsule approach a global Knudsen numbers of 1. Another possible cause is due to the much heavier iodine molecule, which may not track the nitrogen molecules as the flow turns the aeroshell corner due to low bimolecular collision rate in the more rarefied region aft of the forebody. However, since the pressure is very low on the vehicle aft body this discrepancy will not have a significant impact on the vehicle drag coefficient, which is important in the preservation of aerodynamic drag by the quad-nozzle configurations.

Figure 4.16 is a plot of the PD jet mole fraction versus the distance along lines A and B in Fig 4.15 for the CFD calculations and PLIIF. Line A originates at the jet exit and follows along the jet centerline. The sharp drop in jet mole fraction across the jet boundary and shock is clearly visible along line A, with very good comparison shown. Line B is normal to line A and is located 3 nozzle exit diameters downstream of the exit. Increasing distance along line B indicates moving toward the shoulder of the model, as shown in Fig 4.15. Once again the jet mole fraction drops off sharply across the PD jet boundaries. Greater penetration into the freestream for the experimental case is seen for distance greater than 5.5 mm along line A, and distances less than 2 mm along line B. The increased fluid turning as calculated around the model shoulder is seen in

profile B for distances greater than 2 mm. Overall very good agreement is seen between the quantitative PLIIF mole fraction profiles and the CFD predictions.

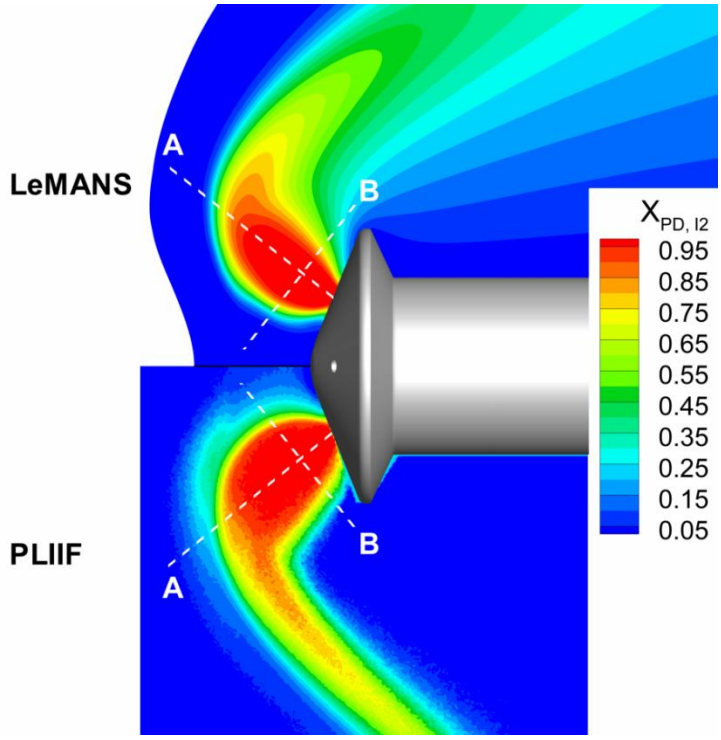

Figure 4.15: Experimental PD jet mole fraction compared to CFD, M_{jet} = 1.0, C_T = 1.5

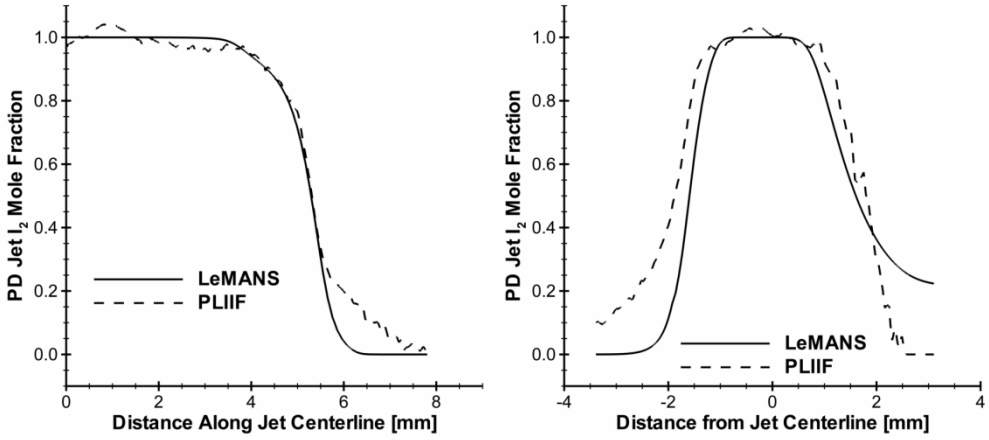

(a) Line A (b) Line B

Figure 4.16: Experimental jet mole fraction and CFD comparison along two profiles shown in Figure 4.15

Figure 4.17 is a quantitative comparison between CFD calculations and experimental results for the supersonic PD jet mole fraction at $C_T = 1.5$. The experimental results show greater PD jet penetration. Furthermore, like the sonic case, the LeMANS computations reflect a greater PD jet turning angle than the experimental results. The PD jet mole fraction versus distance for lines A and B are shown in Fig 4.18. Line A, along the jet centerline, shows significantly greater jet penetration, as seen for the experiment in Fig. 4.17. Line B also shows good agreement between calculations and experiment (located 2 jet-exit diameters from the jet exit); however, the broader PD jet profile, is seen in the experimental results as well as the increased jet fluid around the aeroshell shoulder in the CFD result.

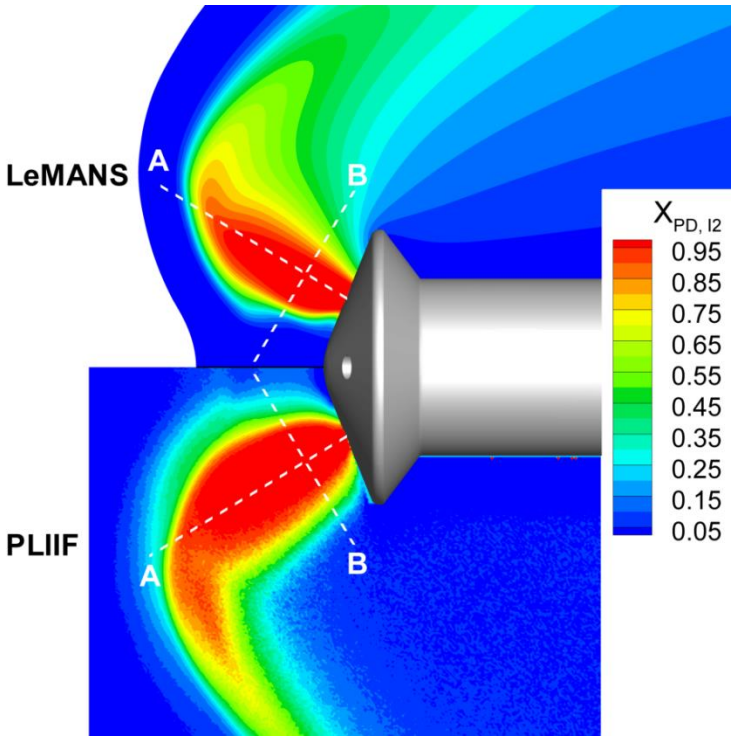

Figure 4.17: Experimental PD jet mole fraction compared to CFD, M_{jet} = 2.66, C_T = 1.5

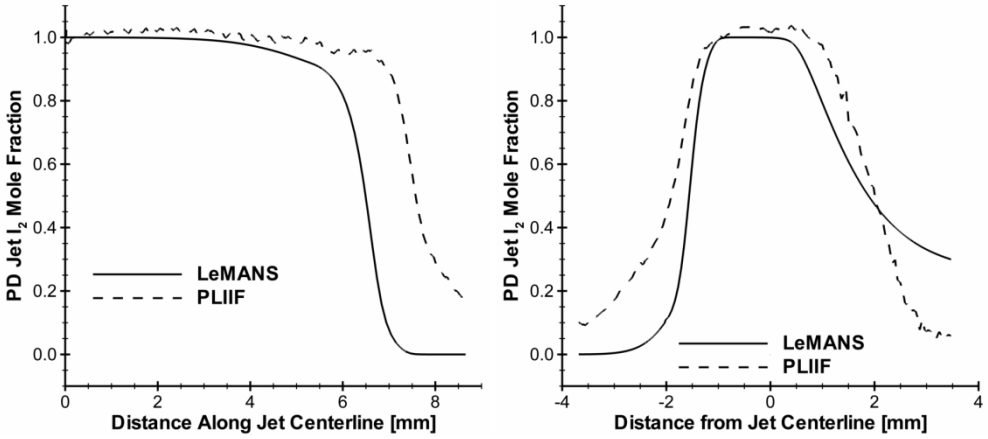

(a) Line A (b) Line B

Figure 4.18: Experiment jet mole fraction and CFD comparison

4.4 Conclusion

Experimental qualitative planar laser-induced iodine fluorescence flow visualizations have been presented and discussed for single and multiple sonic and supersonic peripheral jets on a Mars Science Laboratory frontal aeroshell at Mach 12. Experimental results for the range of thrust coefficients from 0.5 to 3.0, in increments of 0.5, have demonstrated that the bow shock is pushed farther upstream from the aeroshell forebody as C_T increases for all cases studied. The single-nozzle configuration effectively shields the aeroshell forebody from the freestream fluid and bow shock, while the quad-nozzle test case indicates a preserved bow shock between the jets, thus possibly preserving aerodynamic drag. Preservation of drag is important for PD applications because it means less retrorocket thrust would need to be applied to slow the vehicle, and thus percent mass fraction rocket of fuel would be lower, allowing more weight to be dedicated to mission payload. Both the supersonic single and quad-nozzle models have a larger shock stand-off distance at high C_T than the sonic model counterpart. The supersonic single-nozzle shock stand-off varies between 28-31% greater than the sonic model. However, for the quad-nozzle configuration, the shock stand-off distance is roughly equivalent for thrust coefficient less than 2.0. However, for thrust coefficient greater than 2.0 the shock stand-off for the supersonic model is greater than the sonic, being 18% greater for thrust coefficient of 3.0.

Quad-nozzle jet penetration was also calculated, and shown to increase for all thrust coefficients. Further, the supersonic jet penetrates farther upstream than the sonic for all test cases, resulting in approximately 50% greater jet penetration for the supersonic case at a thrust coefficient of 3.0. Further quad nozzle observations include a greater propulsive decelerator jet turning angle and broader jet boundary in the sonic case. Finally, fluorescence between the model shoulder and PD jet boundary was noted at lower C_T, but not evident at higher C_T. Mole

fraction results confirm the fluid between the PD jets is from the freestream. This suggests that the freestream fluid compressed by the bow shock is separating around the PD jet, and re-attaching near the model shoulder for lower C_T, but does not re-attach at higher C_T, as no fluorescence, and hence freestream fluid, is noted in the laser sheet plane.

Computational fluid dynamic calculations appear to capture the major flow characteristics seen in the experimental results. Overall there is good qualitative agreement between shock structure and calculated streamlines and shock location for the sonic propulsive decelerator models for thrust coefficient ranging from 0.5 to 2.5. Agreement between experimental results and computation results is not as good for the supersonic PD jet models. The supersonic PD jets penetrate farther upstream, likely increasing effects from the shock-shock interaction, causing discrepancies off-centerline. Quantitative mole fraction calculations are shown to be in good agreement with the experimental results through the propulsive decelerator jet core and on a cross-sectional cut through the jet core for both sonic and supersonic test cases; although, there is some difference around the model shoulder, where calculations predict greater fluid turning in both cases, and the supersonic jet penetrates further into the freestream experimentally.

Due to the shock-shock interactions observed in the visualization results at large thrust conditions, a C_T of 1.0 was chosen quantitative velocity and temperature measurements reported in subsequent Chapters. This thrust condition is deemed small enough to minimize the shock-shock interactions, but large enough to be interesting for application of HRP PD jets for Mars missions.

CHAPTER 5: QUANTITATIVE SINGLE-SONIC PD RESULTS

Experimental velocity and temperature results for the single-sonic PD model will be presented in this chapter. Flowfield velocity magnitude, streamlines, vectors, and planar temperature using three separate solution methods will be presented and discussed. Comparisons to CFD results from the University of Michigan will be made for purposes of validation.

5.1 Single-sonic PD Velocity

5.1.1 Symmetry of Flowfield

Because the symmetry of the flowfield is an important assumption to solve for velocity using the method described in Chapter 2, verifying the symmetry of the experimental flowfield is desirable. As shown in Chapter 4, broadband visualization images caused the flowfield to appear asymmetric due to the Dopper effect, where signal intensity levels are lower for portions of the flowfield with iodine absorption peaks shifted outside of the argon-ion gain profile; however, it is possible to negate the Doppler effect by creating a "Doppler-free visualization" from the narrowband frequency data. The Doppler-free image is created by integrating (summing) the signal level over a single iodine absorption transition, in this case the P13/R15 peak which is not Doppler-shifted outside of the argon-ion gain profile in any portion of the flowfield. Figure 5.1 shows the resulting Doppler-free visualization image constructed from the measured iodine absorption spectrum. Freestream flow is from top to bottom, x/D and y/D of zero correspond to the center of the PD jet exit, and the laser sheet is at 27.9-deg from the horizontal going from the top right of the image to the bottom left. From the Doppler-free visualization it is apparent the flowfield is symmetric.

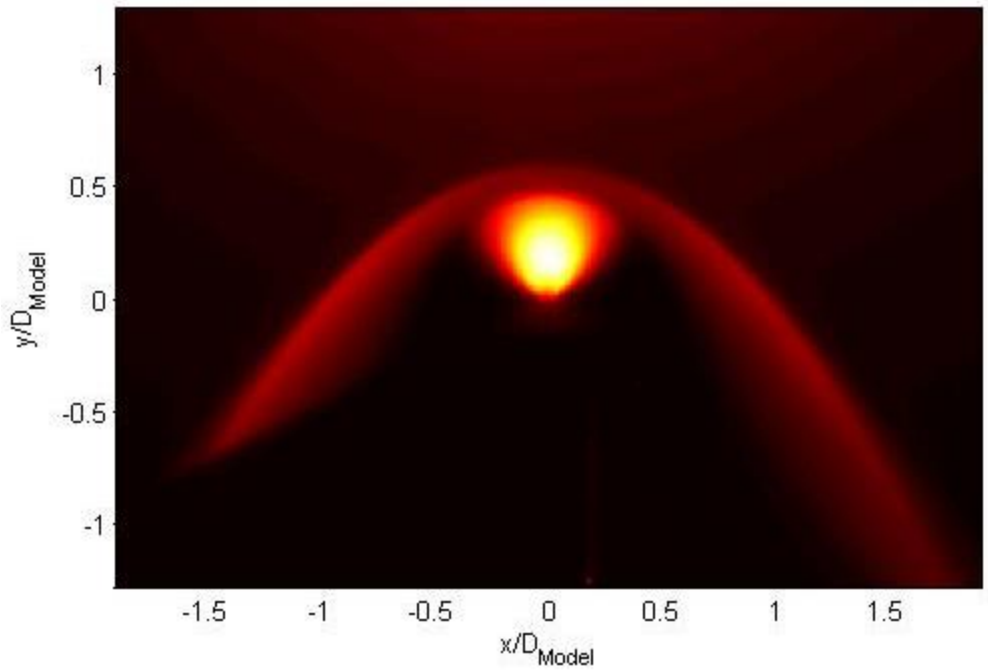

Figure 5.1: Single-sonic PD jet Doppler-free visualization, C_T = 1.0, M_{jet} = 1.0, M_∞ = 12.0

5.1.2 Flowfield Characteristics

Planar velocity flowfield magnitude and streamlines for the single-sonic PD jet at a C_T of 1.0 are shown in Figure 5.2. The 2D velocity vector field at reduced resolution (every seventh pixel), is shown in Figure 5.3(a) and an image with finer resolution (every second pixel) in Figure 5.3(b) focuses on a small region of interest. Velocity was measured as discussed in Chapter 2, with impact shift cancelled through symmetry of the flowfield about the model centerline. Due to cancelling impact shift, the velocity vectors are only resolved for one half of the flowfield, positive x/D, and mirrored about the centerline. In accounting for the limited optical access, the laser sheet angles were set to 27.9-deg and 2.3-deg from the horizontal. The freestream flows from top to bottom and the retrorocket jet exit is centered at y/D and x/D of zero, where D corresponds to model diameter of 10 mm. One of the angles for the laser sheet results in blocked laser light on the backside of the model, thus preventing the cancellation of impact shift in the

flow for negative y/D at the model surface. For the subsequent discussion *upstream* will refer to increasing y/D, and *radially outward* to positive or negative x/D.

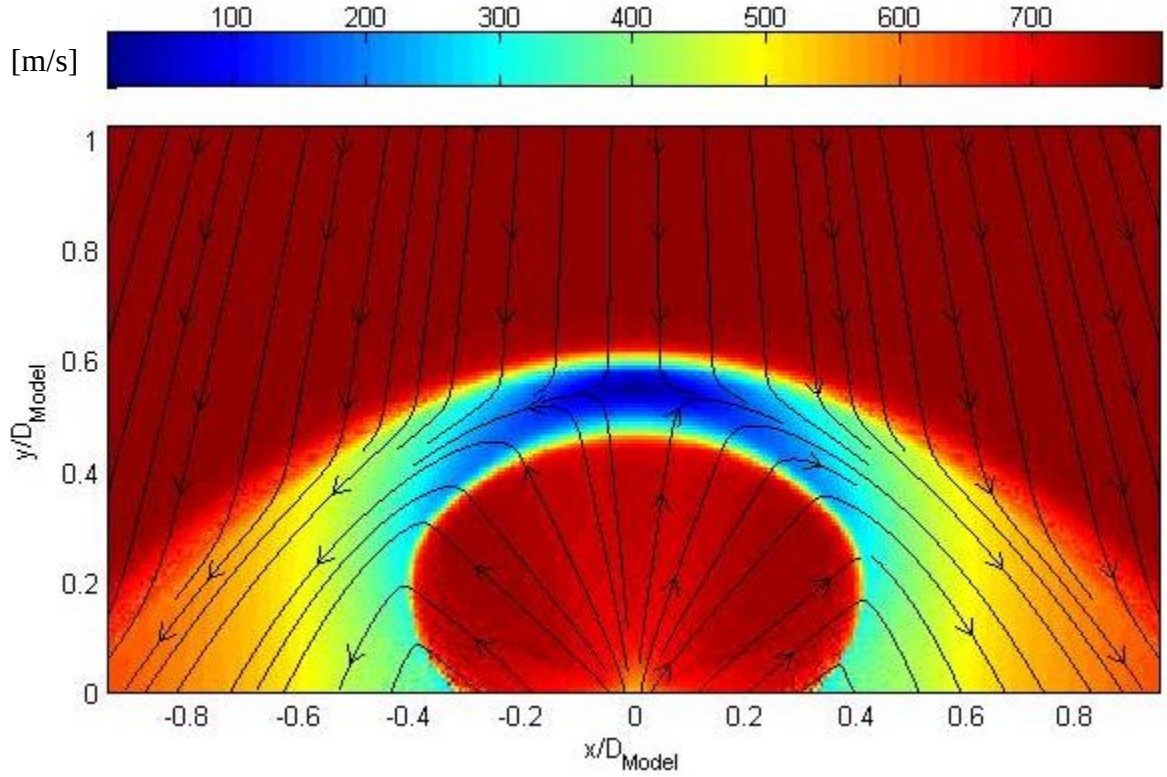

Figure 5.2: Single-sonic PD jet magnitude and streamlines, C_T = 1.0, M_{jet} = 1.0, M_∞ = 12.0

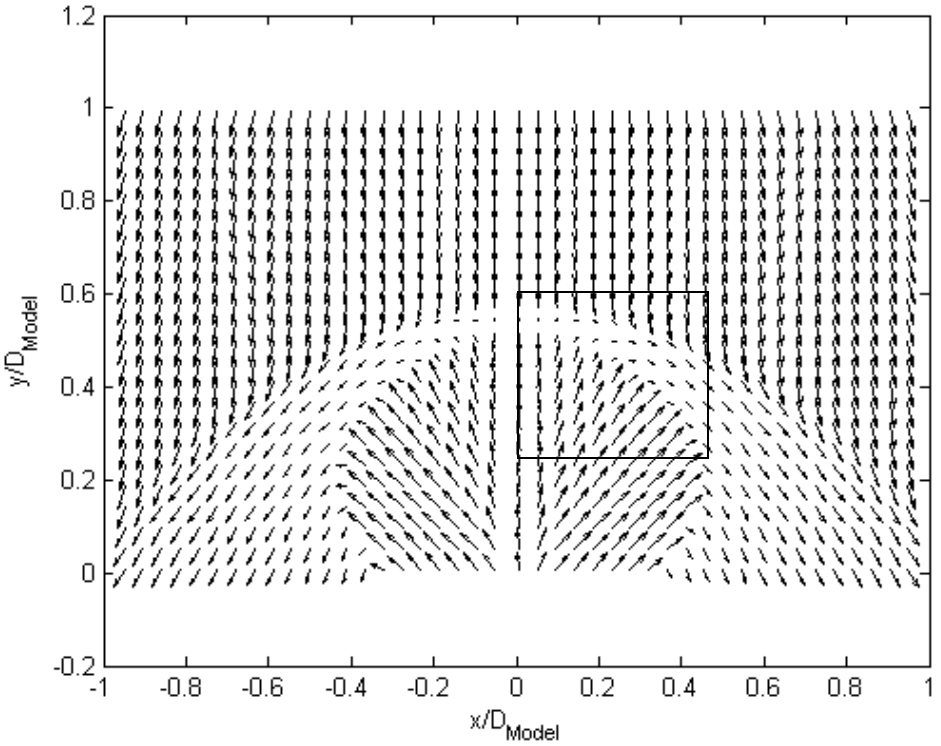

(a) 2D Velocity Vector for every 7th pixel

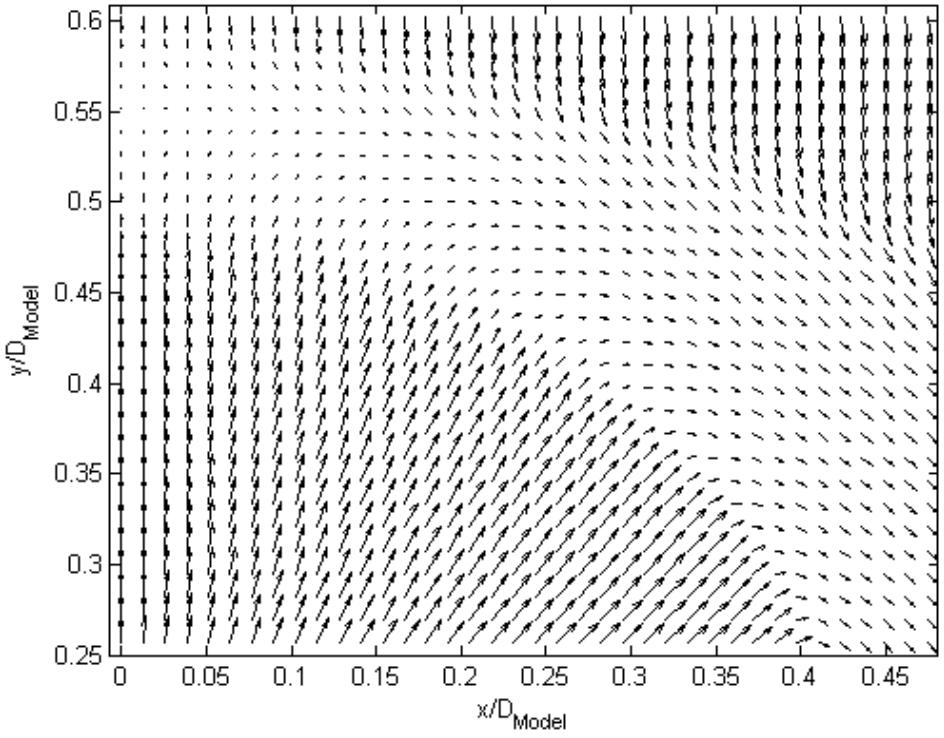

(b) 2D Velocity Vector for interaction region of PD jet and freestream flow, every 2nd pixel,

Figure 5.3: Single-sonic PD jet planar velocity vectors, C_T = 1.0, M_{jet} = 1.0, M_∞ = 12.0

The following is a discussion of the flowfield features seen in Figure 5.2 and 5.3, as labeled in Figure 5.4. It is evident in these figures that the PD jet expands from the jet exit before terminating at the shock, after which the flowfield slows to subsonic velocities. The freestream flow forms a normal shock on the centerline of the model and upstream of the subsonic region, and decelerates the freestream flow to subsonic speeds. A free stagnation point forms between the PD jet terminal shock and model shock. At the free stagnation point an effective contact surface forms (viscous effects are likely small in this region of the flow, which will be discussed in subsequent chapters) and the PD jet fluid and freestream fluid turn and accelerate radially outward around the PD jet plume and then downstream, past the PD jet boundary and model shoulder. The PD jet fluid compresses in an oblique shock at the boundary, and abruptly turns downstream. This area is shown in more detail in the higher resolution image, Figure 5.3(b). The abrupt change in flow direction results in a region with large shear, and is where viscous effects (to be discussed in the following sections) are expected to be the most significant.

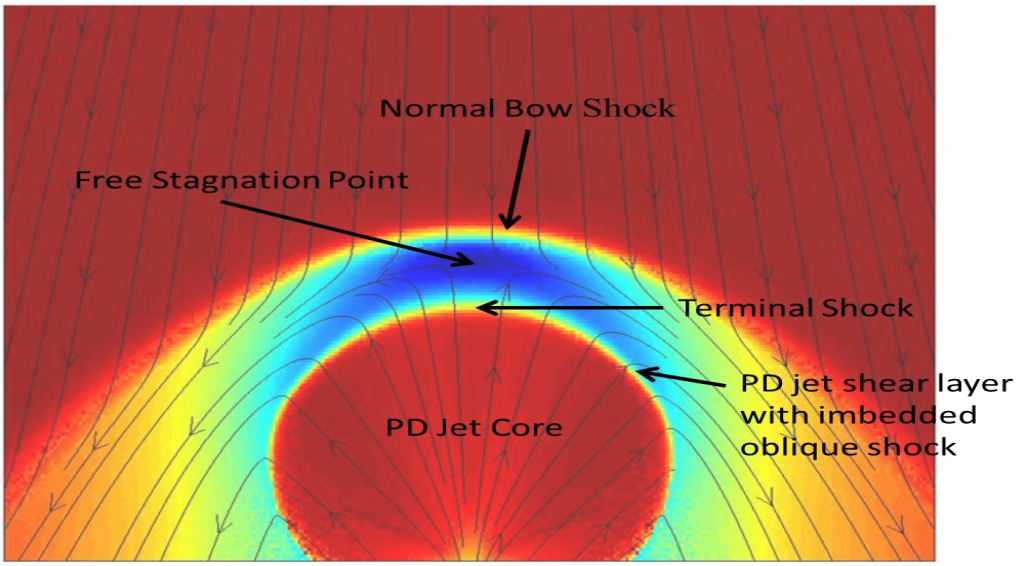

Figure 5.4: Flowfield features overlaid on Figure 5.1

5.1.3 Strain Tensor

With the spatially-resolved planar velocity field it is possible to calculate a two dimensional strain tensor, which is given by equation 5.1:

$$E_{ij} = \frac{1}{2}\left(\frac{\partial u_i}{\partial j} + \frac{\partial u_j}{\partial i}\right) \tag{5.1}$$

The resulting analysis for the sonic test case is shown in Figure 5.5 with the flowfield streamlines. E_{xx} and E_{yy} correspond to expansion (positive values) or compression (negative values) in the respective x and y directions and the off-diagonal terms E_{xy} and E_{yx} correspond to shearing strains. Because the strain tensor is symmetric, E_{xy} is equal to E_{yx}, and thus only E_{xy} is shown. Once again, freestream flow is from top to bottom, and the retrorocket nozzle exit is located at x/D and y/D of 0. Note, only half of the flowfield is shown in these images due to flow symmetry. It is seen that the fluid strain is very low in most regions of the flowfield, being concentrated in localized regions. Large horizontal compression is indicated in E_{xx} in the shear layer, labeled in Figure 5.4, across which the flow is abruptly turned by an oblique shock, as well as in the freestream bow shock. A compression is also seen in E_{yy} in these same regions. Shearing strain, E_{xy}, is evident off-centerline in the model bow shock, and in the PD jet shear layer where the PD jet fluid compresses in an oblique shock, and is subsequently turned downstream. Areas in the flowfield where these shearing components are large are indicative of where viscous effects are significant, which will be important to note for the subsequent section where an inviscid fluid is assumed to compute the flowfield temperature. It is also possible to calculate flow vorticity as defined by the following equation:

$$\omega_z = \frac{\partial u_y}{\partial x} - \frac{\partial u_x}{\partial y} \tag{5.2}$$

Vorticity for the sonic retrorocket test case is shown in Figure 5.5(d). The greatest vortices are located in the shearing region on the PD jet boundary where the PD jet and freestream fluid from the subsonic region is flowing downstream as the PD jet fluid off-axis is expanding upstream.

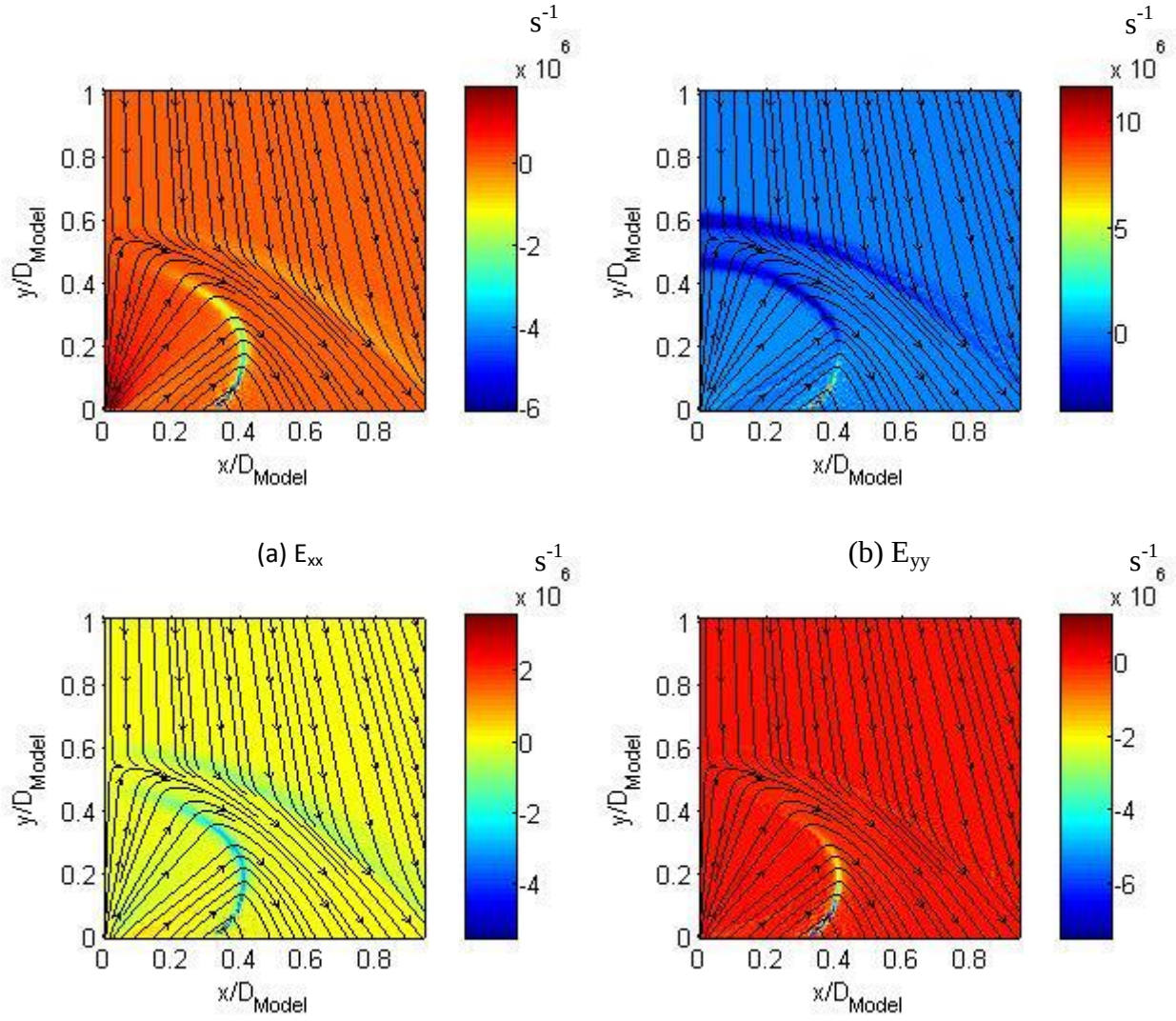

(a) E_{xx} (b) E_{yy}

(c) E_{xy} (d) Vorticity

Figure 5.5: Components of 2D stress tensor, C_T = 1.0, M_{jet} = 1.00, M_∞ = 12.0

5.1.4 Impact Shift

In this section the overall effect on the flowfield velocity measurement is discussed if impact shift is neglected. The velocity magnitude computed using the total measured frequency shift.

Doppler and impact shift (equation 2.22) is shown in Figure 5.6(a), while the velocity magnitude calculated from the Doppler shift alone is in Figure 5.6(b). As can be seen the effect of the impact shift on most of the flowfield is negligible. The difference becomes apparent in Figure 5.7, which shows the percent difference in velocity magnitude between Figures 5.6(a) and (b). The most notable difference in the computed velocity is an apparent asymmetry to the flowfield when impact shift is neglected. The asymmetry is direction-dependent, with higher velocities occurring in locations with a negative Doppler shift, and lower velocities in areas with a positive Doppler shift. This is due to the fact that the impact shift is a function of thermodynamic properties, and thus always causes the iodine absorption to shift to lower frequencies. In these figures the laser sheet is from left to right, resulting in a positive Doppler shift for positive x/D; thus a negative impact shift makes the velocity magnitude appear to be slightly less than at negative x/D where the Doppler shift is negative. Areas of the flow with a negative Doppler shift have an artificially large velocity magnitude, while areas of the flow with a positive Doppler shift have an artificially smaller velocity magnitude. This is most notable in the bow shock, where the percent difference is negative for positive x/D, and positive for negative x/D.

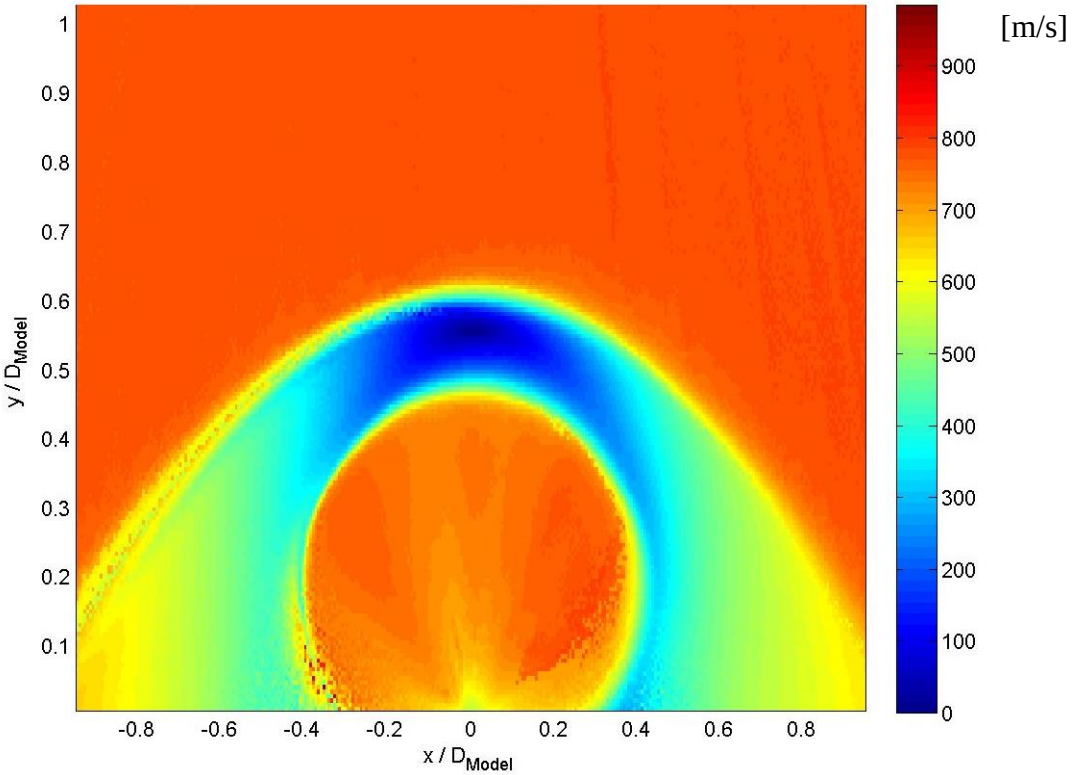

(a) Calculated velocity magnitude from measured total shift

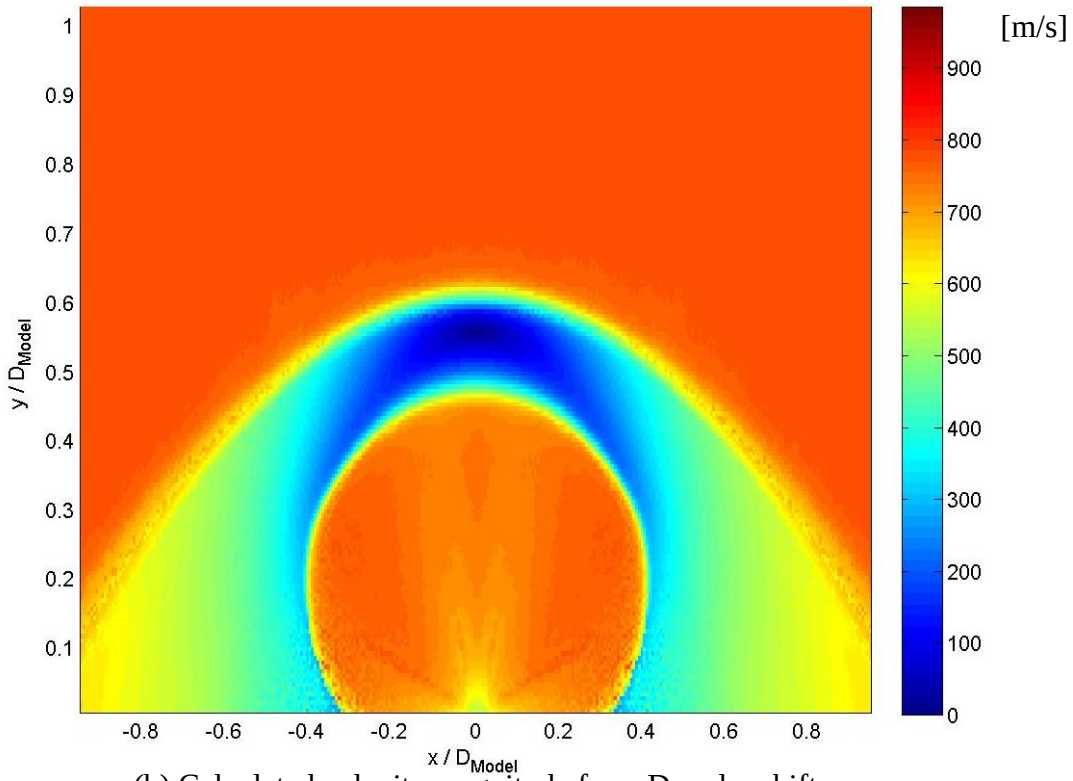

(b) Calculated velocity magnitude from Doppler shift

Figure 5.6: Effect of impact shift on single sonic PD jet velocity magnitude, C_T = 1.0, M_∞ = 12.0

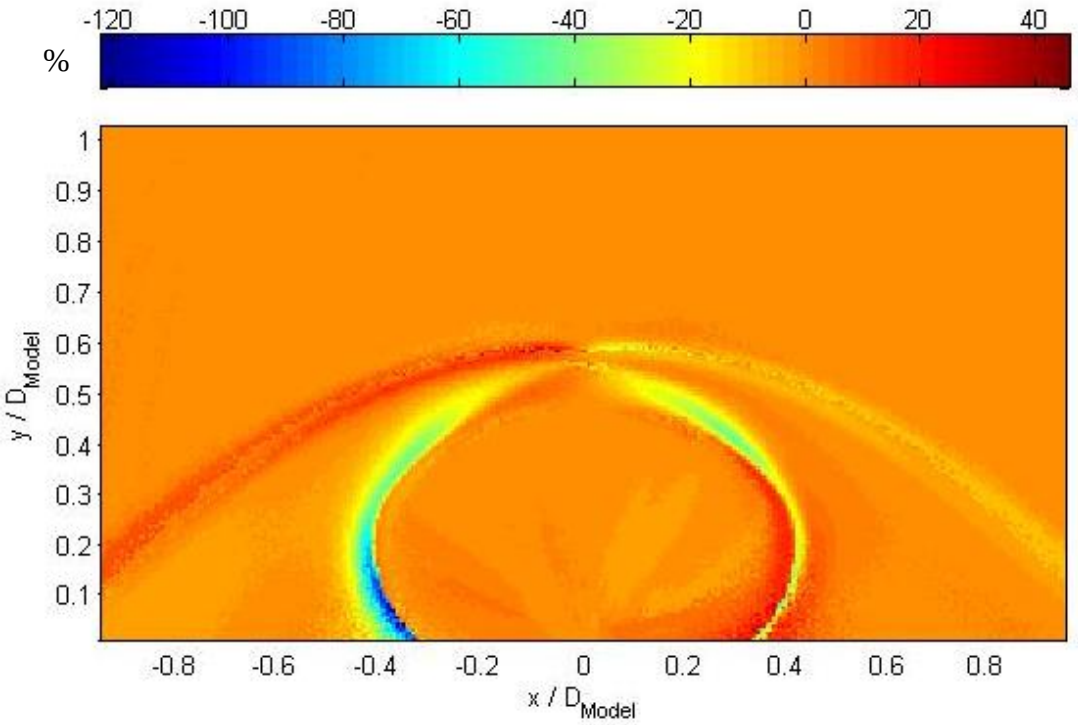

Figure 5.7: Percent difference in velocity magnitude due to impact shift

Although the magnitude of velocity is obviously affected by impact shift, the effect is relatively minor throughout the majority of the flowfield. Throughout the PD jet core, freestream, and areas between the PD jet core and bow shock, neglecting impact shift results in less than a 5% difference in velocity magnitude. Impact shift is proportional to pressure, and inversely proportional to $T^{0.7}$, thus it is negligible in the freestream where the flow is rarefied at high Mach numbers and where pressure is extremely low. Furthermore, the PD jet core is not largely affected by impact shift because the total pressure of the PD jet plenum is relatively low at 40 kPa. Regions between the PD jet shear layer and bow shock are not greatly affected because the pressures in this region will be relatively low due to the rarefied conditions, while the temperature is relatively high. Impact shift has the most notable effect in the PD jet shear layer, with imbedded oblique shock, freestream bowshock, and in the subsonic velocity region between the PD jet Mach disk and bow shock. In the PD jet shear layer, with imbedded oblique

shock, and bow shock, pressure increases as the fluid is compressed. Thus it is possible for a very small area of the flow to have relatively high pressure and moderately low temperature, and subsequently a large impact shift. In the subsonic region between the bow shock and the PD jet terminal shock the fluid has gone through two normal shocks (a normal shock from the freestream, and terminal shock at the Mach disk), so it is expected for pressures in this area to also be relatively higher than in many other parts of the flow. Also, the measured velocities in this region are very low, so even small effects due to impact shift will cause a relatively large effect in terms of total velocity magnitude.

5.2 Single-Sonic PD Temperature

For the single-sonic PD jet model the temperature was calculated three different ways: 1) the direct output from a non-linear least squares fit to the absorption spectrum of the P13/R15 and P48/P103 peaks using equation 2.2 for temperatures below 75K; 2) a T-ratio, with a correction factor, to known temperatures in the range of 50-300K as discussed in Chapter 2.3.2; and 3) by assuming inviscid conservation of energy to compute the temperature from the velocity magnitude. The first two methods used rely on the theory discussed in Chapter 2. The first approach provides good results in rarefied sections of the flowfield where temperature is low; however, unexpected behavior was measured by the second approach in the high-temperature region between the PD jet core and freestream bow shock. Because viscous effects, as discussed in Chapter 5.1.3, are expected to be low throughout most of the flowfield, the inviscid energy equation is also used to analyze flowfield temperature.

5.2.1 Temperature output from non-linear least squares fit

The least squares fit to equation 2.2, discussed in Chapter 2, is utilized in the following discussion to measure temperature in rarefied portions of the flowfield with temperatures at 50K

and below. The resulting best fit temperature output for the entire flowfield is shown in Figure 5.8. Freestream flows from top to bottom, and the PD jet exit is centered at x/D and y/D of 0. The laser sheet propagates from right to left at an angle of 2.3-deg from the horizontal. Experimental temperature values are in good agreement with computed temperatures in rarefied regions of the flow: the freestream, and in the PD jet core. The freestream flow is accelerating along the centerline, so while the model is set to a location corresponding to Mach 12 flow, the bow shock is pushed upstream when PD jet thrust is initiated. By measuring the physical distance to the bow shock, it is possible to use equation 3.1 to calculate the Mach number at the bow shock, resulting in Mach 11.20 for a single-sonic PD jet at C_T = 1.0. Using isentropic relationships with the measured plenum total temperature of 303 K and Mach 11.20 flow, the pre-shock freestream temperature is calculated to be 11.6 K, while the average measured freestream temperature in this area is 13.0 K.

Equation 3.1 can also be used to compute the Mach number corresponding to each camera pixel along the PD jet core centerline, and thus compute the temperature at each pixel location using isentropic conditions. A comparison of computed temperature, to the experimentally measured temperature is shown in Figure 5.9. Near the PD jet exit, where the temperature is relatively high and fitted temperature is highly dependent on relative peak heights of the P13/R15 and P48/P103 transitions, the measured temperature underpredicts the computed values. However, as the PD jet core becomes more rarefied and the hyperfine structure is resolved, agreement to the theoretical values is quite good. In the region between the bow shock and PD jet terminal shock, where total temperature is expected to be recovered at the stagnation point, the fitting routine relies heavily on the ratio of the P13/R15 peak to the P48/P103 peak, and these temperatures are largely underpredicted from expected values without applying the correction

factor discussed in Chapter 2. Furthermore, the highest temperatures in this area are off-centerline, away from the free stagnation point. This unexpected behavior will be discussed in-depth in the next section. In areas where the signal level is relatively low (can be seen in the region of x/D of ± 0.30, and y/D of 0.05 to approximately 0.10), noise in the data more heavily influences the fitting routine, causing some erratic reported temperatures as seen in Figure 5.8. In this region, the fitting routine did better at negative x/D because the P48/P103 peak was Doppler shifted towards the center of the argon-ion laser gain profile, whereas it was shifted out of the gain profile for positive x/D.

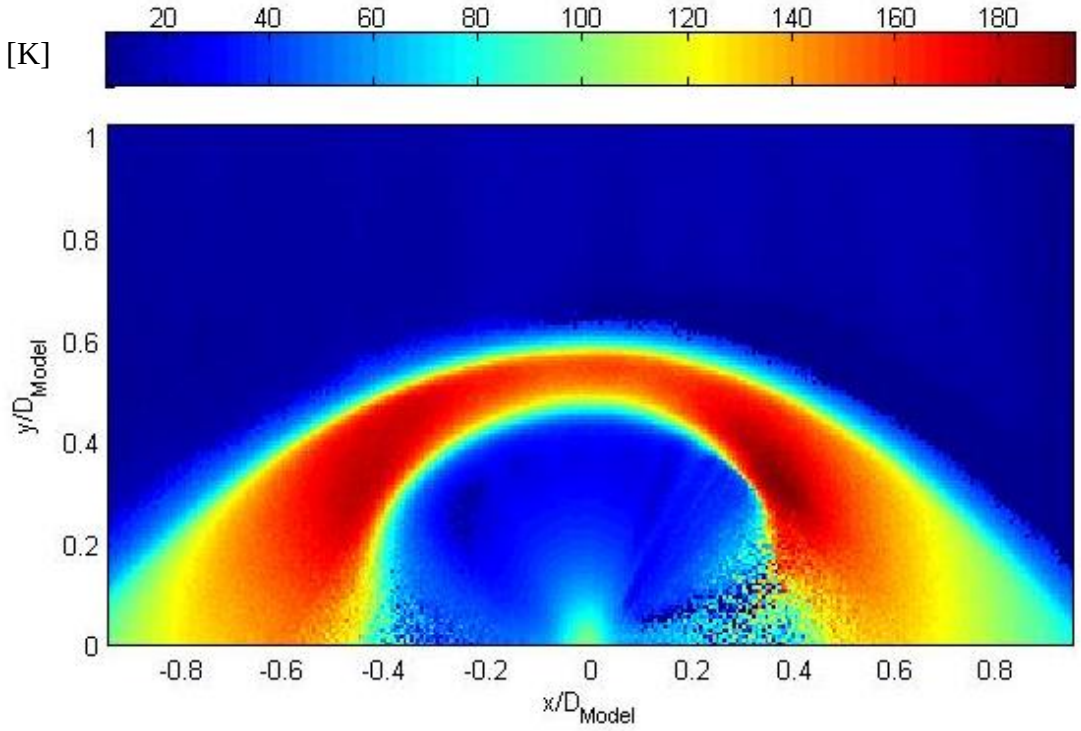

Figure 5.8: Best fit temperature from least squares fitting of equation 2.2 to measured iodine absorption transitions, single-sonic PD model C_T = 1.0, M_∞ = 12.0, M_{Jet} = 1.0

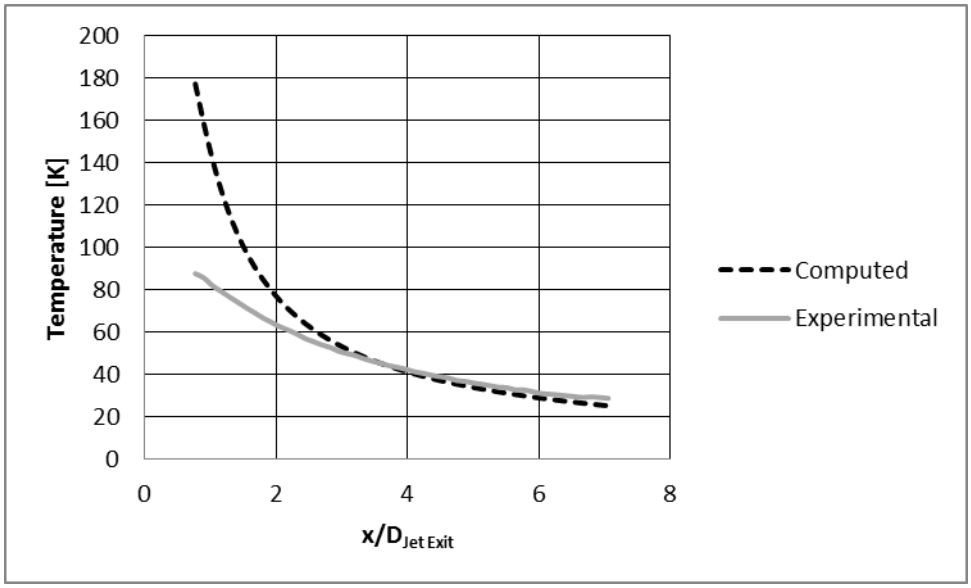

Figure 5.9: Comparison of experimental best-fit temperature in Equation 2.2 to computed temperature along the PD jet centerline, using Eqn. 3.1

5.2.2 Temperature Ratio and Correction Factor

Recall from Chapter 2, temperatures from the range of approximately 50-300 K are measured by comparing the ratio of the P48/P103 to P13/R15 peak amplitude, which is temperature-sensitive due to the large difference in rotational quantum numbers. The experimental T-ratio is measured by fitting a Gaussian profile to the measured P48/P103 and P13/R15 absorption spectra, then taking the ratio of fitted peak amplitudes. Due to the low jet exit pressure, and highly rarefied freestream conditions, pressure is low in the majority of the flowfield, thus the absorption transition profile broadening can be assumed to be due to thermal, Gaussian, broadening. This method was chosen to measure the relative peak heights to reduce uncertainty which would be induced by simply taking the maximum of the fitted iodine model, or measured spectra, where random variations from noise can artificially affect the relative peak height.

Once the T-ratio is measured, a correction factor was found to be necessary to relate the relative peaks heights to a physical temperature (as discussed in Chapter 2.3.2). To calculate the correction factor, computed temperatures using Eqn. 3.1 at known points in the PD jet core,

along the PD jet centerline, are plotted versus the measured T-ratio, and a linear fit is computed, as shown in Figure 5.10. The fitted correction factor corresponds to the following relation:

$$T_{Corrected} = 354.4T_{ratio} - 1.9 \quad (5.2)$$

where $T_{Corrected}$ is the corrected temperature, T_{Ratio} is the experimentally measured T-ratio, and the constants are the numerical correction factor. In Figure 5.10 the single data point at 303K is the measured T-ratio in the static cell at known temperature, and the lower-temperature points are measured T-ratios at known distance from the PD jet exit along the PD jet core centerline. The Mach number at each point is calculated using Equation 3.1, and temperature is computed at each discrete location using isentropic relationships. The resulting rotational temperature measurement is shown in Figure 5.11 for one half of the flowfield, negative x/D. For positive x/D the P48/P103 peak Doppler shifted outside of the argon-ion gain profile, so a temperature measurement from the T-ratio was not possible. The laser sheet angle is 2.3-deg from the horizontal, and propagates from right to left. Because the temperature is so low in the freestream, the P48/P103 rotational quantum levels are de-populated, and thus no T-ratio can be measured. The total temperature at the stagnation point is measured as 242 K with this method, which is lower than expected by approximately 60 K. Furthermore, temperature is approximately 293 K outside the PD jet shear layer. Due to the difference in the area between the PD jet terminal shock and freestream bow shock, and regions of higher T seen in the region outside the PD jet shear layer, as well as viscosity likely being insignificant for the majority of the flowfield (shown in 5.1.3, and further discussed in a subsequent section), it was decided to use the inviscid energy equation to compute flowfield temperature for all subsequent experimental measurements.

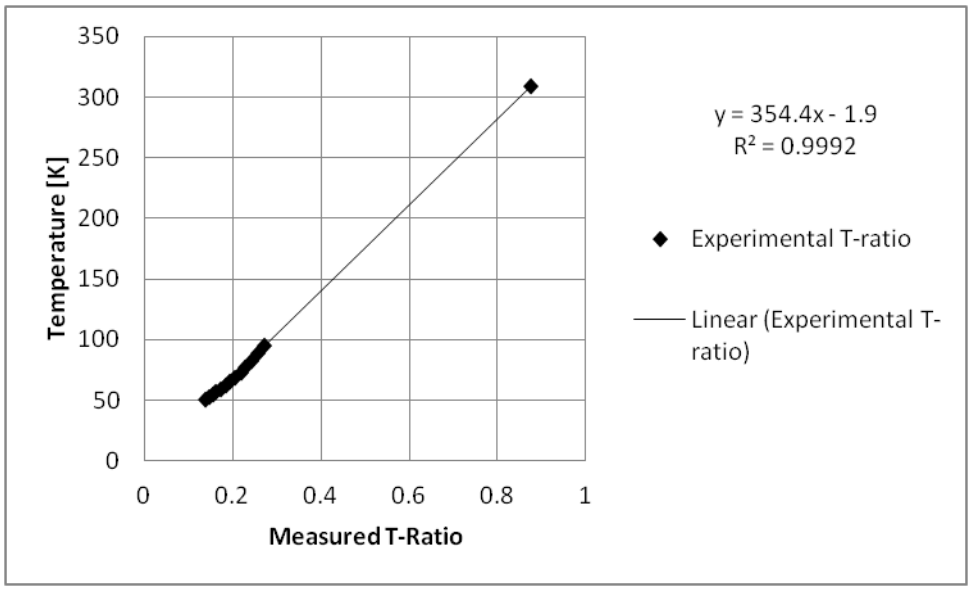

Figure 5.10: T-ratio correction factor

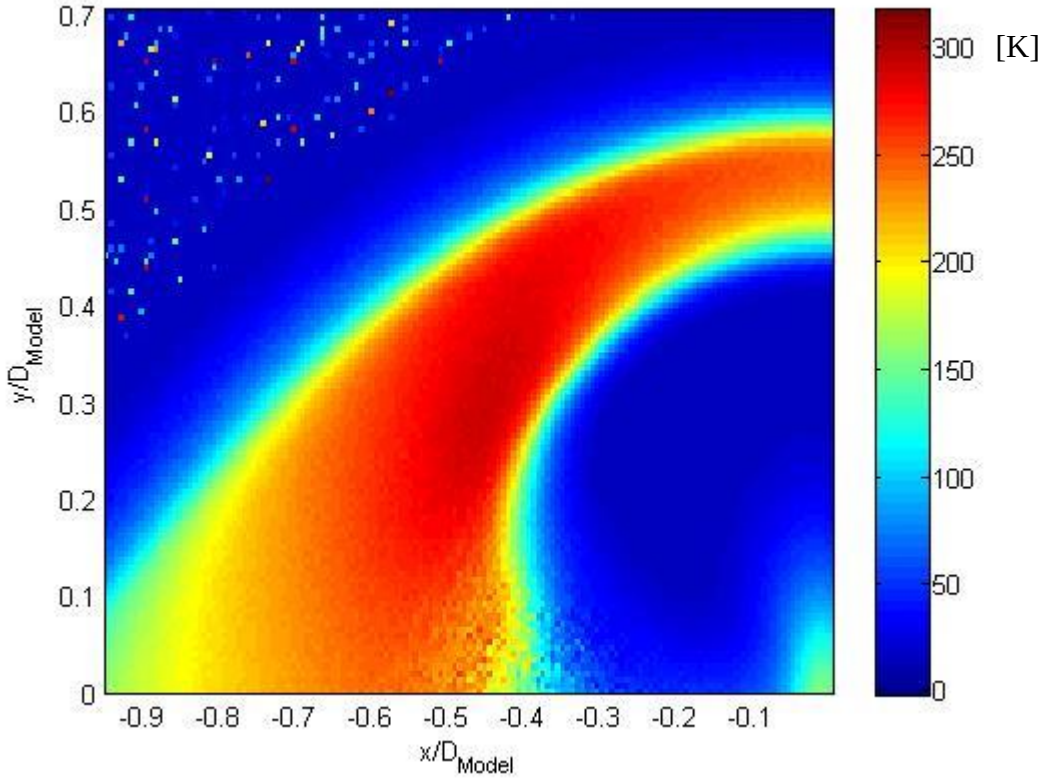

Figure 5.11: Temperature measured from T-ratio with applied correction factor, C_T = 1.0, M_{jet} = 1.00, M_∞ = 12.0

5.2.3 Inviscid Temperature Calculation

Due to difficulty with a two-line ratio approach for accurate temperature measurement, and in the approach to fit the absorption spectrum above 75K, a temperature is computed using the inviscid energy equation and measured velocity magnitude. Viscous effects are expected to be small throughout the majority of the flowfield, so the Euler equation for conservation of energy, equation 5.1, can be used to calculate translational temperature from the measured 2D velocity magnitude:

$$T = \frac{1}{c_p}\left[c_p T_0 - \frac{1}{2}|V|^2 \right] \tag{5.3}$$

The first term on the right hand side of equation 5.1 accounts for internal energy, and the second is due to the kinetic energy of the flow. T is the temperature, c_p the specific heat at constant pressure for nitrogen, T_0 is the total temperature in the plenum, and |V| the velocity magnitude. The specific heat for nitrogen is used because the seeding fraction of iodine is so low, 1 part in 5,000, thus making it not necessary to account for a mixture and the c_p of nitrogen can be used. The translational temperature, calculated from equation 5.1, is shown in Figure 5.12. The temperature result using the inviscid energy equation qualitatively agrees well with the expected temperature distribution, with the temperature quickly decreasing in the PD jet core, rising as molecules pass through the PD jet terminal shock, and having nearly total temperature recovery at the free stagnation point, with a computed temperature of 302.2 K. Quantitatively, the temperature calculation also agrees well with theoretical freestream temperature of 11.6 K, with mean the inviscid temperature being 13.1 K. The use of this temperature calculation method will be further discussed in the subsequent CFD comparison sections. Note, for some areas of the flow, where viscous effects are anticipated to be relatively large, the temperature solution using

the inviscid energy equation only offers qualitative results. Only this temperature calculation will be presented and discussed for the single- and quad-supersonic PD models in later chapters.

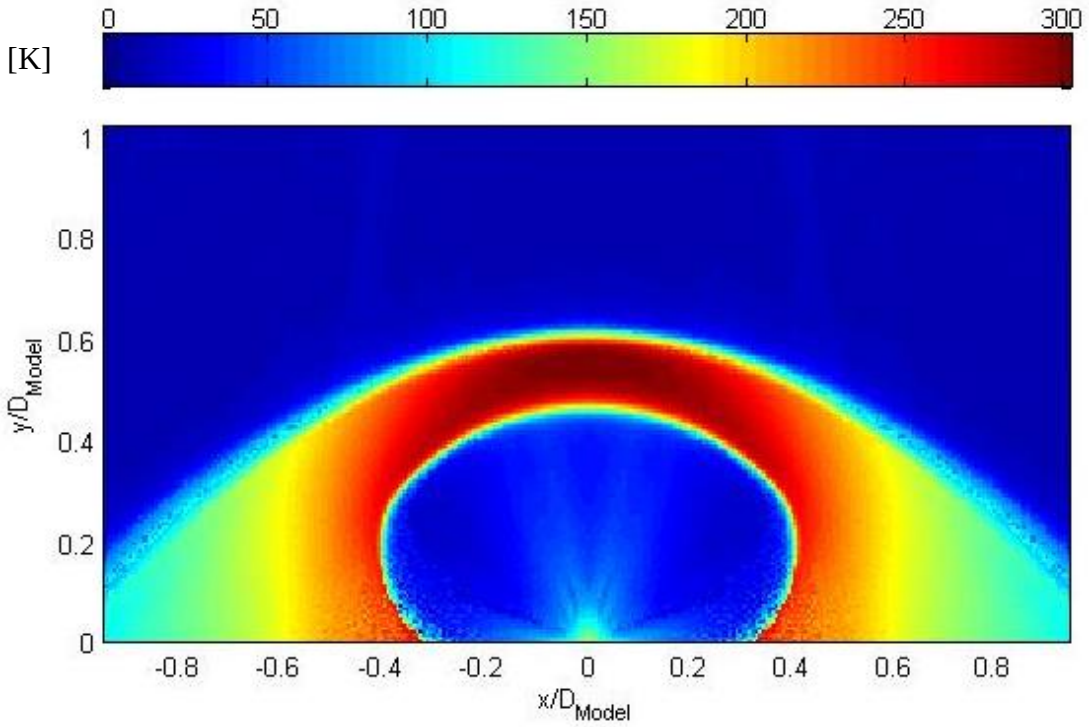

Figure 5.12: Single-sonic PD model temperature calculation from inviscid energy equation C_T = 1.0, M_{jet} = 1.00, M_∞ = 12.0

5.3 Comparison to CFD

Experimental velocity and temperature calculated from the inviscid energy equation will be compared with numerical simulations executed using LeMANS, a parallelized CFD code for simulating hypersonic reacting flows, and described in Chapter 4.

5.3.1 Velocity

Experimental velocity magnitude and streamline results are compared with LeMANS CFD solutions in Figure 5.13. In figure 5.13 the freestream flows from left to right and the jet exit nozzle is located at x/D and y/D of 0. The CFD results are shown for positive y/D values, and the experimental results are negative y/D, where D corresponds to the model diameter of 10 mm.

Overall, there is good agreement between the experimental and computational results. Slight discrepancies are notable with the shock stand-off distance (point where the bow shock begins), bow shock thickness, PD jet plume size, and recirculation region near the bottom of the PD jet plume. The CFD computations indicate a larger shock stand-off distance and subsonic region for the single-sonic PD model, while the experimental results show a longer PD jet plume structure and a thicker bow shock. Discrepancy between the experiment and CFD in the bow shock thickness could be due to non-continuum effects in this area, which will not be well predicted by CFD. There is a low-speed recirculation region seen in the numerical calculation which is not present in the experimental results. As noted in reference 56, the largest recirculation regions are expected for the lower C_T. As C_T increases, and thus jet plume size, the small eddy recirculation region is pushed farther towards the model shoulder until finally not being evident around C_T of 2.0. The larger jet plume size seen in experimental results would then suggest a smaller eddy recirculation region and explain why it may not be visible for the sonic experimental results.

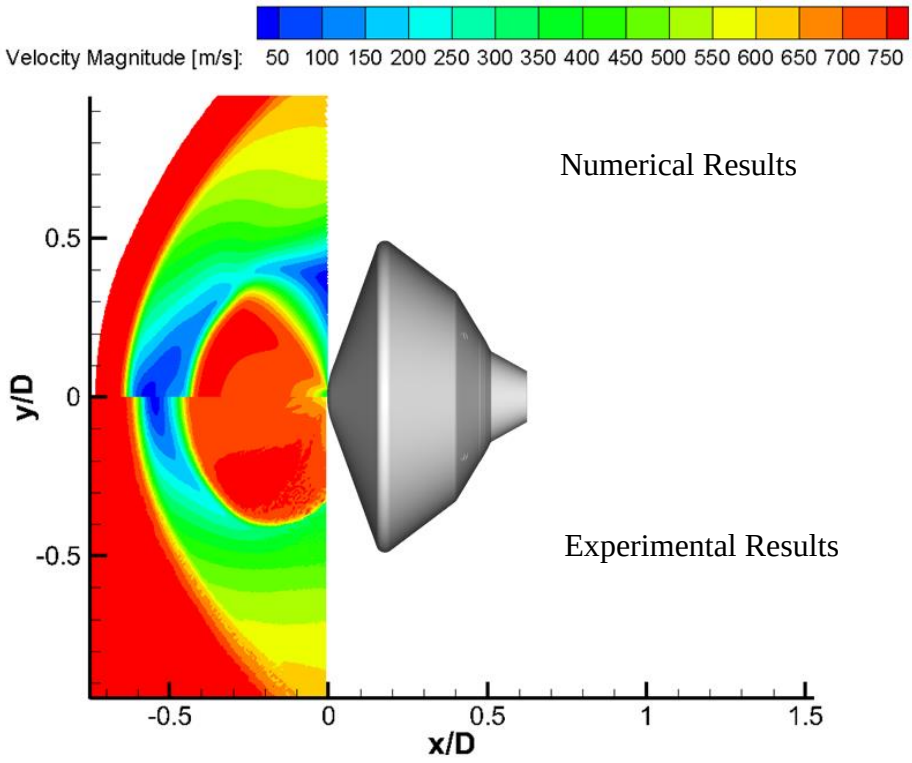

(a) Velocity magnitude

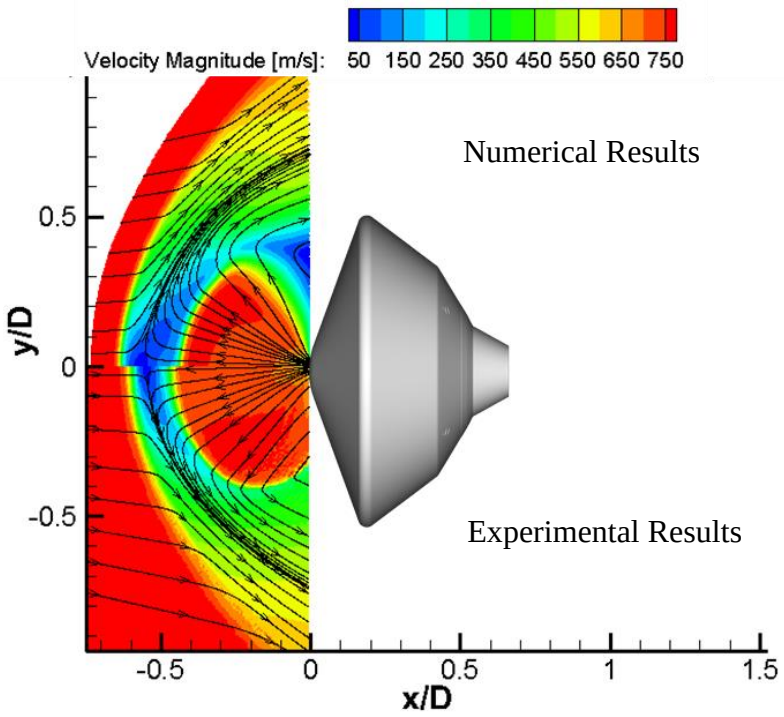

(b) Velocity magnitude and streamlines

Figure 5.13: Comparison of CFD (top) velocity magnitude and streamlines to experimental (bottom), C_T = 1.0, M_∞ = 12.0, M_{Jet} = 1.0

Line comparisons of the experimental and computational results are shown in Figure 5.14, and in the coordinate system shown in Figure 5.13. Four comparisons are made, a centerline comparison at constant x/D through the center of the jet core in Figure 5.14(a), and 3 cross-sectional cut comparisons in Figure 5.14(b) – (d). The centerline comparison in Figure 5.14(a) shows the velocity magnitude for the CFD and experimental results at constant y/D = 0, and tracking upstream to x/D of -0.70. Velocity magnitude along the centerline agrees very well in the PD jet core, with the exception of near the PD jet exit, where the experimental results are higher at the jet exit, but quickly agree by -0.05 y/D upstream. The location of the free stagnation point is experimentally measured to occur at -0.54 y/D, while the CFD results indicate a value of -0.63 y/D.

Figure 5.14(b)-(d) are 3 cross-sectional cuts at constant x/D of 0.1, 0.2, and 0.3, and tracking from y/D of 0 to 0.5 for the CFD results, and 0 to -0.5 for the experimental results. The experimental results are plotted versus positive y/D for a direct comparison of velocity at each given y/D location. The cross-sectional comparison in Figure 5.14(b) shows a sharp decrease in velocity magnitude across the jet boundary, whereas the decrease is more gradual for the CFD results. For all cross-sectional cuts, it is seen that the boundary occurs further radially outward for the experimental results than for the computations. Furthermore, the minimum velocity magnitude is larger for the experimental results, but the computations match very well after the minimal velocity location, most notably in Figure 5.14(c) and (d). Overall, there is good agreement between the experimental and computational results.

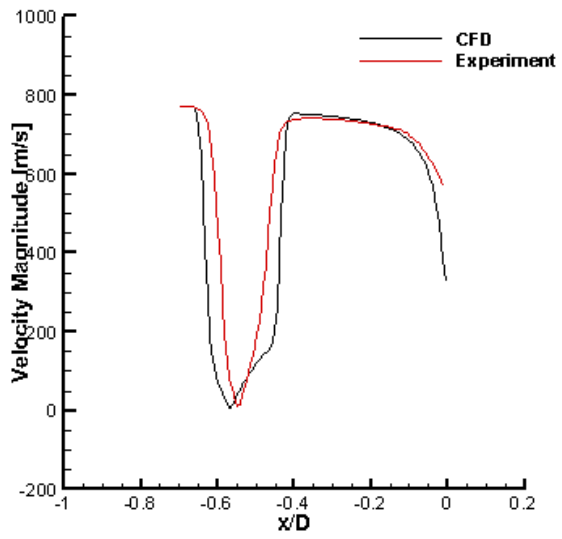

(a) Centerline comparison at y/D = 0

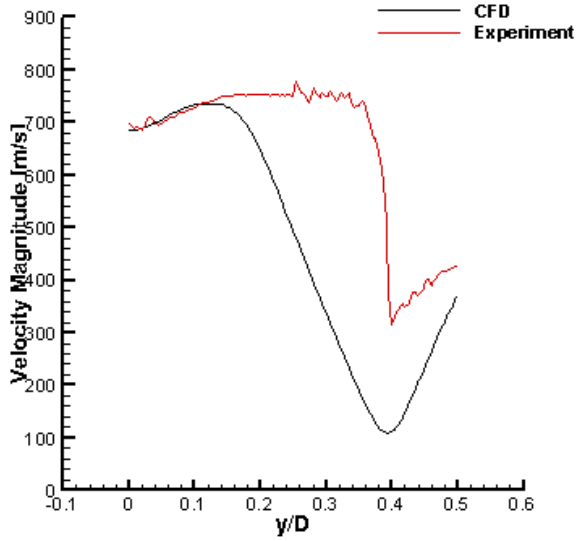

(b) Cross-sectional cut at x/D = 0.1

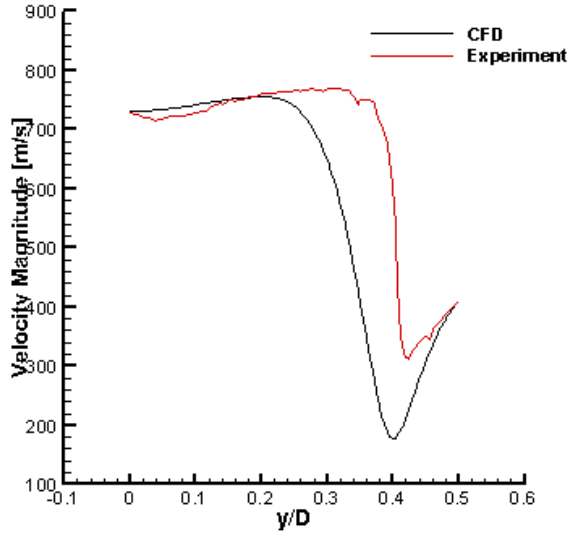

(c) Cross-sectional cut at x/D = 0.2

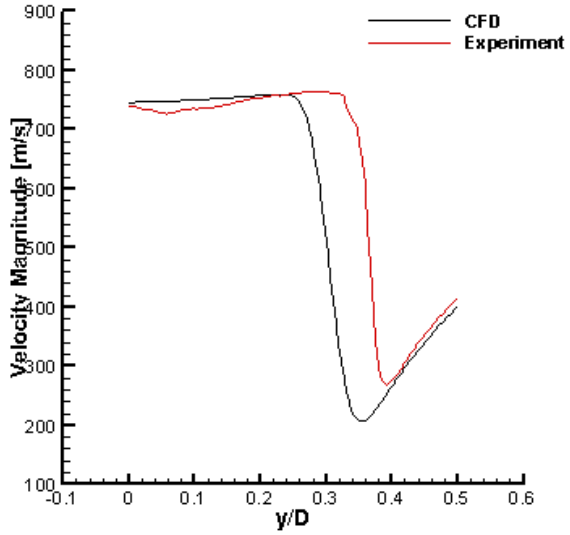

(d) Cross-sectional cut at x/D = 0.3

Figure 5.14: Centerline and cross-sectional cuts through PD jet core comparisons between CFD and experimental results. Coordinate system shown in Figure 5.13

5.3.2 Temperature

The LeMANS computations use the full Navier-Stokes equation to solve for flowfield temperature, including viscous effects. In order to quantify where temperature computed from

the inviscid energy equation will be reliable, temperatures computed with two approaches are compared and shown in Figure 5.15. Freestream flows from left to right, and the PD jet exit is centered at x/D and y/D of zero. Temperature computed from the inviscid energy equation and using the CFD velocity magnitude is shown for positive y/D and labeled in the figure. Temperature computed from the full-Navier Stokes equation with viscous effects is shown for negative y/D. As expected from the computed strain tensor, viscous effects are negligible for the majority of the flowfield. Qualitatively the temperature fields agree quite well. To understand the difference quantitatively, the percent difference between the two computed temperatures, together with computed streamlines, is shown in Figure 5.16. For the majority of the flowfield the difference is between ± 5%. Areas where the differences are the largest are in the PD jet terminal shock, where the PD jet fluid abruptly turns downstream at the PD jet boundary, and in the region between 0.40 and 0.50 y/D, which is where the largest components of the strain tensor were measured in the previous section. A -20% difference is noted in the freestream flow pre-shock; however, the temperatures in this area are very small, on the order of 13 K, so a small variation in temperature results in a large percent difference. Overall, viscous effects are minor throughout the flowfield, so experimental temperature computed with the inviscid energy equation is considered to be quantitative in the majority of the flowfield.

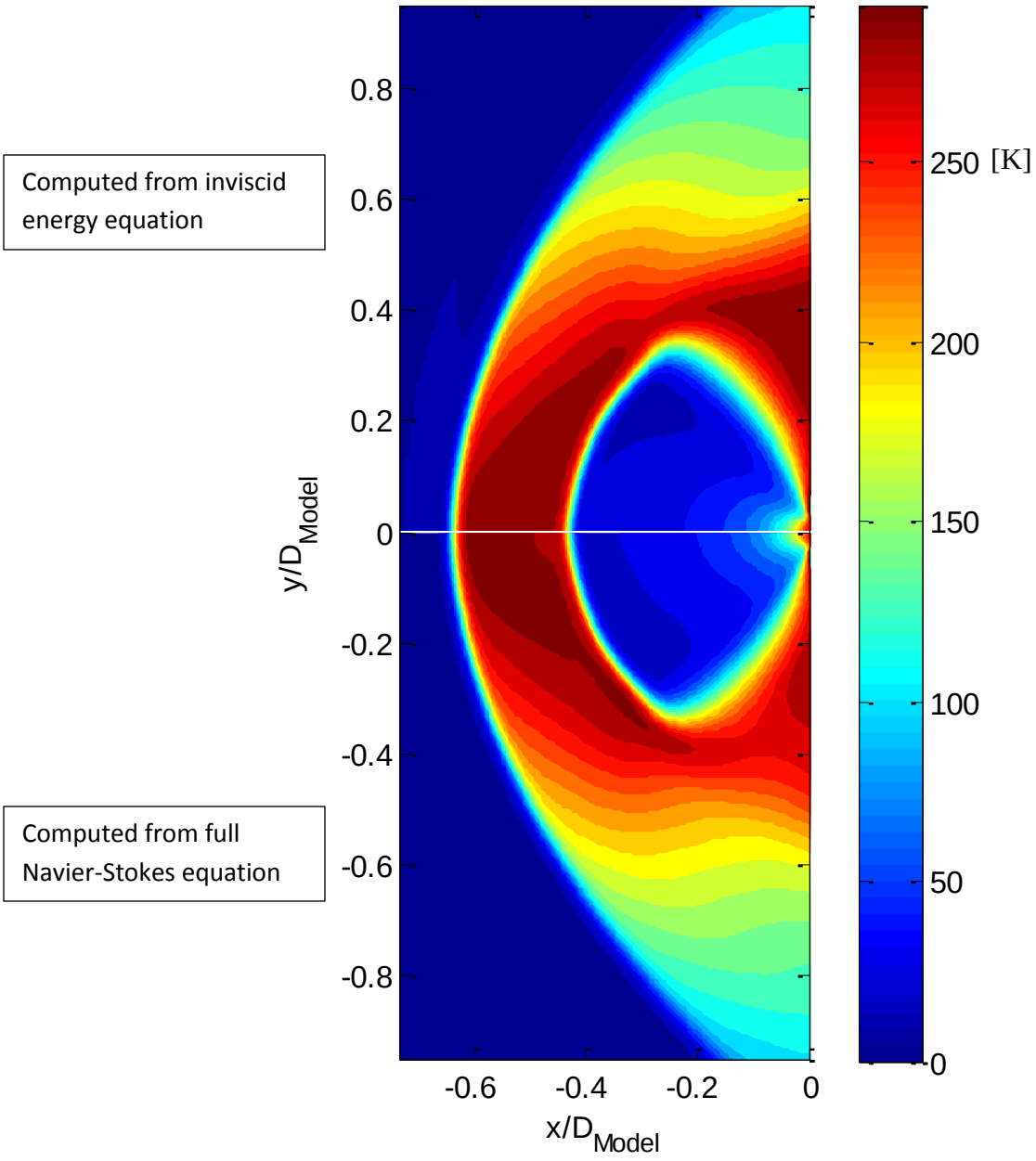

Figure 5.15: Comparison of computed temperature from full Navier-Stokes equations versus temperature computed from inviscid energy equation

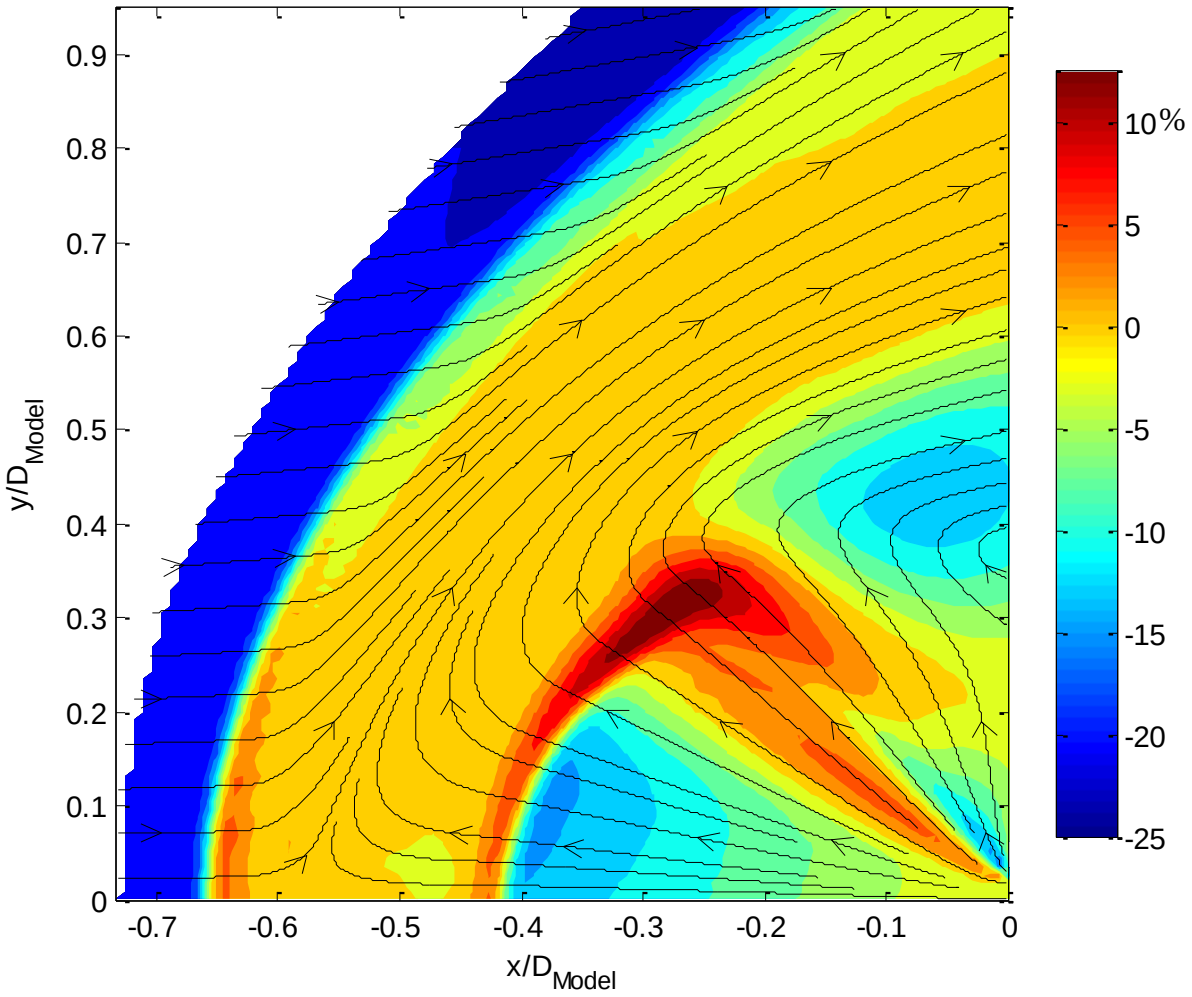

Figure 5.16: Percent difference of temperatures computed from full Navier-Stokes equations versus temperatures computed with inviscid energy equation

Computed temperature from the inviscid energy equation for the experimental and CFD results are shown in Figure 5.17 for the single-sonic PD mode in Mach 12 freestream flow with C_T of 1.0. Freestream flows from left to right, and the PD jet exit is at x/D and y/D of zero. CFD results are reported for positive y/D and experimental results for negative y/D. Overall, there is good qualitative agreement in absolute temperature comparisons. As expected from the velocity comparisons, there are discrepancies in certain structures, such as the PD jet width, penetration, subsonic region, and recirculation region. The experimental PD jet penetrates farther upstream

than the computational results, while the bow shock occurs farther downstream; this results in a smaller subsonic region than in the CFD results.

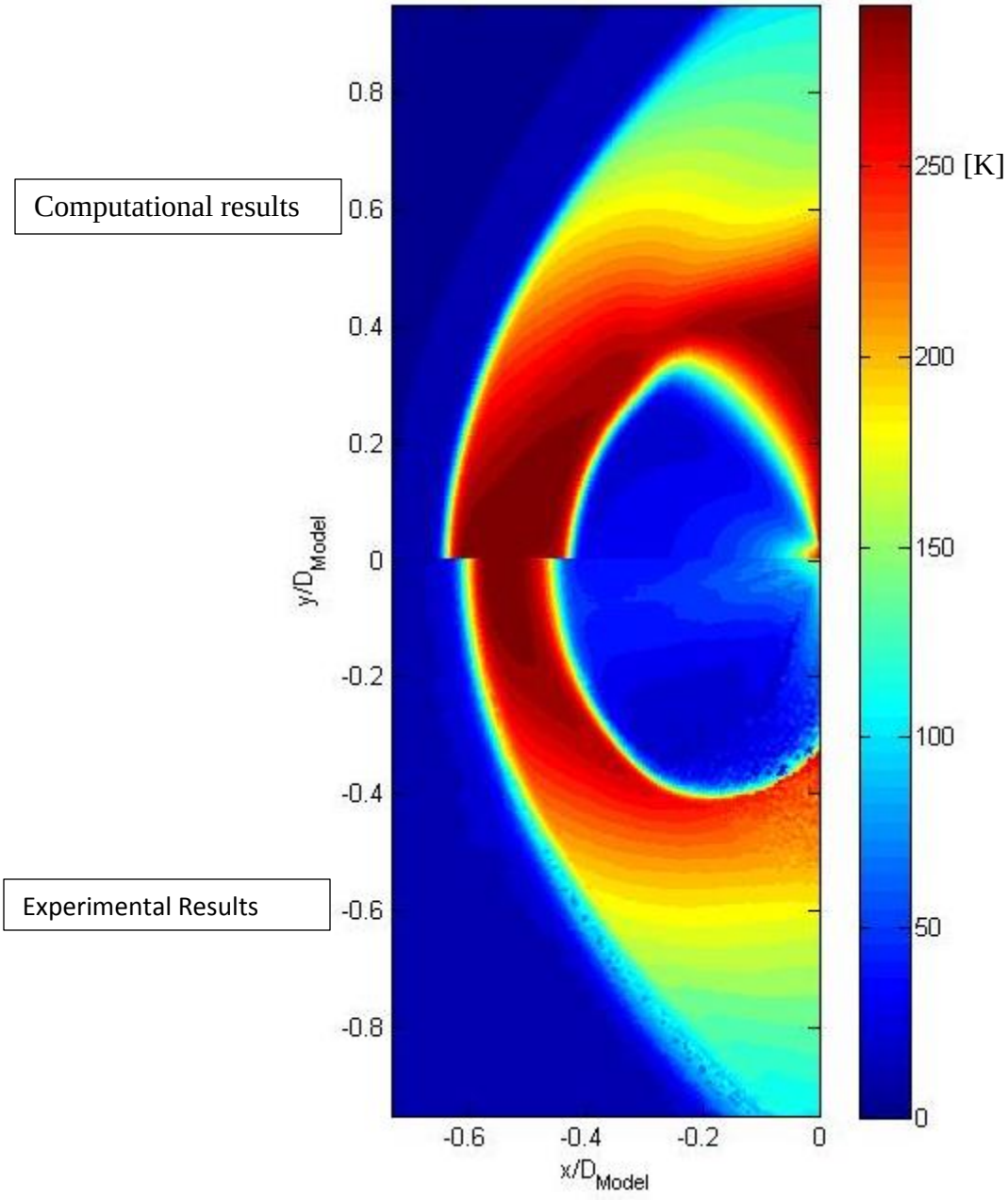

Figure 5.17: CFD temperature versus experimental temperature, computed from inviscid energy equation, $C_T = 1.0$, $M_\infty = 12.0$, $M_{Jet} = 1.0$

CHAPTER 6: QUANTITATIVE SINGLE-SUPERSONIC PD RESULTS

This chapter presents experimental planar velocity and temperature measurements for the single-supersonic PD model with a C_T of 1.0 in Mach 12 freestream flow. The experimental results will be compared with CFD results from the University of Michigan to validate the CFD code.

6.1 Single-Supersonic PD Velocity

6.1.1 Flowfield Symmetry

A Doppler-free visualization of the flowfield was created, as described in Chapter 5, for the single-supersonic PD jet model in Mach 12 freestream flow and with C_T of 1.0. Freestream flows from top to bottom and the origin is centered on the PD jet exit, x/D and y/D of zero. The laser sheet angle propagates from the top right of the image to the bottom left at an angle of 27.4-deg from the horizontal. The bow shock on the left side of the image is blocked from the laser sheet by the model, and thus no fluorescence is captured below y/D of approximately -0.5. It is evident from the Doppler-free visualization that the flowfield is symmetric about the model centerline, and using symmetry to cancel impact shift in the next sections is justified.

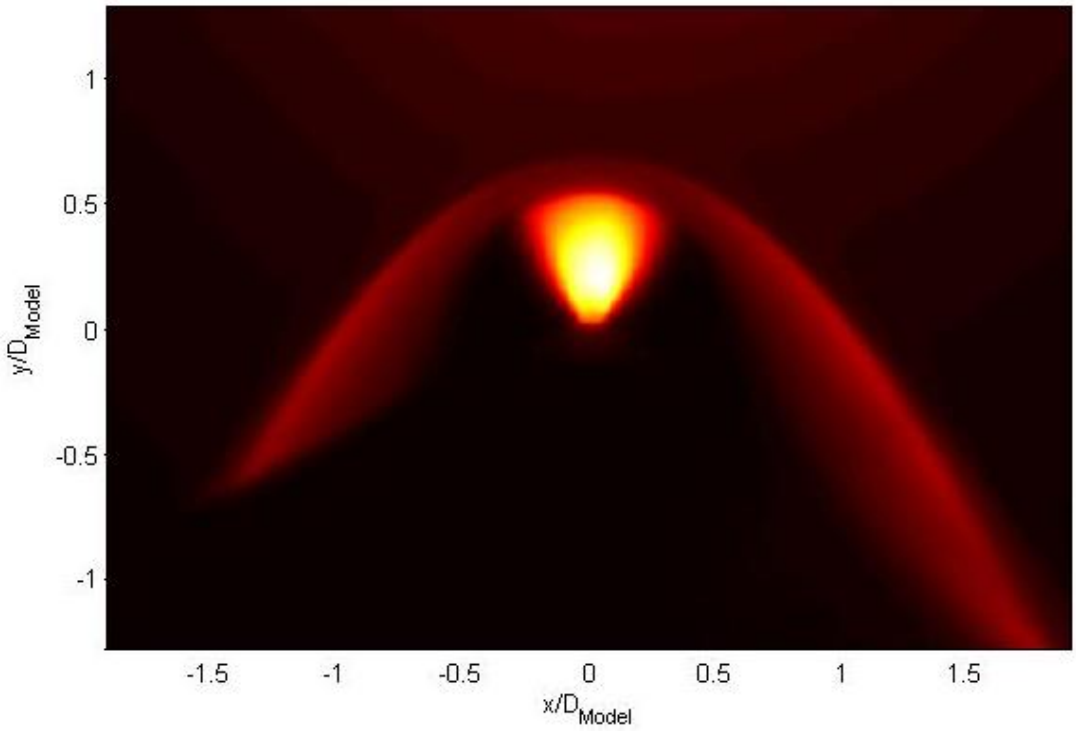

Figure 6.1: Doppler-free visualization of the single-supersonic PD model, C_T = 1.0, M_{jet} = 2.66, M_∞ = 12.0

6.1.2 Flowfield Characteristics

Velocity magnitude and streamlines for the single-supersonic PD jet at a C_T of 1.0 are shown in Figure 6.2 and the 2D velocity vector field at reduced resolution (every seventh pixel) is shown in Figure 6.3. Once again symmetry was used to cancel impact shift. Freestream flow is from top to bottom and the PD jet exit is centered at y/D and x/D of zero, where D corresponds to model diameter of 10 mm. Due to limited optical access, the laser sheet angles were set to 27.4-deg and 2.3-deg from the horizontal.

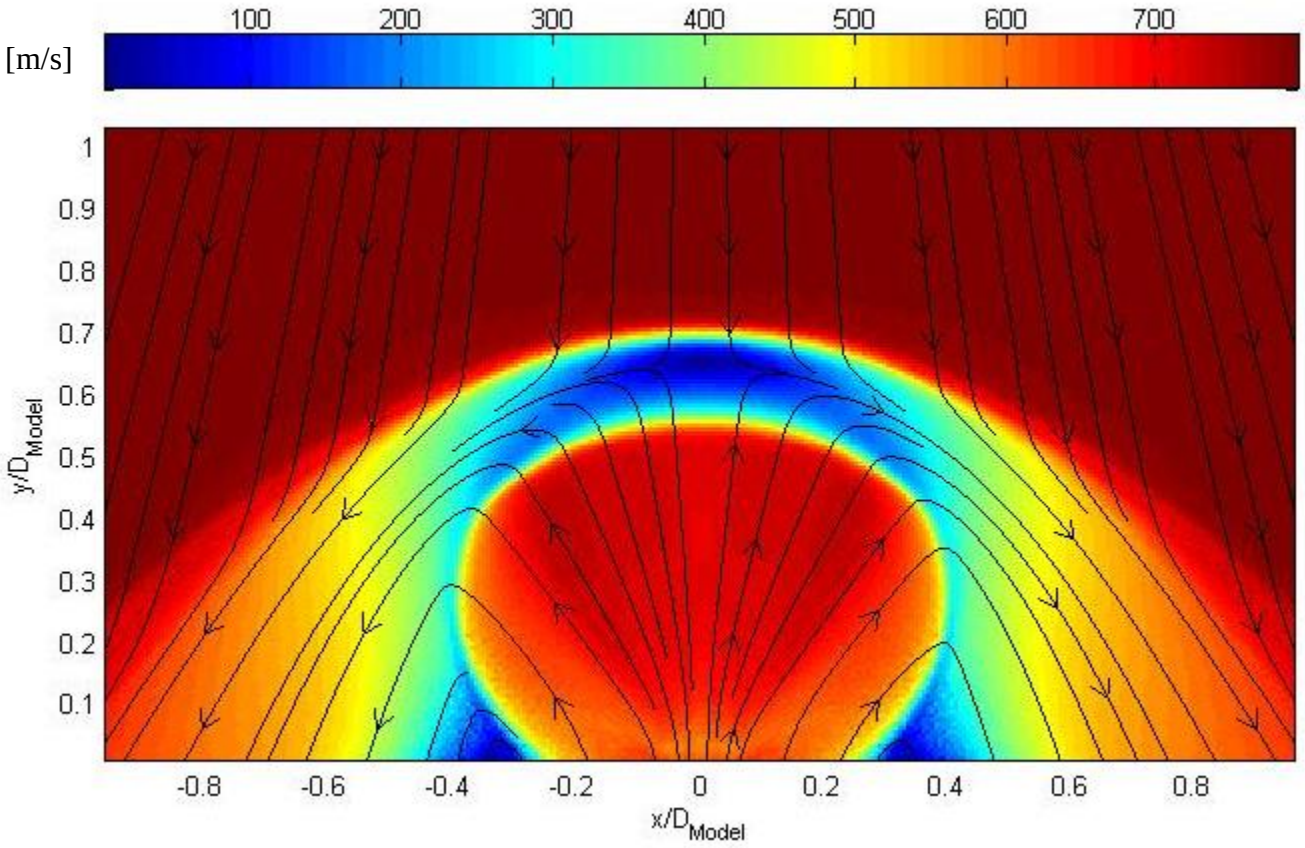

Figure 6.2: Single-supersonic PD jet magnitude and streamlines, C_T = 1.0, M_{jet} = 2.66, M_∞ = 12.0

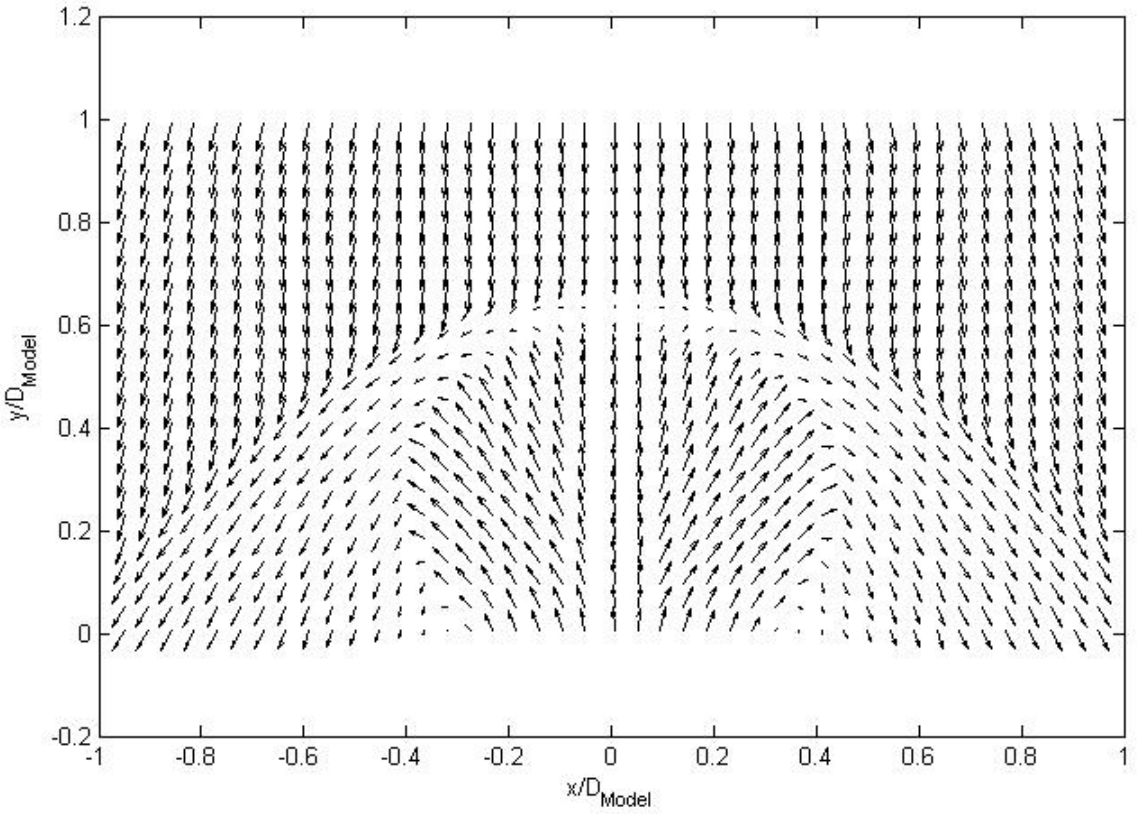

Figure 6.3: Single-supersonic PD jet 2D velocity vectors C_T = 1.0, M_{jet} = 2.66, M_∞ = 12.0

The following discussion presents the flowfield features seen in Figure 6.2 and 6.3, and are labeled in Figure 6.4. In general, the supersonic test case exhibits similar flowfield properties to the sonic test case. The PD jet fluid expands from the Mach 2.66 jet exit until a terminal shock where the fluid slows to subsonic speeds. A freestream bow shock forms upstream of the subsonic region, and a free stagnation point occurs between the PD jet and freestream bow shock. At the free stagnation point an effective contact surface forms between the PD jet and freestream fluids, at which point both turn and flow radially outward around the PD jet structure while turning downstream past the model shoulder. As expected, there are minor differences between the sonic and supersonic jet structure. The supersonic PD jet has a lower jet exit pressure (about 1.2 kPa) and thus a smaller turning angle at the jet exit, which results in an

oblique jet structure at a reduced angle relative to the PD jet core. Furthermore, the supersonic PD jet penetrates farther upstream, to approximately 0.55 y/D. A major difference in the flowfield structures appears near the base of the supersonic jet plume, outside of the PD jet boundary, where a small eddy subsonic recirculation region is evident, which is not present in the sonic model test case.

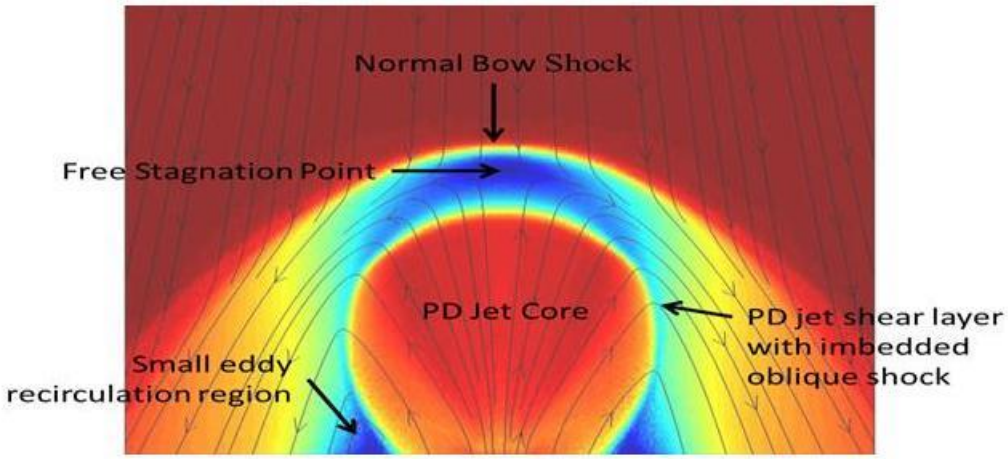

Figure 6.4: Flowfield features overlaid on Figure 6.2

6.1.3 Strain Tensor

The 2D strain tensor is computed using Equation 5.1, and shown in Figure 6.5 for the single-supersonic PD jet model at C_T of 1.0. Freestream flows from top to bottom, the PD jet exit is located at x/D and y/D of 0, and only half of the flowfield is computed due to symmetry. The strain tensor components given by E_{xx} and E_{yy} correspond to expansion and compression in the respective x- and y-directions, positive for expansion, and negative values for compression. Shearing terms are given by E_{xy}, because the strain tensor is symmetric E_{yx} is equal to E_{xy}, and is not shown. As shown in Figure 6.5(a) and (b), there is a rapid expansion in the PD jet core in both the x- and y-directions. The location of the PD jet terminal shock and bow shock are indicated by the strong compression in the y-direction. A relatively large compression occurs in

the x-direction at the PD jet boundary, after which the fluid abruptly turns downstream. This area is also where the greatest shearing strain is measured. Overall, the strain tensor components are relatively small in the majority of the flowfield, but large in very small, distinct areas. This indicates that for the majority of the flowfield, it can be assumed an inviscid approximation for the jet fluid is valid. However, viscous effects are expected to be non-negligible in certain areas of the flow, such as the PD jet terminal shock, freestream bow shock, and the point of intersection as indicated in Figure 6.4. It is also possible to calculate flow vorticity, given by Equation 5.2. Vorticity for the single-supersonic PD test case is shown in Figure 6.5(d). The greatest vortices are located in the shearing region on the PD jet boundary, where the off-axis PD jet fluid is flowing upstream at the boundary and intersects the freestream/PD jet fluid flowing downstream from the low-velocity region, and suddenly turns downstream. Small amounts of vorticity are also measured in the bow shock where the freestream fluid makes an abrupt turn as it flows around the model and proceeds downstream.

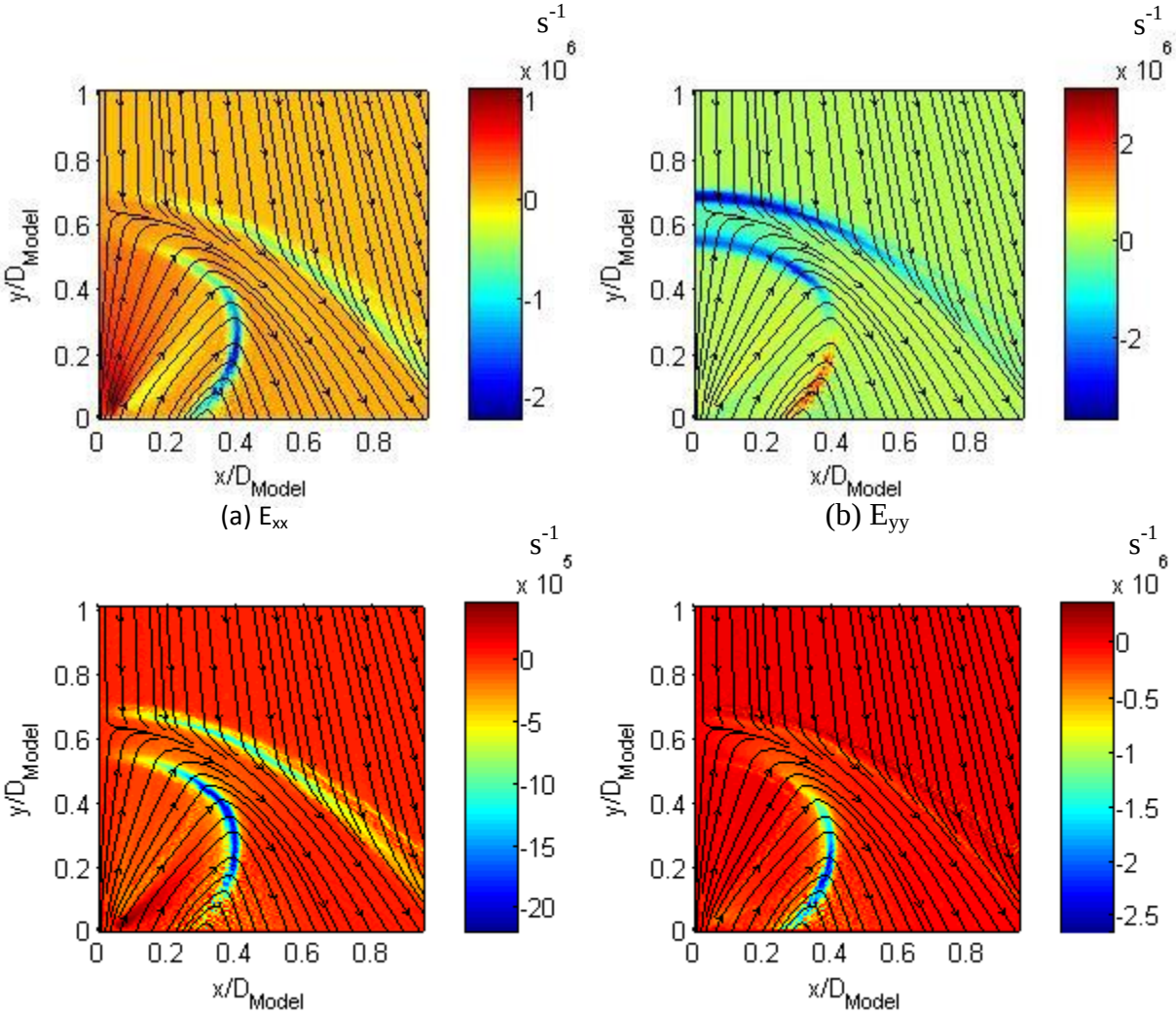

Figure 6.5: Components of 2D stress tensor for half of the flowfield, C_T = 1.0, M_{jet} = 2.66, M_∞ = 12.0

6.2 Single-supersonic PD Temperature

The inviscid temperature calculation for the single-supersonic PD model at C_T of 1.0 is shown in Figure 6.6. Freestream flows from top to bottom, x/D and y/D of zero corresponds to the jet exit located at the model stagnation point. The PD jet fluid isentropically expands from Mach 2.66 at the jet exit, as the fluid expands the temperature decreases, resulting in the low-temperature PD jet core. The PD jet fluid passes through a terminal shock, increasing in

temperature, and reaches a maximum temperature at the free stagnation point. Freestream fluid compresses in a normal shock upstream of the subsonic region, and has near total temperature recovery at the free stagnation point. In the subsonic region between the PD jet terminal shock and freestream bow shock the temperature remains high, near 300 K. As the subsonic freestream and PD fluid turns radially outward it accelerates around the shoulder of the jet core and temperatures begin to decrease. Temperatures off-axis in the PD jet boundary are slightly higher than in the jet core, due to the fluid temperature increasing through the imbedded oblique shock. At the PD jet boundary, labeled in Figure 6.4, the PD jet fluid quickly decelerates and abruptly turns downstream resulting in a small, high temperature region. Further, the small eddy recirculation region contains fluid at near stagnation conditions and is maintained at high temperature, approximately 302 K.

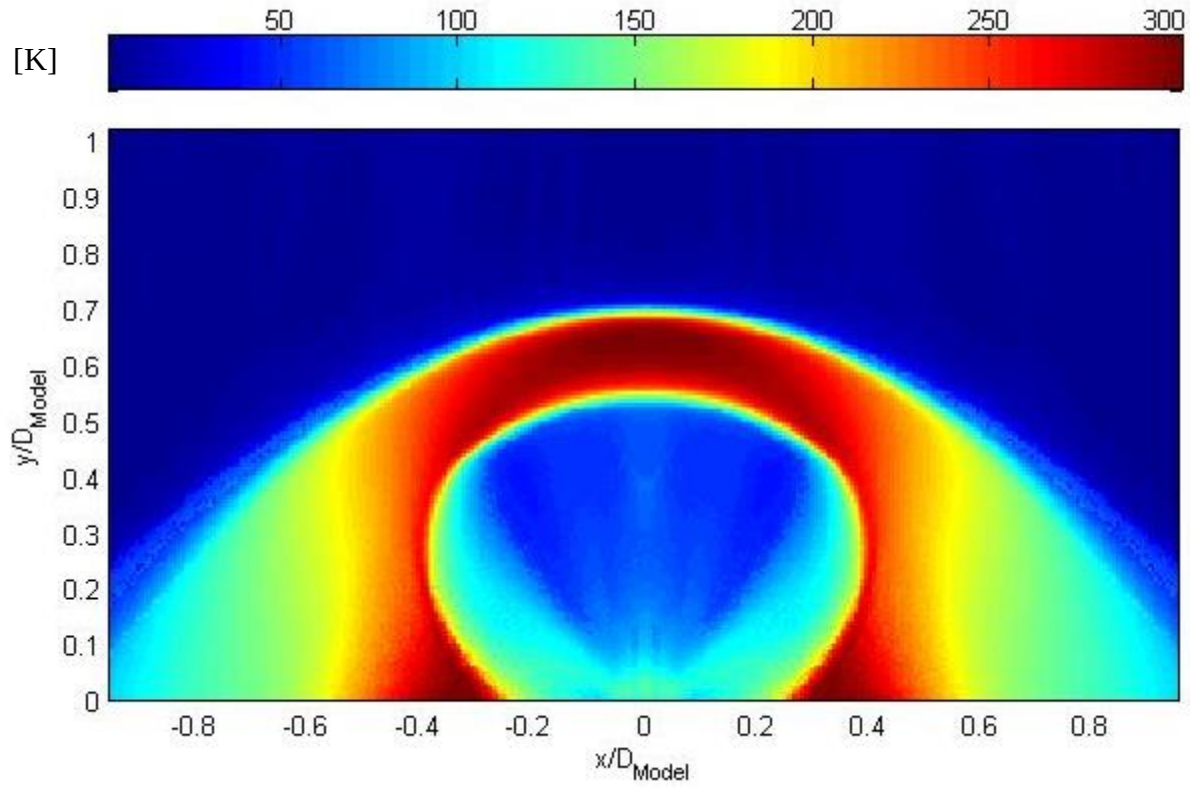

Figure 6.6: Single-supersonic PD model inviscid temperature calculation, C_T = 1.0, M_{jet} = 2.66, M_∞ = 12.0

6.3 Comparisons to CFD

Experimental velocity and temperature will be compared with numerical simulations executed using LeMANS, a parallelized CFD code for simulating hypersonic reacting flows, and described in Chapter 4.

6.3.1 Velocity

Experimental velocity magnitude and streamline results are compared with LeMANS CFD solutions in Figure 6.7. In figure 6.7 the freestream flows from left to right and the jet exit nozzle is located at x/D and y/D of 0. The CFD results are shown for positive y/D values, and the experimental results are negative y/D, where D corresponds to the model diameter of 10 mm. Overall, there is good agreement between the experimental and computational results. Measured velocities in the PD jet core are in excellent agreement, and the streamlines match very well between the experimental results and CFD. Similar to the sonic comparison shown in the previous chapter, discrepancies are notable with the shock stand-off distance (point where the bow shock begins), bow shock thickness, PD jet plume size, and size of the recirculation region near the bottom of the PD jet plume near the model surface. The PD jet does not penetrate as far upstream for the CFD computations, and the bow shock is farther upstream, causing the low-speed region between the PD jet terminal shock and bow shock to be larger in the CFD results than the experimental results. The experimental PD jet boundary is wider than the CFD case and the experimental recirculation region is smaller. This confirms the trend discussed in Ref. 56: as the PD jet boundary increases in size, the recirculation region is pushed radially out towards the model shoulder, and decreases in overall size. For the single-supersonic PD model, the PD jet is larger in the experimental results than in the CFD results, causing the experimental recirculation region to be smaller. In the previous chapter, the recirculation region was not evident in the

measurement because the sonic PD jet has a greater pressure at the jet exit and thus expands more in the radial direction. This causes the PD jet boundary to be larger, resulting in no recirculation region being captured in the field of view for the experimental results.

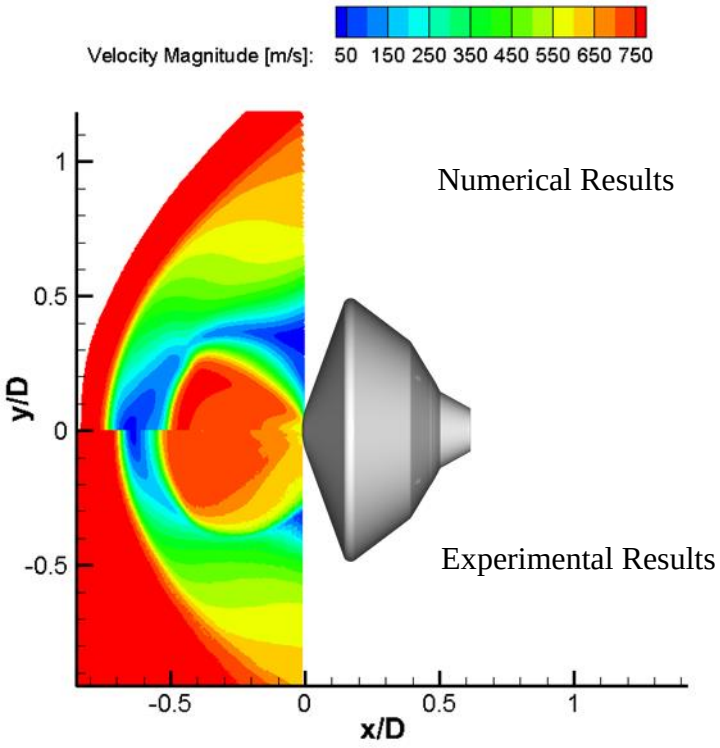

(a) Velocity magnitude

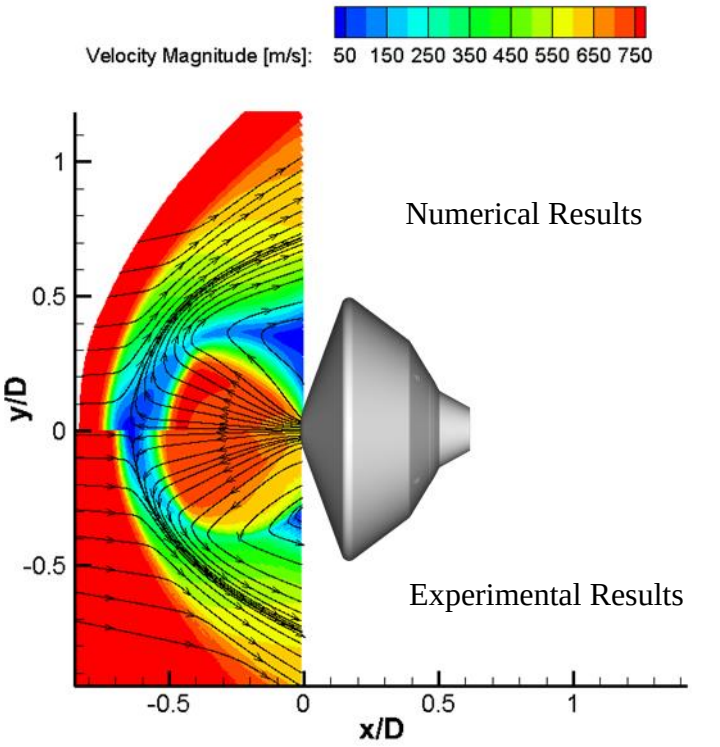

(b) Velocity magnitude and streamlines

Figure 6.7: Comparison of CFD (top) velocity magnitude and streamlines to experimental (bottom), C_T = 1.0, M_∞ = 12.0, M_{Jet} = 2.66

Velocity magnitudes are compared along the centerline and in three cross-sectional cuts through the PD jet core for the experimental and computational results in Figure 6.8, and in the coordinate system shown in Figure 6.7. The centerline comparison is at constant y/D of 0, and velocity magnitude results are plotted from x/D of 0 to -0.8. The experimental and computational results agree quite well at the PD jet exit; however, as the PD jet fluid expands and accelerates, the maximum computational velocity is greater than the experimentally measured velocity. The location of the PD jet terminal shock is evident when the PD jet fluid begins to rapidly decrease, which occurs at x/D of -0.48 and -0.54 for the CFD and experimental results, respectively. Similar to the single-sonic results, discussed in the previous Chapter, the experimental results have a relatively constant slope from the start of the PD jet terminal shock to the free stagnation point (indicated by the minimum velocity at x/D of -0.64), whereas the slope changes at x/D of approximately -0.54 in the CFD results. The experimental and computational results follow the same trend through the freestream bow shock, and have good agreement in the freestream velocity.

The cross-sectional cuts in Figure 6.8(b) – (d) are at constant x/D indicated in each respective caption. Experimental results are plotted versus positive y/D to make a point-to-point comparison with computational results. The cross-sectional cuts begin on the PD jet centerline, and track out through the PD jet core, jet boundary, and into the region between the PD jet and oblique bow shock. Experimental results in the PD jet core have a smaller velocity magnitude, and consistently show the PD jet boundary as being farther radially outward than the computational results. The PD jet boundary is indicated in the Figures by the sharp decrease in velocity magnitude; at this point for the cross-sectional cuts at x/D of 0.2 and 0.3, the CFD results have a constant slope for decreasing velocity, whereas the experimental results have an

inflection point where the slope suddenly changes. It is currently not clear why this discrepancy occurs, but for the cross-sectional cut at x/D of 0.4, the same trend occurs for the experimental and computation results, with a constant slope at the PD jet boundary. In the region between the PD jet boundary and oblique shock, the computational results have a smaller minimum velocity; however, as the velocity begins to increase, the computational and experimental results are in good agreement in velocity magnitude, most notably in Figure 6.8(d). Overall, the experimental and computational results have very similar trends, with the exception of some small discrepancies as noted by the changing slope through the various shock locations.

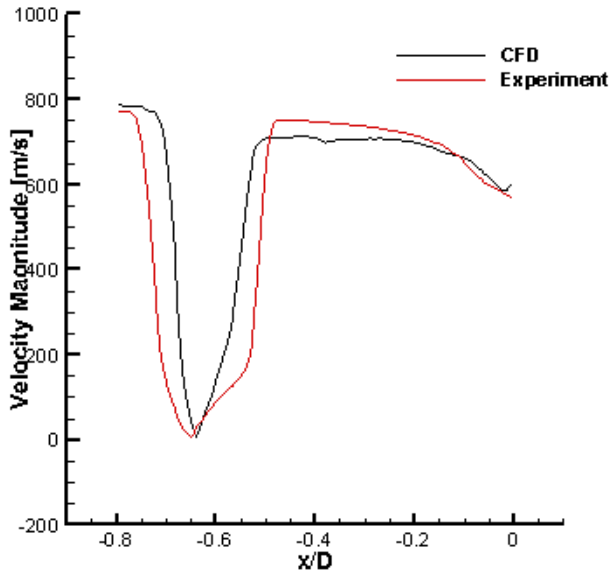

(a) Centerline comparison at y/D = 0

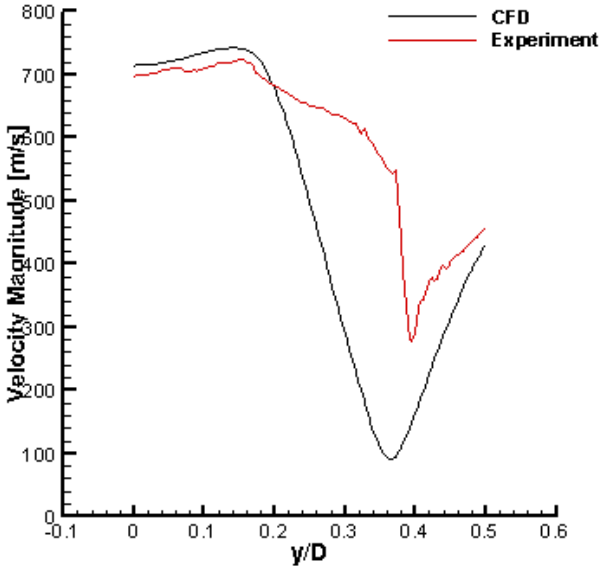

(b) Cross-sectional cut at x/D = 0.2

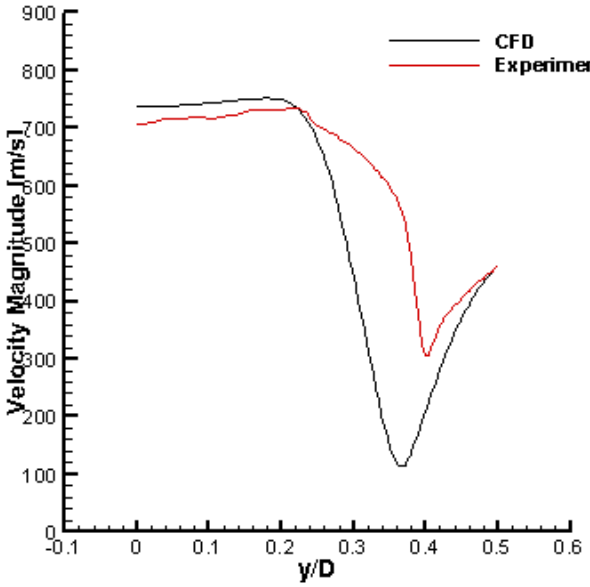

(c) Cross-sectional cut at x/D = 0.3

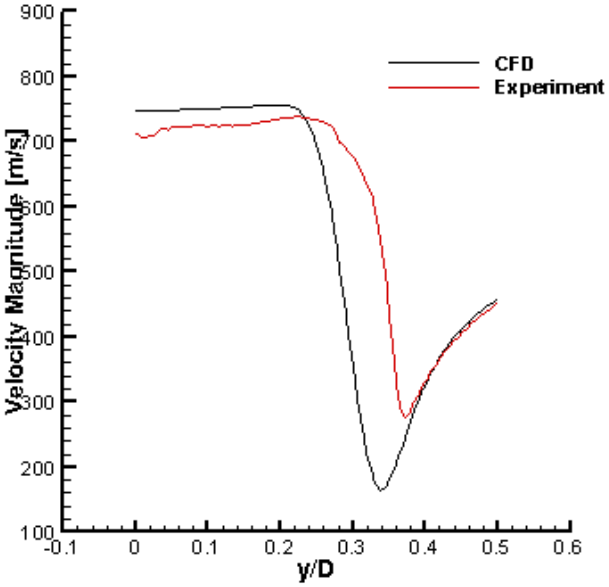

(d) Cross-sectional cut at x/D = 0.4

Figure 6.8: Centerline and cross-sectional cuts through PD jet core comparisons between CFD and experimental results

6.3.2 Temperature

The inviscid energy equation is used to compute flowfield temperature from the measured velocity magnitude; however, it was shown by examining the experimentally measured strain tensor that areas of the flowfield might have significant viscous effects. In addition to the strain tensor calculation, the CFD solution can be used to examine the differences in computed temperature if the flow is considered completely inviscid and the energy equation is used, versus the full Navier-Stokes solution, which considers viscous effects. Temperature computed from the inviscid energy equation, using CFD results for velocity magnitude, and temperature computed from the solution to the full Navier-Stokes solution, with viscocity, is shown in Figure 6.9. Here the inviscid energy equation is used to calculate temperature for positive y/D, and the Navier-Stokes solution is used to calculate temperature for negative y/D. Freestream flows from left to right, and the PD jet exit is centered at x/D and y/D of zero. Overall, the two computed temperatures are in good agreement throughout the majority of the flowfield, indicating viscous effects are largely negligible. To better gauge where viscous effects are significant, the percent difference between the two temperature results, with streamlines overlaid, is shown in Figure 6.10. Assuming an inviscid solution to the energy equation results in a -20% difference in the freestream, where temperatures are on the order of 13 K and small variations in temperature result in large percent difference. A -10% difference is noted near the recirculation region, where temperatures are in the 300K range, and a +10% difference near the oblique shock of the PD jet, where the experimental results indicated the strain tensor was large; however, assuming inviscid fluid to calculate temperature from the energy equation results in less than a ± 5% difference throughout the majority of the flowfield. Thus, using the inviscid energy equation to calculate temperature from the experimental velocity magnitude is considered to be quantitative.

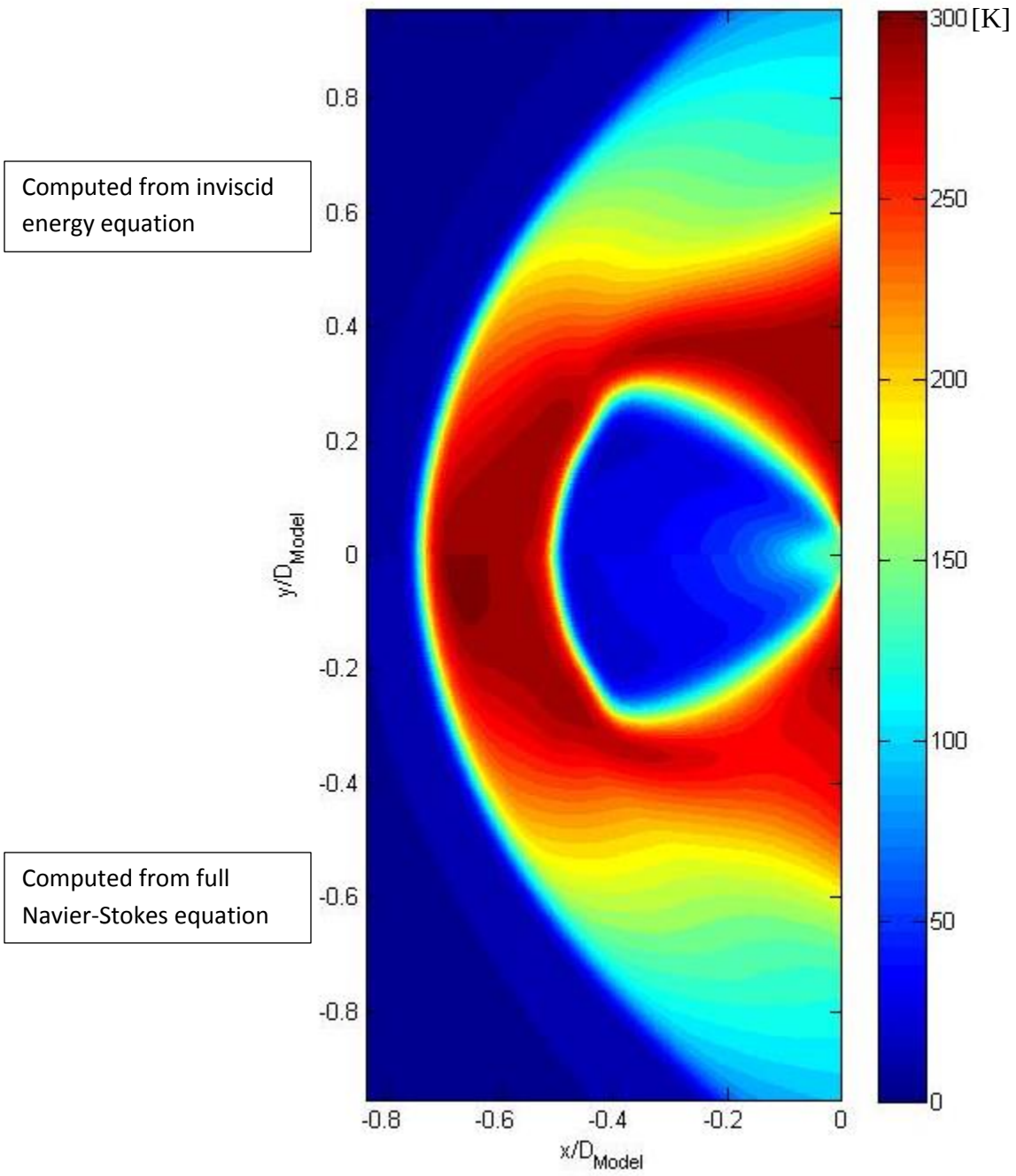

Figure 6.9: Comparison of computed temperature from full Navier-Stokes equations versus temperature computed from inviscid energy equation and CFD velocity results

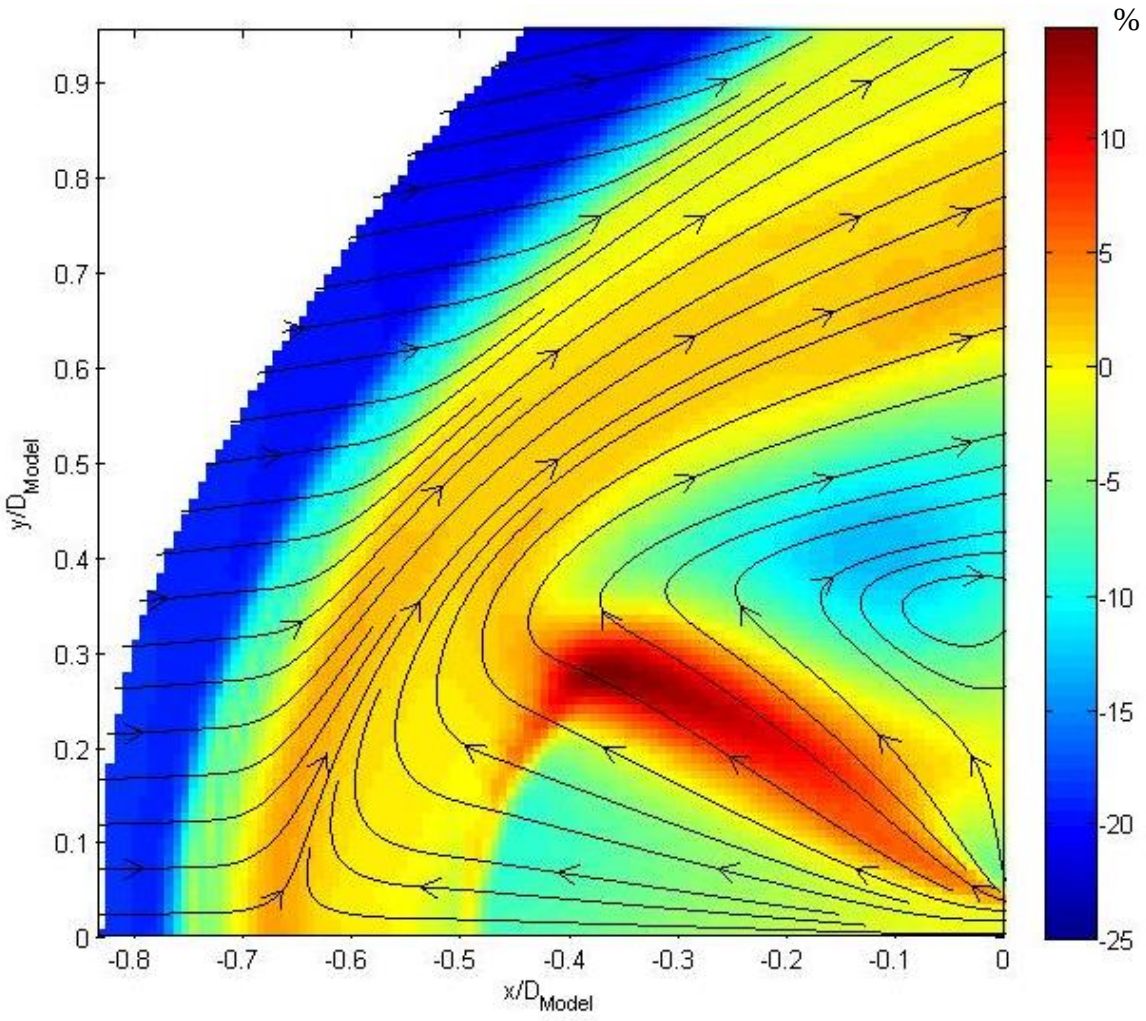

Figure 6.10: Percent difference of temperatures computed from full Navier-Stokes equations versus temperatures computed with inviscid energy equation and CFD velocity results

A comparison of the computational temperature and experimental temperature, calculated from the inviscid energy equation, is shown in Figure 6.11. Freestream flows from left to right, and the PD jet exit is at x/D and y/D of zero. The overall trends in temperature are in good agreement throughout the flowfield. Discrepancies are seen in PD jet size, where the experimental PD jet plume is longer and wider than the computational results; however,the shock stand-off distance is not as great, resulting in a smaller subsonic region where the temperature is

high, near 300K. Due to the larger experimental PD jet size, the recirculation near the bottom of the PD jet plume is smaller. Further, as noted previously, the maximum experimental velocity in the PD jet core is not as great as the computational results, which means the experimental temperature is higher in this region of the flow. Overall flowfield features and trends agree quite well.

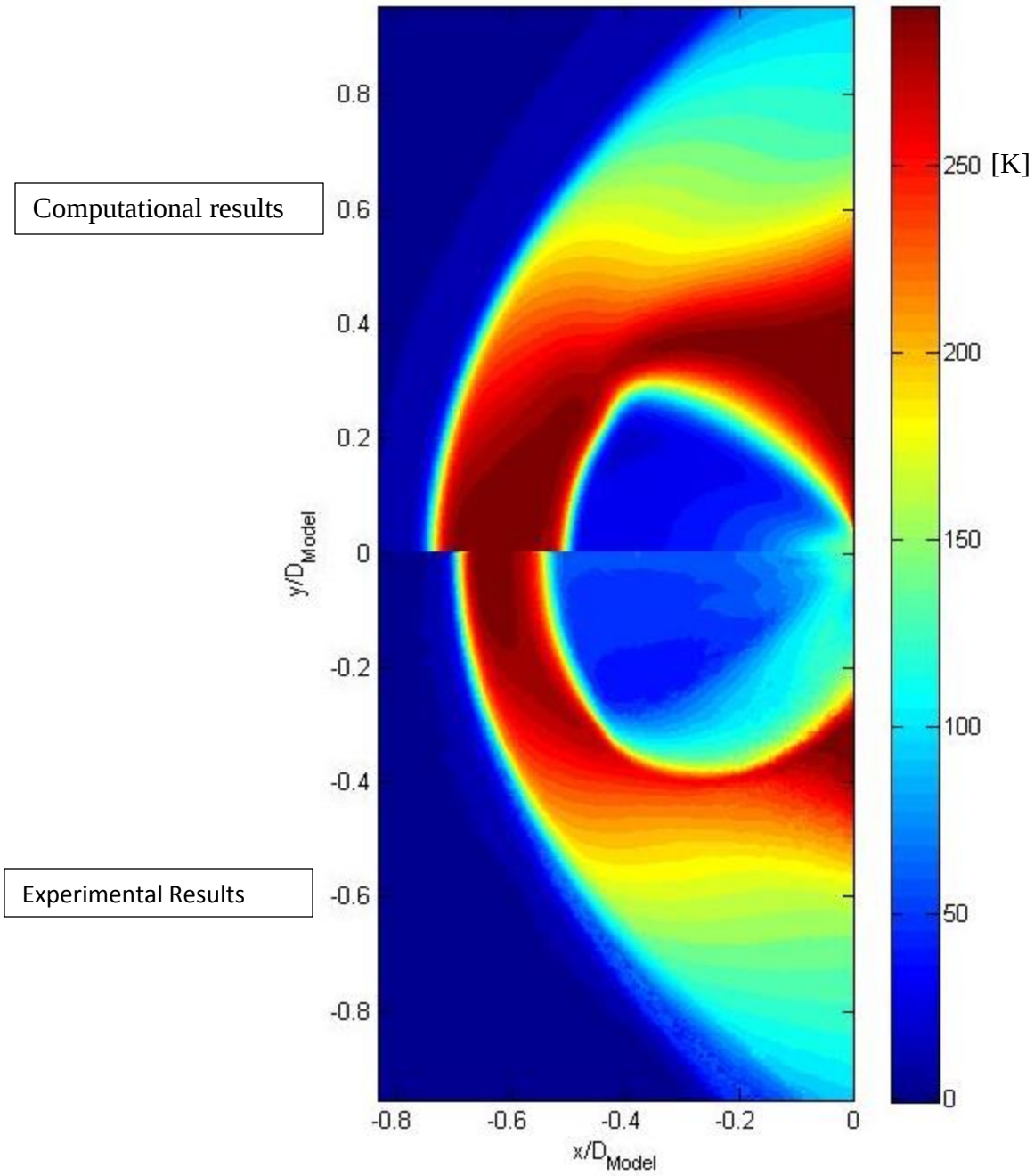

Figure 6.11: CFD temperature versus experimental temperature, computed from inviscid energy equation, $C_T = 1.0$, $M_\infty = 12.0$, $M_{Jet} = 2.66$

CHAPTER 7: QUANTITATIVE QUAD-SUPERSONIC PD RESULTS

This chapter presents experimental planar velocity and temperature measurements for the quad-supersonic PD model with a C_T of 1.0 in Mach 12 freestream flow. The experimental results will be compared with CFD results from the University of Michigan to compare with the CFD predictions.

7.1 Quad-supersonic PD Velocity

7.1.1 Flowfield Symmetry

A Doppler-free visualization of the flowfield was created, as described in Chapter 5, for the quad-supersonic PD jet model in Mach 12 freestream flow and with C_T of 1.0. Freestream flows from top to bottom and the origin is centered on the model stagnation point, x/D and y/D of zero. The laser sheet angle propagates from the top right of the image to the bottom left at an angle of 24.5-deg from the horizontal. The laser sheet is blocked at the model stagnation point on the backside of the model. It is evident from the Doppler-free visualization that the flowfield is symmetric about the model centerline, and using symmetry to cancel impact shift in the following sections is justified.

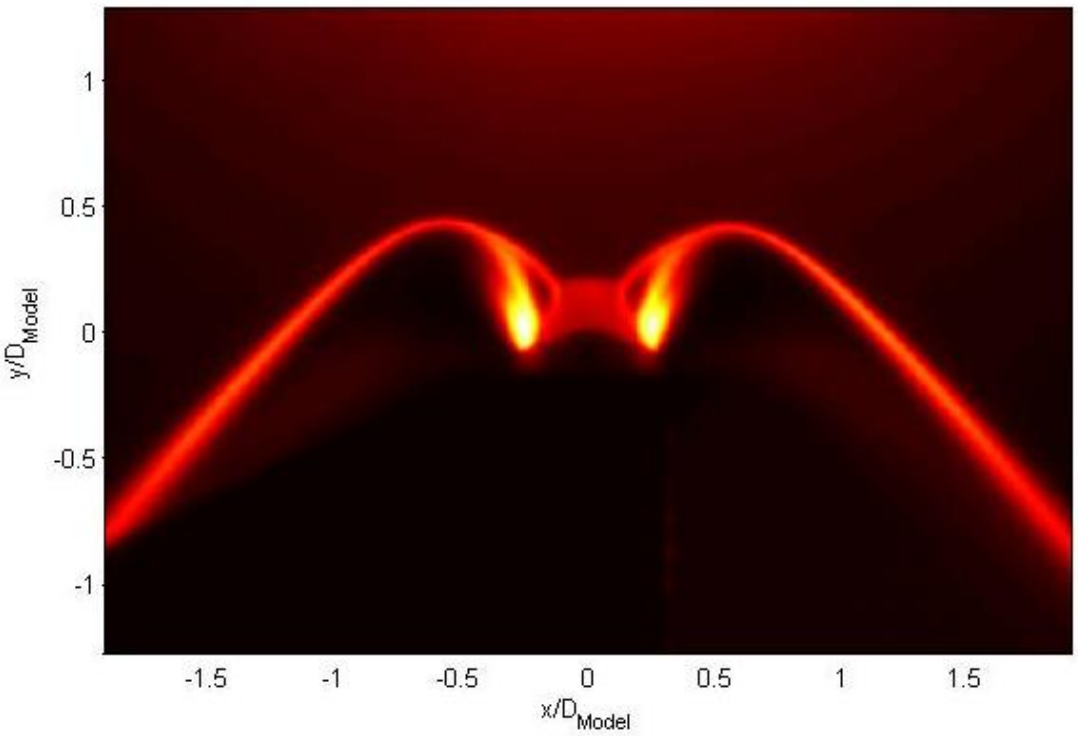

Figure 7.1: Doppler-free visualization of the quad-supersonic PD model, C_T = 1.0, M_{jet} = 2.66, M_∞ = 12.0

7.1.2 Flowfield Characteristics

Planar velocity flowfield magnitude and streamlines for the quad-supersonic PD jet at a C_T of 1.0 are shown in Figure 7.2 and the 2D velocity vector field at reduced resolution, every 7th pixel, is shown in Figure 7.3. Velocity was measured as discussed in Chapter 2, using the symmetry about the model centerline to cancel effects of impact shift. Due to cancelling impact shift the velocity vectors are only resolved for one half of the flowfield, positive x/D, and flipped about the origin. Freestream flows from top to bottom and the model stagnation point is centered at y/D and x/D of zero, where D corresponds to model diameter of 10 mm. Due to limited optical access, the laser sheet angles were set to 24.5-deg and 1.1-deg from the horizontal. Because the second laser sheet angle is so shallow, it was blocked below the stagnation point on the backside of the model and thus it was not possible to cancel impact shift for negative y/D close to the

model shoulder. Thus, for the following case it was not possible to resolve the planar velocity field at the jet exit. For the subsequent discussion upstream will refer to increasing y/D, and radially outward to positive or negative x/D.

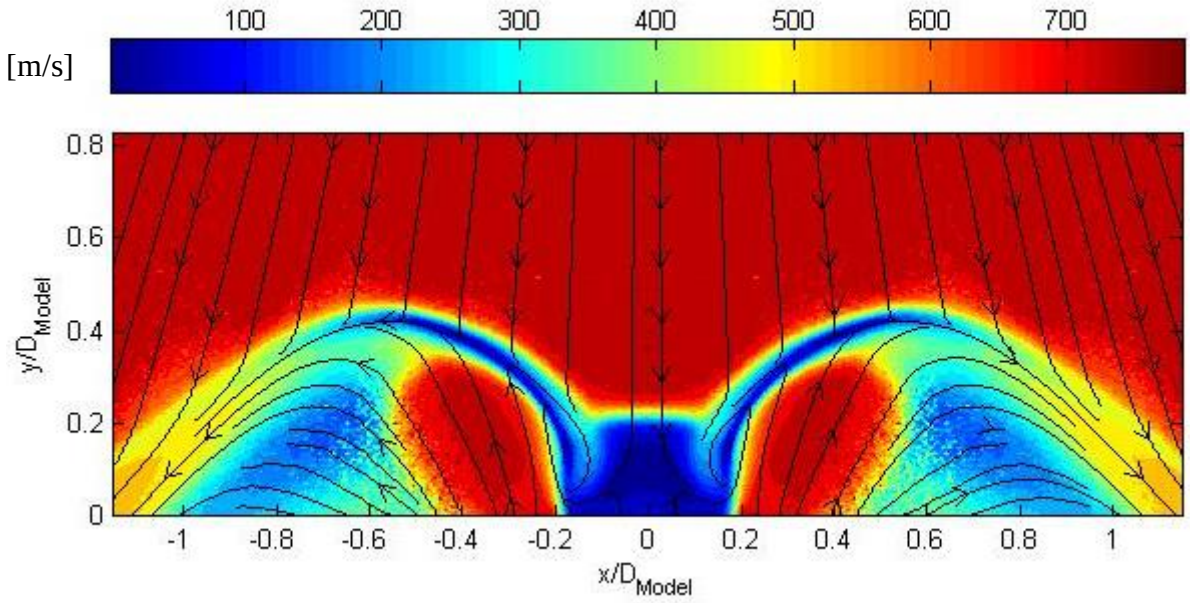

Figure 7.2: Single-supersonic PD jet magnitude and streamlines, CT = 1.0, Mjet = 2.66, M∞ = 12.0

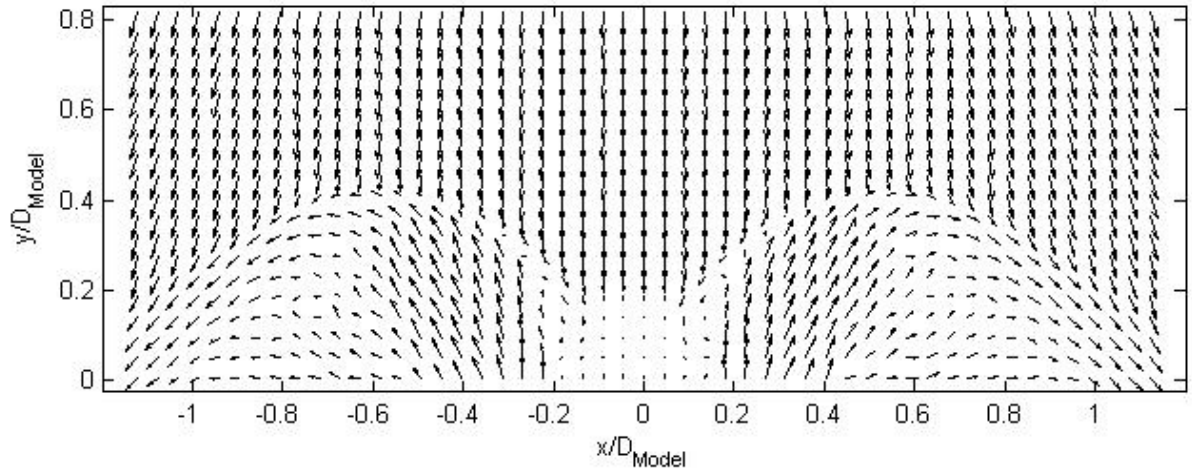

Figure 7.3: Quad-supersonic PD jet 2D velocity vectors, C_T = 1.0, M_{jet} = 2.66, M_∞ = 12.0

The following discussion presents the flowfield features seen in Figure 7.2 and 7.3, and are labeled in Figure 7.4. The PD jet expands and accelerates from the Mach 2.66 jet exit, and

penetrates to approximately 0.35 y/D prior to terminating in a relatively weak shock, at which point it mixes with freestream flow and turns downstream. The freestream fluid compresses in a normal bow shock between the PD jets, and decelerates to a free stagnation point at approximately 0.1 y/D. Entrainment of freestream fluid from the inner PD jet boundary occurs aft of the normal bow shock and forms a recirculation of subsonic fluid that moves back upstream, to the mixed freestream/PD jet region upstream of the weak terminal shock. Entrainment of fluid near the model surface also occurs, accelerating fluid from near the model surface upstream, until intersecting the mixed freestream/PD jet fluid in the bow shock, at which point the entrained fluid turns back downstream. Signal levels in the region between the radially outermost PD jet boundary and shock are relatively low and noisy due to the overall deficiency of iodine in the area; because of the noisy signal levels, the least squares fitting routine was difficult in this area, which will be discussed in the uncertainty analysis appendix.

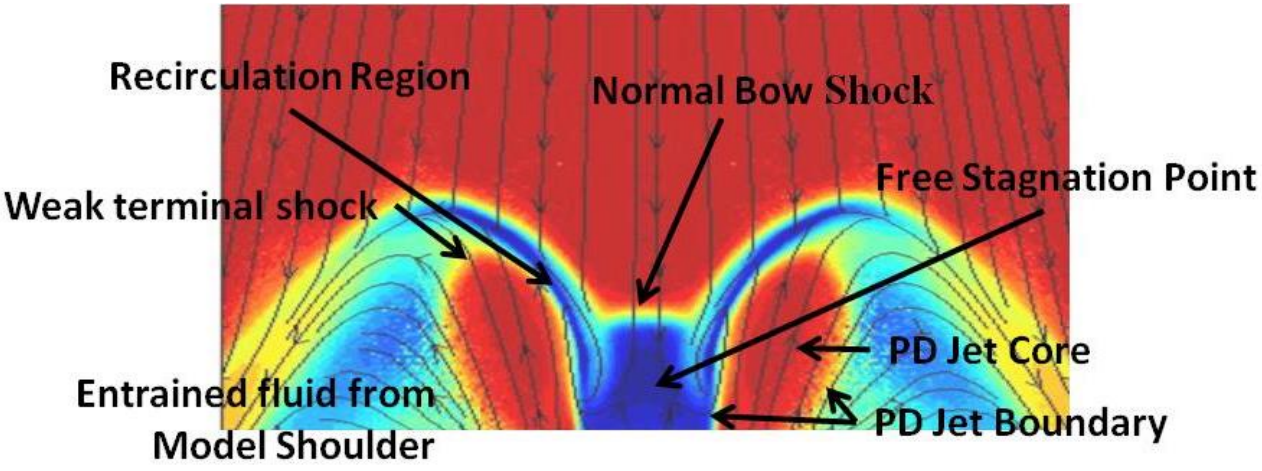

Figure 7.4: Flowfield features overlaid on Figure 7.2

7.1.3 Strain Tensor

The 2D strain tensor is computed using Equation 5.1, and shown in Figure 7.5 for the single-supersonic PD jet model at C_T of 1.0. Freestream flows from top to bottom, the model stagnation point is located at x/D and y/D of 0, and only half of the flowfield is shown due to symmetry. The strain tensor components given by E_{xx} and E_{yy} correspond to expansion and compression in the respective x- and y-directions, positive for expansion, and negative values for compression. Shearing terms are given by E_{xy}, because the strain tensor is symmetric E_{yx} is equal to E_{xy}, and is not shown. Horizontal compression is evident in the oblique bow shock upstream of the recirculation region, at the PD jet boundary, and in the oblique bow shock off-centerline, at x/D greater than 0.6. Expansion in the x-direction is evident in the PD jet core, and recirculation region upstream. As expected, compression is seen in the y-direction at the preserved bow shock between the PD jets, and in the bow shock directly upstream of the PD jet, and some compression is seen in the recirculation region. The greatest shear occurs in the area where fluid downstream of the normal bow shock is turned back upstream by the PD jet boundary, which forms the recirculation region. Shear is also evident in the bow shock directly upstream of the recirculation region, and a very small shearing across where the PD jet fluid and freestream fluid mix upstream of the weak PD jet terminal shock. The vorticity is calculated using equation 5.2, and shock in Figure 7.5(d). The only notable vorticity occurs in the recirculation region, and through the mixing region between the freestream bow shock and weak PD jet terminal shock. These results indicate that the largest viscous effects are expected to be non-negligible in the freestream shock, at the PD jet boundary, and throughout the recirculation region.

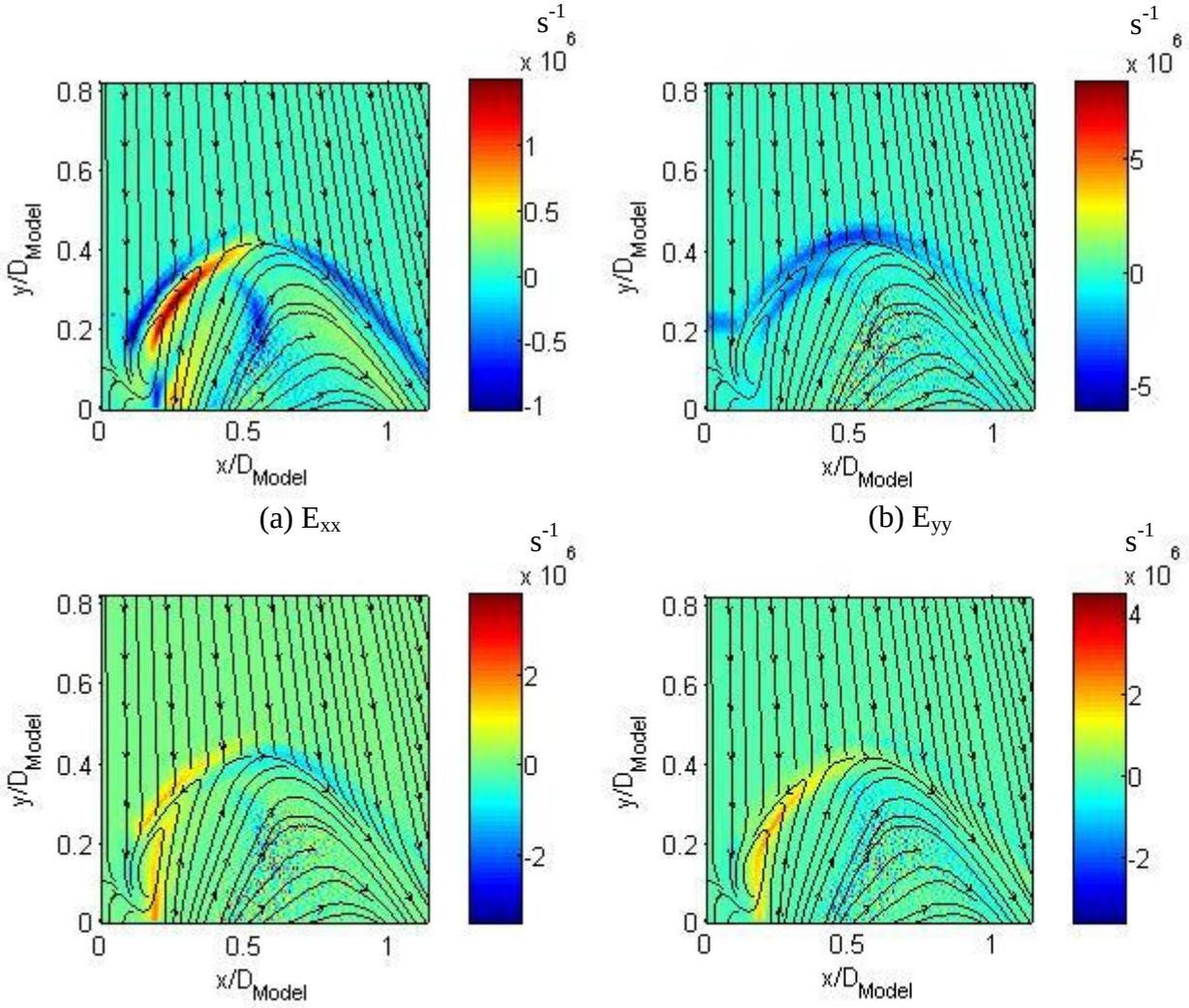

(a) E_{xx} (b) E_{yy}

(c) E_{xy} (d) Vorticity

Figure 7.5: Components of 2D stress tensor and vorticity for half of the flowfield, C_T = 1.0, M_{jet} = 2.66, M_∞ = 12.0

7.2 Quad-supersonic PD Model Temperature

Flowfield temperature, calculated from the inviscid energy equation, is shown in Figure 7.6 for the quad-supersonic PD model at C_T of 1.0. Freestream flows from top to bottom, x/D and y/D of zero corresponds to the model stagnation point. The PD jet exits are at negative y/D and outside of the field of view due to the limited laser sheet angles. The temperature is low throughout the PD jet cores, until the weak terminal shock is reached, at which point the fluid heats up to approximately 200K. Total temperature recovery from the freestream fluid occurs in

the normal bow shock between the PD jets, with the average temperature being about 300K. In the subsonic recirculation region inboard of the PD jet boundary, temperature also remains high, at nearly 300K. As the recirculating fluid reaches the intersection point of the PD jet fluid and freestream bow shock over the PD jet, the flow accelerates downstream and temperatures decrease to approximately 200K; in this region the flow contains an oblique shock. Entrained fluid from the model surface also remains at a relatively high temperature, in the range of 250K.

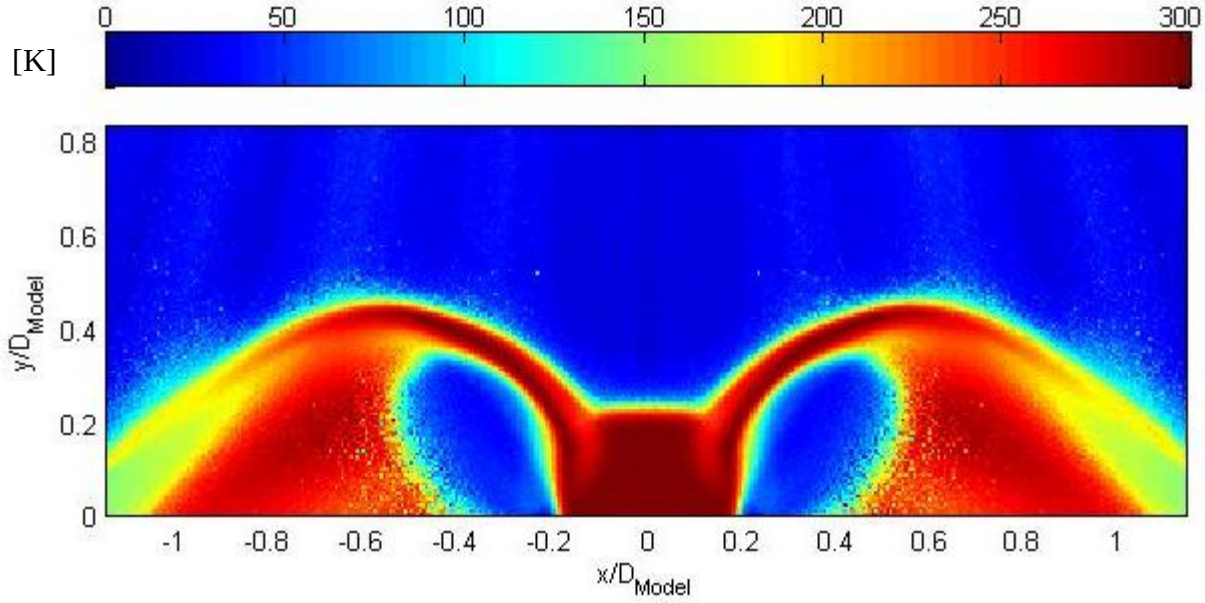

Figure 7.6: Quad-supersonic PD model inviscid temperature calculation, C_T = 1.0, M_{jet} = 2.66, M_∞ = 12.0

7.3 Comparisons with CFD

Experimental velocity and temperature will be compared with numerical simulations executed using LeMANS, a parallelized CFD code for simulating hypersonic reacting flows, and described in Chapter 4.

7.3.1 Velocity

Experimental velocity magnitude and streamline results are compared with LeMANS CFD solutions in Figure 7.7. In Figure 7.7 the freestream flows from left to right and the jet exit

nozzle is located at x/D and y/D of 0. The CFD results are shown for positive y/D values, and the experimental results are negative y/D, where D corresponds to the model diameter of 10 mm. The CFD results capture the overall flowfield trends seen in the experimental results. Most notably, the recirculation region and low velocity region between the inward PD jet plume and freestream bow shock; although, similar differences as shown in the previous Chapters are also noted. The experimental normal bow shock is farther downstream than in the corresponding CFD results, and the experimental PD jet plume is longer, as well as wider, than that shown in the CFD results. Furthermore, the CFD results indicate the stagnation point is at the typical location for blunt body flow, on the aeroshell center, whereas the experimental results show that a free stagnation point forms on the centerline at y/D of 0.1. It is presently unclear why a free stagnation point would occur. One possibility is entrainment of fluid between the PD jets occurs, causing fluid near the model surface to move upstream and intersects the compressed freestream fluid flowing downstream at the free stagnation point.

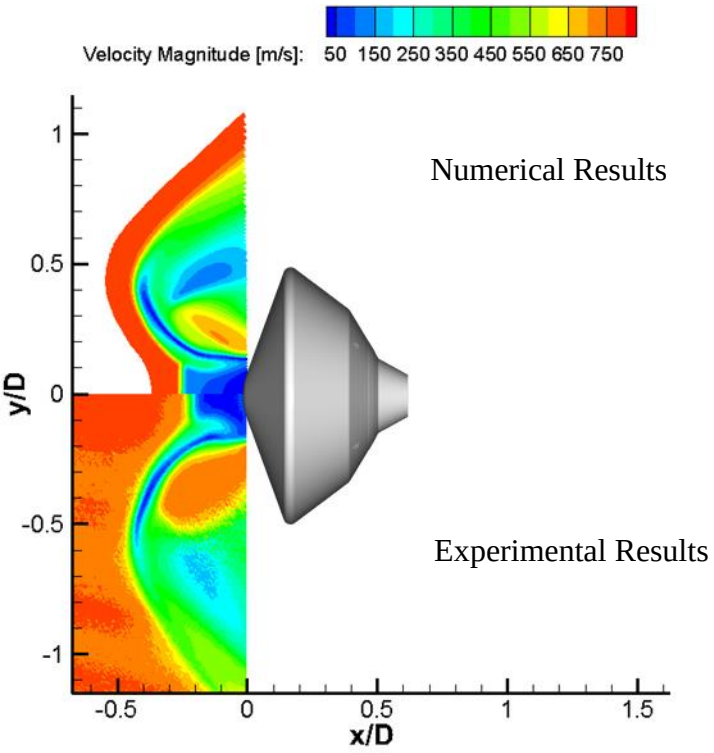

(a) Velocity magnitude

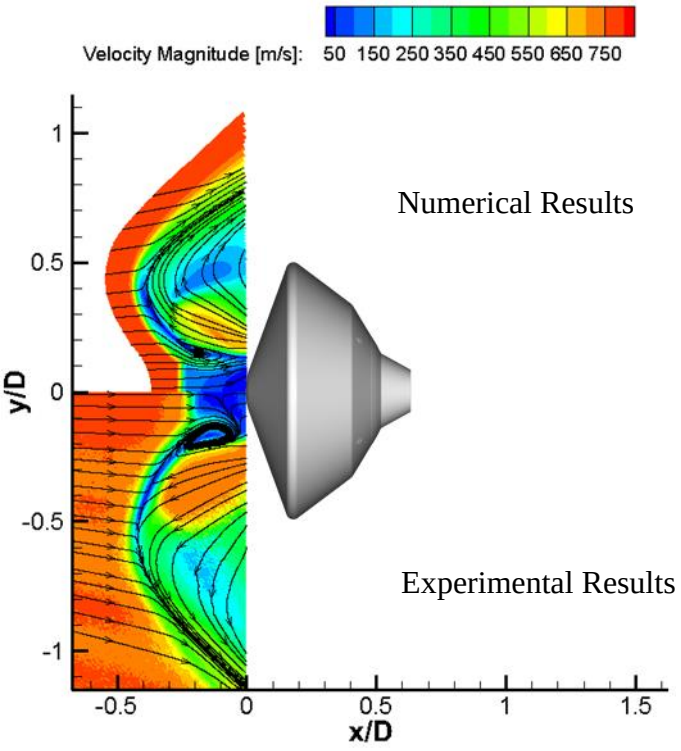

(b) Velocity magnitude and streamlines

Figure 7.7: Comparison of CFD (top) velocity magnitude and streamlines to experimental (bottom), C_T = 1.0, M_∞ = 12.0, M_{Jet} = 2.66

Experimental and computational velocity magnitudes are compared in Figure 7.8 along four profiles in the flow: at the model centerline through model bow shock, and three cross-sectional cuts at constant y/D of 0.075, 0.15, and 0.2. The centerline comparison, Figure 7.8(a), shows the freestream velocity is in good agreement between experimental and computation results. The bow shock, which is indicated by the sharp decrease in velocity magnitude, occurs farther upstream for the CFD results than the experimental results, and the bow shock thickness is greater in the experimental results (the rate decrease in velocity is not as great). After the bow shock the CFD results indicate the fluid gradually slows, until a stagnation point at the model surface; whereas the experimental results decrease to a minimum velocity at about -0.1 x/D, then show a slight increase in velocity until reaching the aeroshell surface.

For the cross-sectional profiles, Figure 7.8(b)-(d), the comparison begins at y/D of 0, and through the compressed freestream flow, recirculation region, and through the PD jet core. Beginning in the low-velocity region downstream of the freestream bow shock, and radially outward, the velocity increases through a small section of flow near the PD jet boundary. This high-velocity region is from freestream fluid that passes through a relatively weak oblique shock near the upstream recirculation region. After the high-velocity region, the recirculation region occurs, which is from freestream fluid that is turned back upstream from interacting with the PD jet boundary. A sharp increase in velocity occurs along the line through the PD jet boundary, and remains relatively constant in the jet boundary for the experimental results, but decreases slightly for the CFD results. At the far PD jet boundary the fluid velocity again decreases. It is evident from the profile comparisons that the experimental PD jet boundary is much wider than the computational results. The overall trends shown by the CFD and PD results are in good agreement; however, the location of various flow characteristics is slightly different.

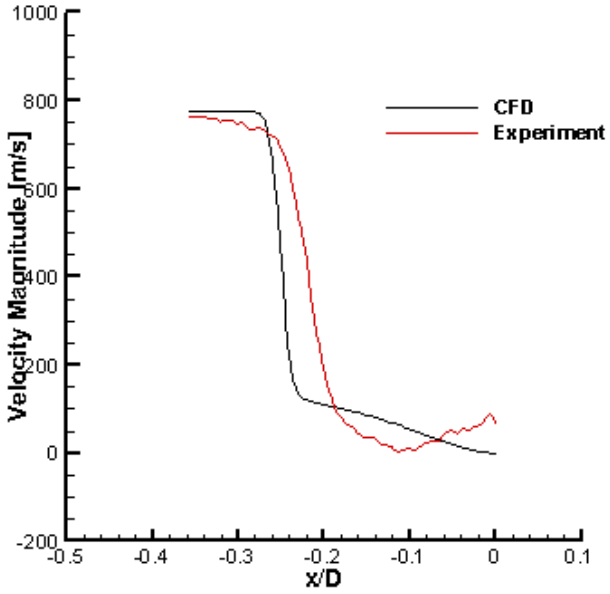

(a) Centerline comparison at y/D = 0

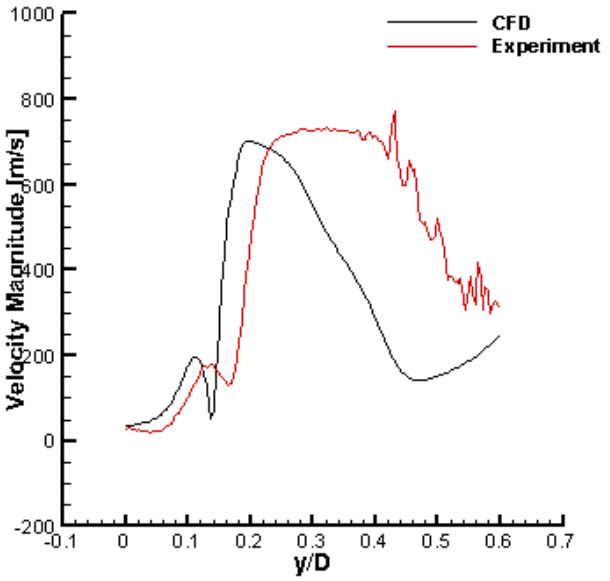

(b) Cross-sectional cut at x/D = 0.075

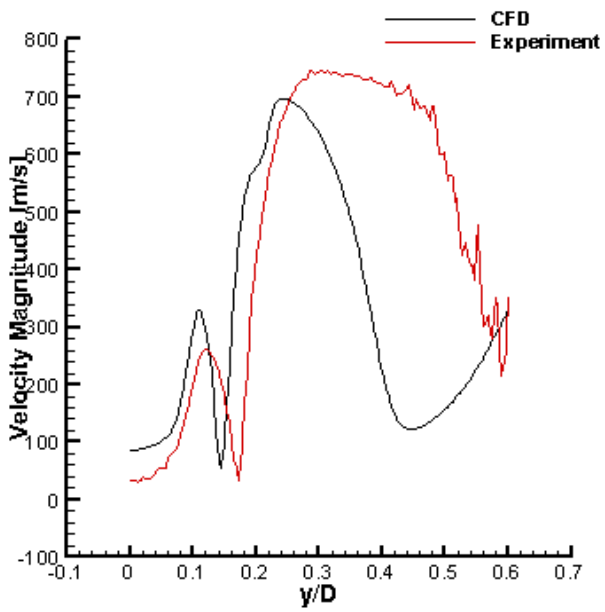

(c) Cross-sectional cut at x/D = 0.15

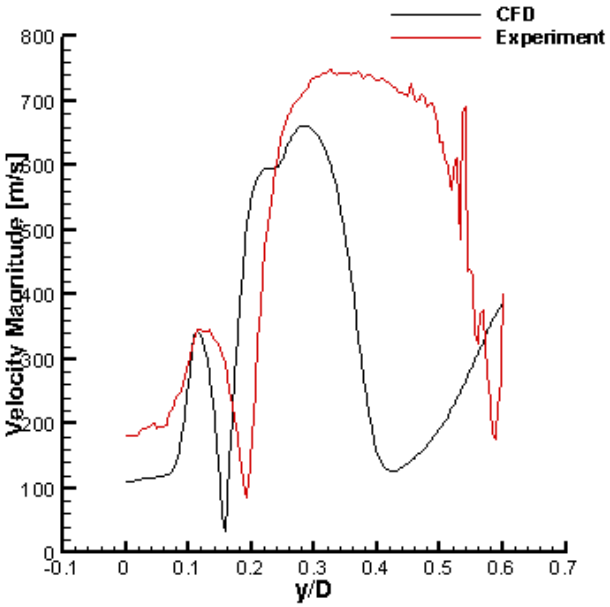

(d) Cross-sectional cut at x/D = 0.2

Figure 7.8: Centerline and cross-sectional cuts through PD jet core comparisons between CFD and experimental results

7.3.2 Temperature

The inviscid energy equation is used to compute flowfield temperature from the measured velocity magnitude; however, it was shown by examining the experimentally measured strain tensor that areas of the flowfield might have significant viscous effects. In addition to the strain tensor calculation, the CFD solution is used to compare temperature from the full Navier-Stokes solution, considering viscous effects, and the inviscid energy equation. Temperature computed from the inviscid energy equation, using CFD results for velocity magnitude, and temperature computed from the solution to the full Navier-Stokes solution, with viscosity, are shown in Figure 7.9, where the inviscid energy equation is used to calculate temperature for positive y/D, and the Navier-Stokes solution is used to calculate temperature for negative y/D. Freestream flows from left to right, and the model centerline is at x/D and y/D of zero. Overall, the two computed temperatures are in good agreement throughout the majority of the flowfield, indicating viscous effects are largely negligible. To quantify exactly where viscous effects might be non-negligible, the percent difference between the two temperature solutions is shown in Figure 7.10. As expected from the examining the experimental strain tensor, areas of the flowfield with the greatest viscous effects produce the greatest percent difference, especially in the freestream bow shock, and recirculation region between the PD jet boundary and bow shock. In these areas, the solution for temperature results in an approximately a 10% difference. The freestream flow has up to a -22% difference, but temperatures in this region are low, so a small variation in temperature results in a large percent difference. Overall, the use of the inviscid energy equation to calculate temperature is adequate for the majority of the flowfield.

Computed from inviscid energy equation

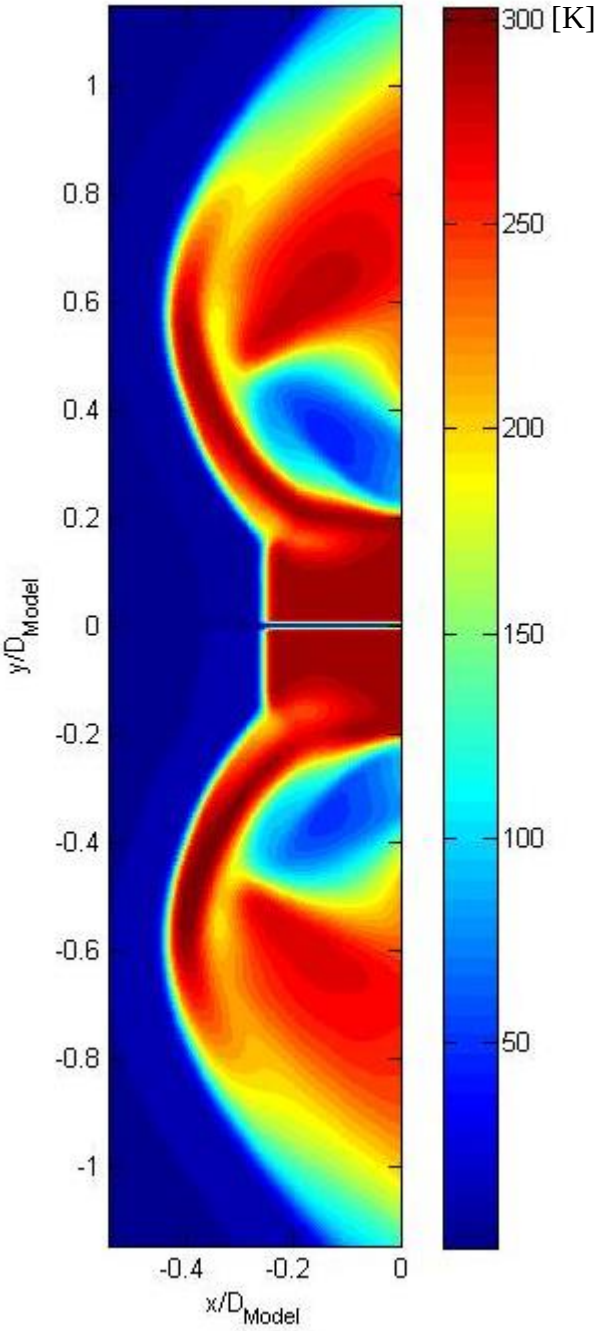

Computed from full Navier-Stokes

Figure 7.9: Comparison of computed temperature from full Navier-Stokes equations versus temperature computed from inviscid energy equation and velocity from CFD results

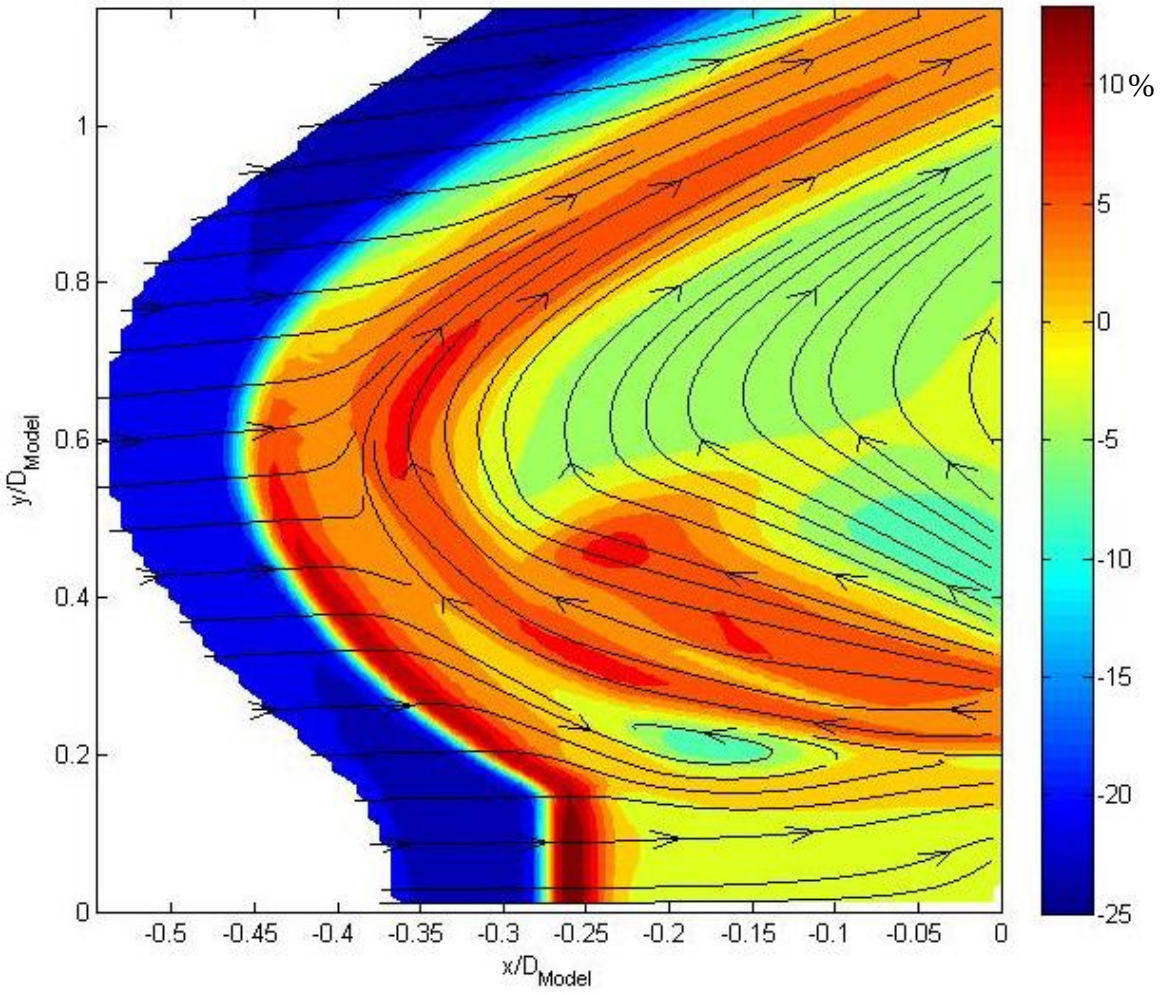

Figure 7.10: Percent difference of temperatures computed from full Navier-Stokes equations versus temperatures computed with inviscid energy equation from CFD results

A comparison of the computational temperature and experimental temperature, calculated from the inviscid energy equation, is shown in Figure 7.11. Freestream flows from left to right, and the model centerline is at x/D and y/D of zero. As expected from the velocity comparison, overall differences in the shock stand-off distances, PD jet penetration, and PD jet width for the experimental and computational results are apparent. However, the overall temperature trends are in very good agreement. The low-velocity region downstream of the bow shock remains near room temperature, as well as the recirculation region and mixing region between the PD jet and normal bow shock. Overall temperatures throughout the flowfield are in good agreement.

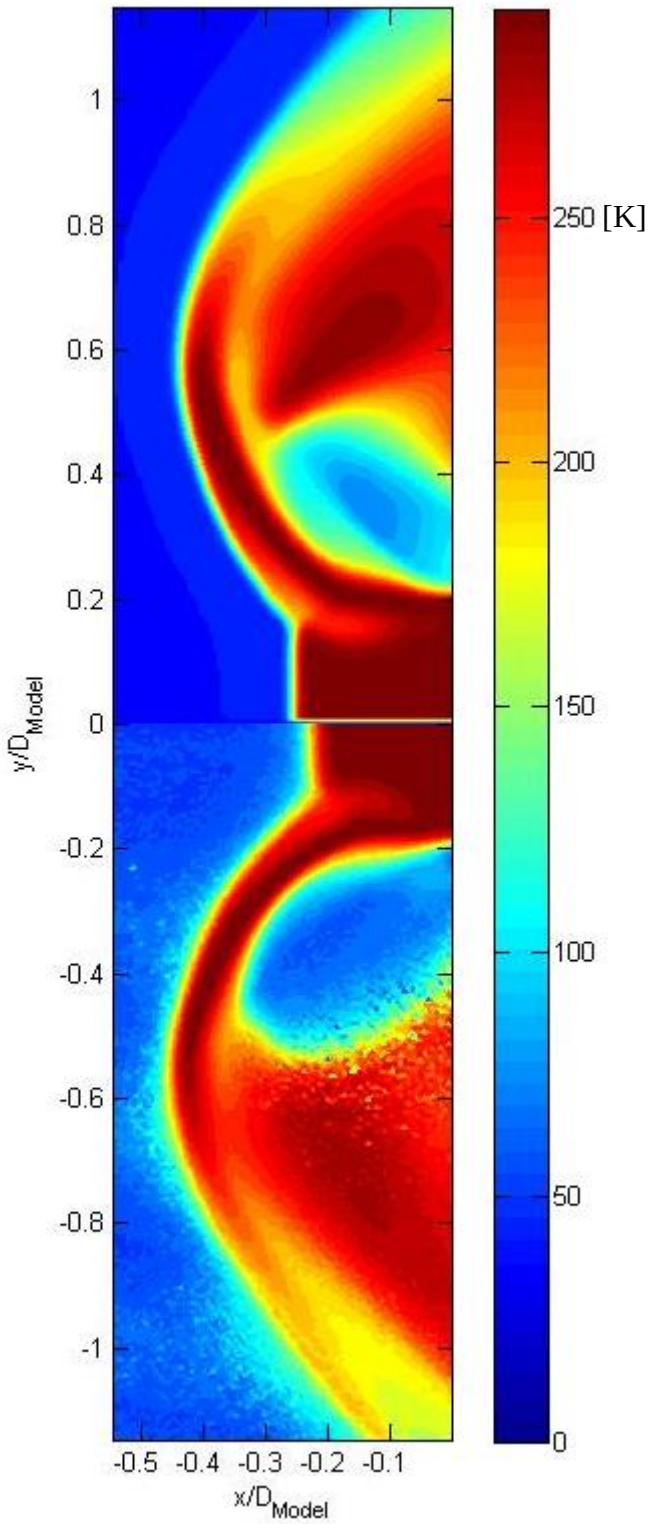

Figure 7.11: CFD temperature versus experimental temperature, computed from inviscid energy equation, $C_T = 1.0$, $M_\infty = 12.0$, $M_{Jet} = 2.66$

CHAPTER 8: CONCLUDING REMARKS

Planar laser-induced iodine fluorescence has been applied to four flowfields of interest: a single-sonic PD jet model, a single-supersonic PD jet model, a quad-sonic PD jet model, and a quad-supersonic PD jet model in Mach 12 freestream flow. Qualitative experimental visualizations were obtained for a range of thrust coefficients for each model to examine and reduce possible shock-shock interactions between the model bow shock and freestream shock structure, as well as provide visualizations for CFD validation. Quantitative PD jet mole fraction was measured for a single coefficient of thrust, 1.5, for both the quad-sonic and supersonic PD jet models, and compared with CFD results. Quantitative planar velocity and temperature were measured and reported for the single-sonic and supersonic PD jet models, as well as the quad-supersonic PD jet model with a thrust coefficient of 1.0 for all cases.

8.1 Visualizations and Mole Fraction

By examining shock-shock interactions in Chapter 4, it was determined a 10 mm diameter model was necessary to minimize these interactions for comparisons with computational results. Also, a small coefficient of thrust was chosen to minimize shock-shock interactions between the model bow shock and freestream shock structure. Although, for practical application of PD jets, larger thrust coefficients are desirable, in order to minimize the interaction, while still providing data for larger jet thrust, it was determined to use C_T of 1.5 and 1.0 for quantitative measurements. Experimental visualizations were compared with CFD results from the University of Michigan, and good agreement was found in shock stand-off distance for most thrust levels; however, at larger thrust levels, the computed shock stand-off distance disagreed for supersonic PD jet models, likely due to the increased shock-shock interaction.

Quantitative PD jet mole fraction was measured for the quad-sonic and supersonic PD jet models and verified a normal bow shock is preserved between the peripherally located PD jets over the model stagnation point. The presence of the bow shock indicates a high pressure region will be maintained on the aeroshell forebody near the centerline, and preserve aerodynamic drag, unlike for the single-central PD jet models. Preservation of the aerodynamic drag is desirable because less thrust is needed to adequately slow a lander, thus saving weight either in reduced propellant mass fraction, or reduced weight from smaller engines. The experimental PD jet mole fraction was compared with CFD results and showed overall good agreement along line profile comparisons.

8.2 Velocity and temperature measurement conclusions

For planar velocity measurements an assumption of flowfield symmetry was necessary. By developing a "Doppler-free visualization" technique using narrowband frequency measurements, the flowfield was confirmed to be symmetric about the model centerline for all three velocity measurement test cases.

8.2.1 Single-nozzle PD jet models

Velocity magnitude and streamlines were found to be in good agreement with expected flow features for the single-nozzle PD jet models. Due to difficulties encountered in using planar laser-induced fluorescence to measure temperature, the inviscid energy equation was used with the measured velocity magnitude to compute planar temperature. With the 2D velocity measurement it was possible to compute the strain tensor, and it was determined that viscous effects were negligible throughout the majority of the flowfield. This was also confirmed by comparing CFD temperatures computed from the full viscous Navier-Stokes equations, and temperature computed from the inviscid energy equation with CFD velocity results; the overall

percent difference in computed temperature due to viscous effects was the largest in the PD jet shear layer with a 10% difference.

Comparisons of experimental and CFD results show the computations have the same overall trends as the experimental results; however, the experimental PD jet was consistently measured to be larger, wider, as well as longer. Furthermore, the experimental shock stand-off distance was over-predicted by the computations, resulting in a larger subsonic velocity region between the PD jet terminal shock and model bow shock. Inviscid temperature comparisons showed good qualitative agreement between the experimental results and computational results, but also had the same differences in PD jet size and bow shock stand-off distance. Experimental results also confirmed the recirculation region which forms near the shoulder of the model shoulder is a function of PD jet width. As the PD jet thrust increases, the jet width increases, which causes the recirculation region to decrease in size.

8.2.2 Quad-nozzle PD jet model

Experimental velocity and temperature measurements confirm a normal bow shock is preserved between the PD jets upstream of the model centerline, suggesting a high pressure region is maintained and aerodynamic drag is preserved. A recirculation region forms inboard of the PD jets from freestream fluid turning back upstream from the bow shock region. The strain tensor was computed from experimental results and suggests viscous effects will be negligible for the majority of the flowfield; areas with viscous effects will be localized to the recirculation region, model bow shock, and PD jet boundary. Because viscous effects are expected to be negligible for most of the flowfield, the inviscid energy equation was used to calculate planar temperature from the velocity magnitude.

CFD computations also confirmed the temperature computed from the full Navier-Stokes equations, with viscous effects, and temperatures computed from the inviscid energy equation are in good agreement. The largest error from computing the temperature with the inviscid energy equation is limited to the localized regions measured by the experimental strain tensor. Overall, the flowfield trends from the computational results are in very good agreement with the experimentally measured trends; however, similar to the single-nozzle PD jet models, the experimental results have a larger PD jet structure, and smaller shock stand-off distance than the computational results.

8.3 Importance of work to PD jet research

To the best of the authors' knowledge, this work is the first spatially resolved, non-intrusive quantitative experimental data available for HRP PD jet flowfields. Experimental wind tunnel data is valuable for computational code validation, which will be necessary for designing future high mass Mars missions.

8.4 Recommendations for future work

In Chapter 1 it was mentioned that previous experimental research indicated areas of periodic flow unsteadiness for single-nozzle PD jet configurations at certain thrust conditions. For the work presented, it is estimated, based on model size, that periodic flow unsteadiness would be on the order of about 17 KHz, indicating the time-averaged velocity flowfield measured gives a good result. However, it would be useful to apply a high speed velocity measurement technique to measure instantaneous velocity flowfields, such as femtosecond laser molecular tagging, which uses a powerful laser source to dissociate nitrogen molecules, and measure the photon emission from re-combination with a time-gated camera.[59] Such measurements would be useful for time-dependent code validation and verification.

Possible improvements to the current experimental measurement technique could be to further investigate the possibility of transition-dependent redistribution of the upper-electronic state, as mentioned by Donohue,[36] for the T-ratio measurement approach. The relationship in Equation 2.10 was determined for the P13/R15 peak only; however, if the redistribution of the upper electronic state is transition-dependent, then it is likely necessary to perform static cell studies to compute a similar empirical relationship for the P48/P103 peak. Thus it might be possible to eliminate the need for a T-ratio correction factor.

Due to various difficulties encountered in running the experiment, it was only possible to measure velocity and temperature once for each model studied (however, measurements were attempted multiple times). Currently, experimental run times for narrowband spectral scans require approximately 12 hours to collect two laser sheet angles in a single experiment. For a typical experiment, the laser and vacuum pumps are typically running for about 3-4 hours before it is possible to collect any data. While it is unlikely to reduce the start-up time necessary, it is possible to reduce the amount of time to obtain each narrowband scan over the absorption profile. Once the narrowband laser scan is started, it only requires about 15-30 minutes to scan through the P13/R15 peak in 25 MHz step sizes (typically about 130-210 data points depending on the flowfield Doppler shift), depending on camera exposure times and laser scan rate (1.5s exposure times were possible for all experimental data in the current work). However, due to controlling pressures for the freestream and PD jet flows via a needle valve, it is necessary to periodically stop data collection to re-adjust the pressures and maintain a constant C_T. Each time the pressure is adjusted, data collection is typically delayed 5-15 minutes, causing the time to scan over the P13/R15 peak to increase to 1-2.5 hours. Furthermore, each time the PD pressure is adjusted there is a small possibility the laser sheet optics will also need to be re-aligned due the

possibility of misaligning optics while attempting to reach the PD jet needle valve control. If an automated flow control were added to the experiment, the need to constantly adjust the PD jet pressure would be eliminated, and thus it could be possible to obtain up to 2-5 more laser sheet scans in the same amount of time for repeatability purposes. It would still be necessary to ensure the laser sheet remains aligned throughout the experiment, but once the lab reaches thermal equilibrium (the vacuum pumps heat the lab anywhere from 10-15 deg-F), the laser sheet optics are very stable.

APPENDIX A: EXPERIMENTAL PROCEDURE CHECKLIST

A.1 Start-up

The following checklist can be used for a standard experimental run for single-mode laser operation. Some steps are not necessary for visualization or mole fraction experiments. The following checklist assumes the model is properly aligned and laser sheet optics have also been aligned prior to start-up.

1. Turn on pit water pump, open main water valve in pit, turn on Neslab heat exchanger, check water level on Neslab and fill with distilled water if necessary (Neslab heat exchanger located under Lab 124E, trap door between optics tables)
2. Turn on power meter, o-scope, J-Lok, Z-Lok, photodiode, Klinger stepper motor, camera chiller, and etalon heater
3. Display laser warning safety signs outside all lab entrances
4. Open laser housing to access etalon, insert safety lockout pin to casing switch
5. Turn on breaker to laser, under optic table
6. Turn on laser, set mode to Constant Power, let warm up at approximately 1.0W for 2 hours. Locate flashpoint by adjusting horizontal and vertical etalon tilt if necessary
7. Check oil level in Stokes 412 pump, re-fill oil if necessary
8. Open orange ball valve above Stokes 412 pump
9. Ensure proper oil drain valves under optic table next to vacuum chamber are open/closed
    a. 3 valves to drain oil from Roots 1236 pump open
    b. Valve to nitrogen farm closed
    c. Valve to oil drain line closed
10. Open baffle under vacuum chamber
11. Ensure vacuum chamber door securely closed, apply C-clamps if necessary

12. Turn breaker for Stokes 412 (labeled) on, start Stokes 412 pump. Allow vacuum chamber to reach sufficient vacuum before turning on booster pumps, about 10-15 minutes
13. Turn on Roots 615 booster pump
    a. Wait another 10-15 minutes prior to next step
14. Turn on Roots 1236 booster pump
15. Monitor vacuum chamber pressure using MKS gauge, Hastings gauges can be used to check vacuum pump pressures
16. Open N_2 cylinders outside, open valves on control board and downstairs to allow N_2 to enter iodine mixing vessel
    a. Allow mixing vessel pressure to stabilize to allow appropriate seeding fraction
17. Turn on freestream and model flow, adjust pressures with needle valves to obtain desired C_T
    a. Until flow has settled, about 30-45 minutes, pressures will constantly need to be monitored and re-adjusted

A.2 Scanning Laser

The following checklist can be used start an experimental laser scan for velocity/temperature measurement. This list assumes the laser has been started and allowed to warm up, necessary equipment is on such as the camera, J-Lok, Z-Lok, oscilloscope, etc, and the the laser is on flash point, and the DAQ program is opened in Labview.

1. Check laser power calibration, re-calibrate if necessary
    a. Set laser power to various values, ex. 0.50, 0.75, 1.00, 1.25, etc, and record voltage readout on computer. Fit line and update equation in Labview DAQ program.

2. Reset Klinger
3. Rotate vertical tilt away from you (clockwise direction if looking at the high-reflector side of the laser, counter-clockwise if viewing laser from output coupler) to move laser off flashpoint
4. Set data file
5. Take single frequency, p-number of data points in Labview DAQ program to set relative frequency scale
6. Laser will be near P48/P103 absorption peak at this point, if it is desired to start the laser scan near the P13/R15 peak, then "go to" specific frequency approximately 10 GHz greater than current
7. To scan down through P13/R15 peak, select "hop down" to minimum frequency, adjust minimum frequency based on relative frequency scale, adjust frequency step size, and select variables to record, hit "Do It" to start
    a. Alternatively, the laser can be scanned up by selecting "hop up" to maximum frequency

A.3 Shut Down

The following checklist should be used to shut down after an experimental run is concluded.

1. Return laser to flashpoint
2. Turn off laser at laser remote control
    a. Note, the laser needs to cool completely before shutting off water flow and breaker, typically about 15 minutes is needed, but the temperature can be monitored by touch using black water input/output lines to laser housing
3. Shut off nitrogen/iodine flow to freestream and model

4. Close valves to stop nitrogen flow to iodine mixing vessel
5. Turn off 1236 blower, shut off break, allow blower to finish spinning down, then repeat process for 615 blower, and finally Roots 412 pump
6. Close orange ball valve above Stokes 412 pump
7. Open vacuum vessel fill valve from control board
8. Open valve on side of vacuum chamber to re-fill vacuum chamber and vacuum pumps with dry nitrogen, monitor pressure levels while filling vacuum chamber to atmospheric pressure
    a. Once finished, close all valves, close regulator and cylinders at nitrogen farm
9. Close laser breaker when laser is sufficiently cooled
10. Remove laser warning signs
11. Shut off Neslab chiller
12. Turn off pit water pump
13. Close main water valve in pit

APPENDIX B: UNCERTAINTY ANALYSIS

In this Appendix the total experimental uncertainty for the planar velocity measurement due to random and systematic error is considered. Random error is due in part to the shot noise of the CCD camera. Due to the complexity of the measurement technique, systematic error can be related to a number of sources. For instance, fixed pattern noise of the CCD due to imperfections in manufacturing and reflections in the wind tunnel are addressed by background subtraction. The two primary forms of systematic error considered in the following discussion are laser sheet angle calculations, and the location of the line of symmetry in the flowfield. The total computed uncertainty in velocity will be used to estimate uncertainty with temperatures computed from the inviscid energy equation.

B.1 Velocity Uncertainty Analysis

As discussed in Chapter 2, flowfield velocity measurements primarily depend on the ability to accurately measure the linecenter frequency relative to an unshifted static cell, and the linecenter frequency of Doppler-shifted absorption spectra in the flowfield in order to calculate the change in frequency. To accomplish this, a least-squares spectral fit of the measured absorption spectra using equation 2.2 is used. Once the change in frequency is computed, equation 2.26 and 2.27 are applied to relate the measured frequency shift to a Doppler shift in the direction of the corresponding laser sheet angle. The Doppler shift is related to the velocity component by equation 2.21, and a coordinate transform, given by equations 2.28 and 2.29, is used to relate the velocity to the natural coordinate system of the experiment. Therefore, the total uncertainty in velocity is primarily due to three possible sources of error: goodness of the spectral model fit for frequency shift to measured absorption spectra, uncertainty in cancelling the impact shift, and

uncertainty in the laser sheet angle. The total uncertainty in velocity measurements will be calculated in the following sections.

A. Uncertainty in fitted frequency

Random error in the experimentally measured spectra is sufficiently characterized as white noise. The white noise is considered to be due to a multiplicative factor and additive factor. To estimate the additive factor, a moving average filter (low pass filter) is applied to the measured absorption signal and the difference of the total signal and filtered signal is taken to isolate high frequency noise. The median of the high frequency noise is taken and normalized by the measured spectra to give percent noise for the additive factor. The multiplicative factor is determined by subtracting the additive factor from the high frequency noise and normalizing to give percent noise. A Fast-Fourier Transform was applied to check for high frequency signal, which would artificially increase the calculated percent noise, however high frequency signal is only noted for hyperfine spectra, where the total calculated percent noise is typically less than 1%. No high frequency signal is present in the continuum region where spectra are pressure and temperature broadened.

The resulting multiplicative percent noise is shown in Figure B.1, and a log plot of the percent noise is shown in Figure B.2, for each experimental model and laser sheet angle. Images are oriented the same as presented in Chapters 5, 6, and 7, with x/D and y/D (D being the model diameter of 10 mm) corresponding to the PD jet exit for single-nozzle models, and the model stagnation point for the quad-nozzle PD jet model. For the following discussion the signal to noise ratio (SNR) will typically be referred to, which is equal to the inverse of the percent noise divided by 100. The SNR is quite good throughout the freestream, model bow shock, and PD jet core. However, for the single-nozzle PD jet models, the SNR is poor in regions outside of the PD

jet core near the model surface (where the percent noise is large). For the quad-nozzle PD jet model, the SNR is poor in the region outside of the PD jet between the model bow shock and shoulder. To gauge the effect of the SNR on the quality of fit, spectra are generated for known pressure, temperature and frequency shift and perturbed by percent noise associated with areas of the flow where SNR is good, and areas of the flow where SNR is low.

Estimated uncertainty in the measured frequency shift and corresponding uncertainty in velocity is shown in Table B.1. The sensitivity analysis was performed for four cases with additive and multiplicative percent noise being equal to: 1%, 5.5%, 7.5%, and 11%. These values were chosen to be representative of areas of the flow where SNR is very good, such as in the PD jet core and freestream, and areas of the flowfield where SNR ratio is low. The values of 5.5%, 7.5%, and 11% were chosen based on the maximum percent noise shown in Figures B.1 for each model. Variation in Mach number does have a minor effect on uncertainty due to broadening of the peak at low Mach numbers (high pressure and temperature). The estimated uncertainty with varying Mach number was characterized for the 11% noise case for Mach 0.5, 1, 2, 4, 6, 8, and 10. The highest uncertainty occurred at Mach 0.5, and these conditions were used for the 1%, 5.5%, and 7.5% noise cases to bound the problem by worst-case conditions. The largest uncertainty in the frequency shift, due to random error in the signal, results in an uncertainty of ±10 m/s in velocity magnitude for low SNR regions of the quad-nozzle PD model.

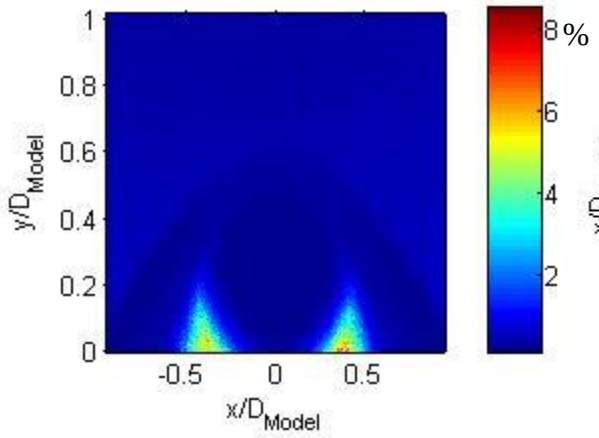

(a) Single-sonic PD Model, 2.3-deg laser sheet angle

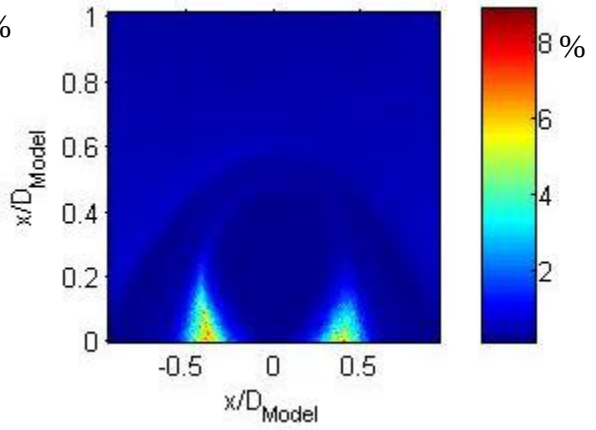

(b) Single-sonic PD Model, 27.8-deg laser sheet angle

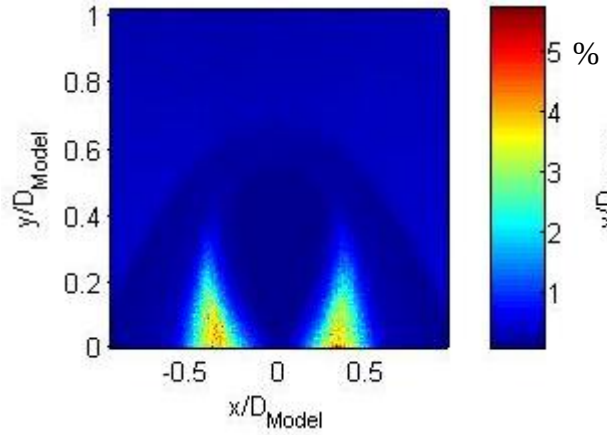

(c) Single-supersonic PD Model, 2.3-deg laser sheet angle

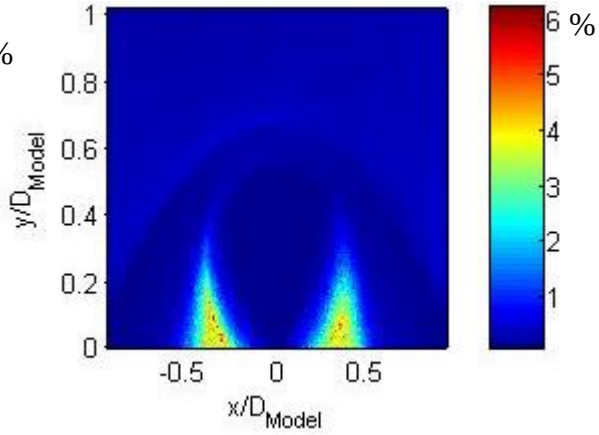

(d) Single-supersonic PD Model, 27.9-deg laser sheet angle

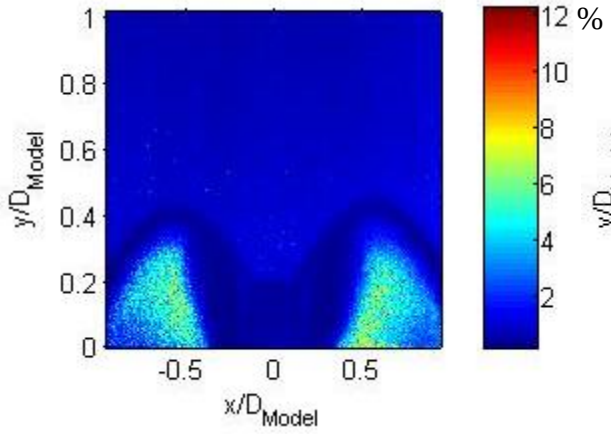

(e) Quad-supersonic PD Model, 1.1-deg laser sheet angle

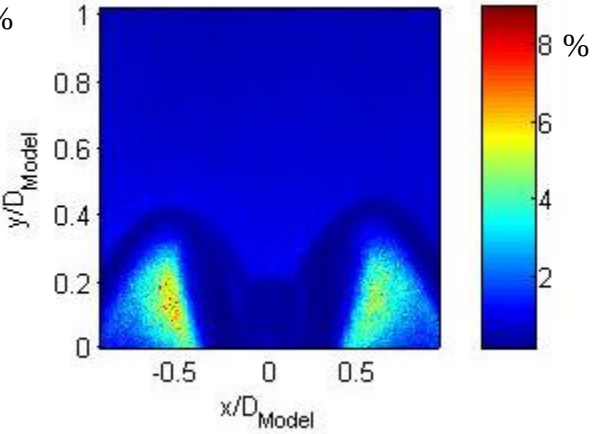

(f) Quad-supersonic PD Model, 24.5-deg laser sheet angle

Figure B.1: Percent noise of total measured signal from absorption spectra

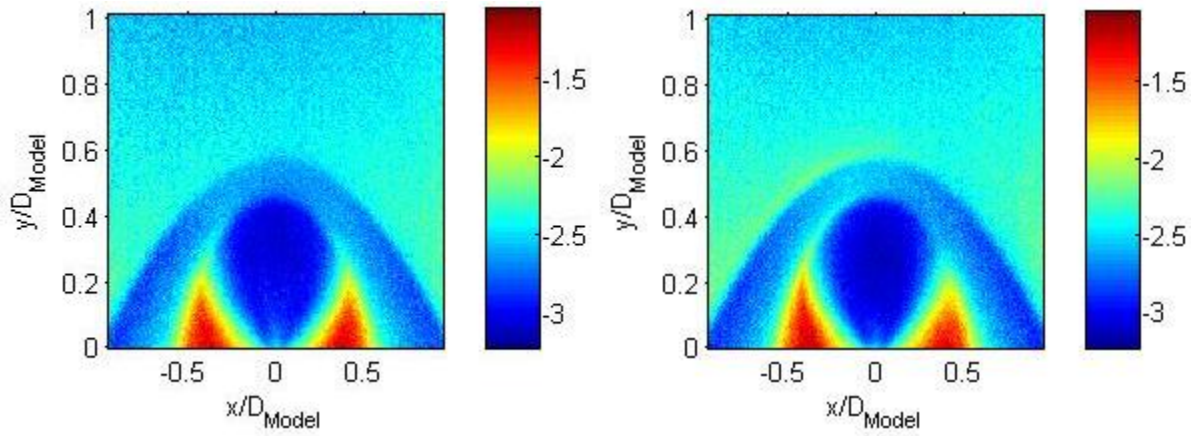

(a) Single-sonic PD Model, 2.3-deg laser sheet angle

(b) Single-sonic PD Model, 27.8-deg laser sheet angle

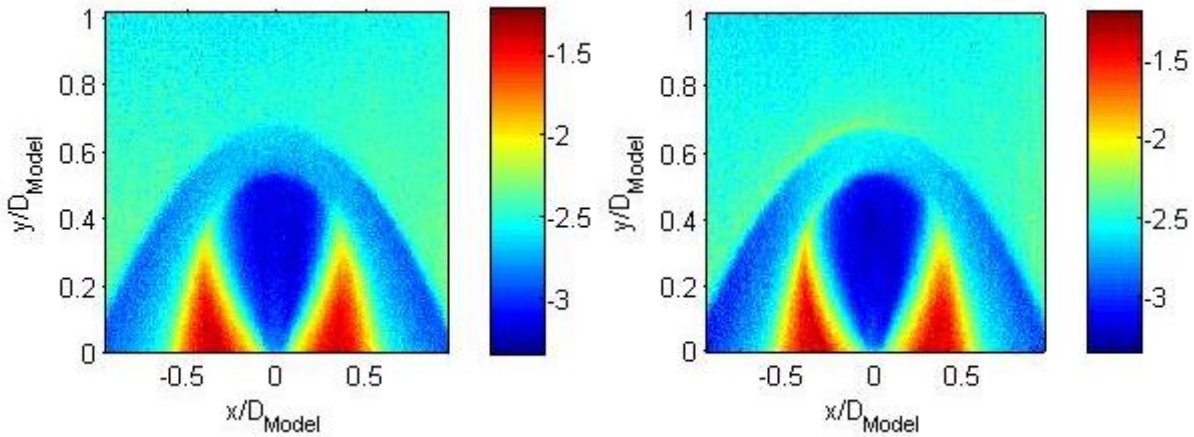

(c) Single-supersonic PD Model, 2.3-deg laser sheet angle

(d) Single-supersonic PD Model, 27.9-deg laser sheet angle

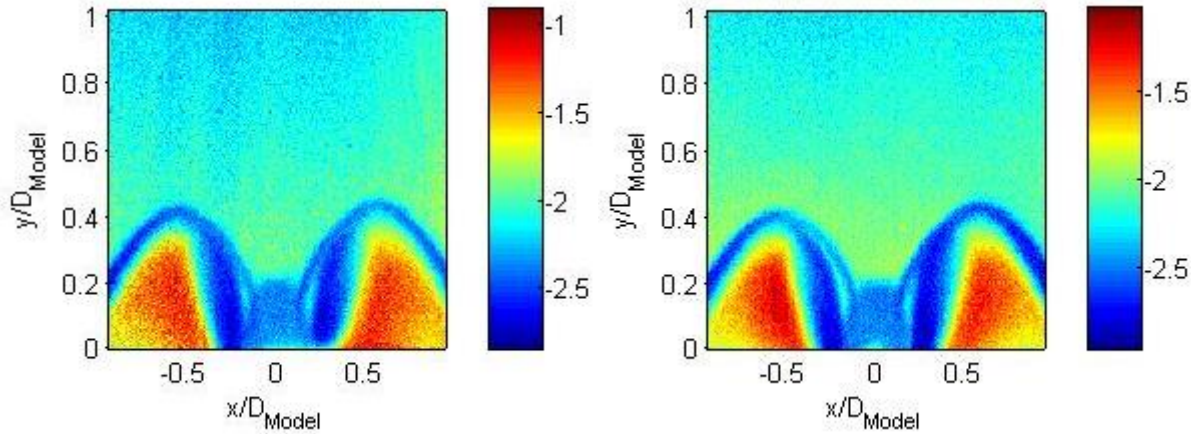

(e) Quad-supersonic PD Model, 1.1-deg laser sheet angle

(f) Quad-supersonic PD Model, 24.5-deg laser sheet angle

Figure B.2: Log plot of percent noise of total measured signal from absorption spectra

Percent Noise	Uncertainty in Measured Frequency Shift [MHz]	Uncertainty in Velocity [m/s]
1.0%	± 1.78	± 0.91
5.5%	± 11.38	± 5.86
7.5%	± 14.13	± 7.27
11.0%	± 19.34	± 9.95

Table B.1: Total velocity uncertainty due to random noise in measured frequency shift

B. Impact Shift

The uncertainty due to cancelling impact shift using symmetry of the flowfield is difficult to quantify. While the assumption of a symmetric flowfield was shown to be a very good assumption from the Doppler-free visualizations in Chapters 5, 6, and 7, in reality no flowfield is perfectly symmetric due to random variation in the measurement technique, such as pixel-to-pixel noise. Furthermore, there is some error associated with identifying the flowfield line of symmetry. The measurement technique is limited by information collected at each individual CCD pixel, and while the resolution is very good (each pixel corresponds to a section of flowfield equal to a square with sides of 64 micrometers) the line of symmetry must be considered to be a single pixel row, or located between two discrete pixels. If columns of camera pixels are at a slight angle to the line of symmetry, then it is also possible for the line of symmetry to pass through multiple adjacent horizontal CCD pixels as the line of symmetry moves vertically upstream of the model centerline. This error is minimized through careful alignment of the camera and model, but still must be considered. For this work, the line of symmetry was assumed to occur between two pixels, i.e. at the edge of each pixel boundary, and the model is centerline is assumed to be coincident with columns of the CCD camera pixels.

It was attempted to quantify the uncertainty associated with "perturbing" the location of the line of symmetry, essentially choosing different columns of pixels for the line of symmetry to occur between, to resolve the effect on computed velocity. However, as expected from Figures 5.6 and 5.7, when the centerline location was varied by 1-3 pixels, the overall effect on flowfield velocity magnitude was less than 3% difference throughout the freestream, PD jet core, and areas outside of the PD jet core/freestream. The greatest percent difference occurred at the PD jet boundary, approaching 40% difference for a range of 2-3 pixels. This area is affected the most by error in the centerline location because the gradient in thermodynamic properties is the greatest in the PD jet shear layer. So mis-identification of the centerline means symmetry points in these large-gradient areas will correspond to a pixel with very little impact shift, which will be outside the PD jet shear layer, and the corresponding symmetry point being inside the PD jet shear layer with large impact shift. While error in the line of symmetry does result in relatively large uncertainty in small, localized regions of the flowfield (PD jet shear layer), the uncertainty in velocity for the majority of the flowfield is considered to be negligible.

C. Laser Sheet Angle

During an experiment a portion of the laser sheet is blocked, causing a dark region in the flow where there is no fluorescence, and multiple images are taken for each laser sheet angle. Edge detection software in Matlab is then used, with the Canny algorithm, and the laser sheet angle is measured along the detected edge. This process is repeated for several images and an uncertainty is calculated for each laser sheet angle. The uncertainty in laser sheet propagation angle is then used to calculate the maximum total uncertainty for each velocity component in the lab frame. The resulting uncertainty for each component of velocity and model test case is shown in Table B.2.

Model	Uncertainty in V_x [m/s]	Uncertainty in V_y [m/s]
Single-Sonic PD	± 5.9	± 2.7
Single-Supersonic PD	± 10.6	± 5.3
Quad-Supersonic PD	±6.4	±1.0

Table B.2: Uncertainty in velocity component (lab frame) for each model tested

D. Total Velocity Uncertainty

Because two laser sheet angles are necessary to measure each velocity component, the total uncertainty is given by the uncertainty in each velocity component due to uncertainty in the laser sheet angle, and uncertainty due to random noise in the measured spectra for each laser sheet angle. The total velocity uncertainty is given by:

$$S_V = \sqrt{S_{shift\,1}^2 + S_{shift\,2}^2 + S_{comp\,1}^2 + S_{comp\,2}^2}$$

where S_V is the total velocity uncertainty, $S_{shift\ 1}$and $S_{shift\ 2}$ correspond to the uncertainty due to random error in fitting the spectra for each component of velocity, and $S_{comp\ 1}$, $S_{comp\ 2}$ are the uncertainties for each velocity component. The overall uncertainty in velocity measurements is shown in Table B.3. In general, the 1% noise is applicable to the freestream, model bow shock, PD jet core, and regions between the PD jet terminal shock and model bow shock (for the quad-nozzle model). Areas with high percent noise correspond areas of the flow with low SNR, and are from the maximum calculated percent noise. For instance, for the single-nozzle PD jet models, the 7.5% and 5.5% noise results apply to regions outside the PD jet shear layer, near the model surface, for the single-nozzle PD jet models (shown in Figures B.1 & B.2). The largest percent noise applies to the quad-supersonic PD model in the region outside of the PD jet shear layer and downstream of the model bow shock.

Model	% Noise	S_V [m/s]
Single-Sonic PD	1.0%	± 6.6
	7.5%	± 12.2
Single-Supersonic PD	1.0%	± 11.9
	5.5%	± 14.5
Quad-Supersonic PD	1.0%	± 6.6
	11.0%	± 15.5

Table B.3: Total experimental uncertainty in velocity for each experimental model. Areas corresponding to different percent noise are shown in Figure B.1

B.2 Temperature Uncertainty Analysis

Because the temperature is computed from the inviscid energy equation, equation 5.3, the experimental uncertainty is related to the total uncertainty in the velocity measurement. The total experimental uncertainty for temperature is given by the following Equation:

$$S_{Temp} = \left(\frac{dT}{dV}\right) S_V = \left(\frac{1}{c_p}|V|\right) S_V$$

where S_{Temp} is the uncertainty in temperature and c_p is the specific heat at constant pressure for nitrogen. The corresponding uncertainty for temperature is given in Table B.4 for various areas of the flow according to a percent error, as discussed in section B.1. Note that this uncertainty analysis does not account for portions of the flowfield where viscous effects are significant; in these regions of the flowfield, as discussed in Chapters 5, 6, and 7, temperatures computed from the inviscid energy equation are only qualitative.

Model	% Noise	S_T [K]
Single-Sonic PD	1%	± 5.0
	7.50%	± 9.3
Single-Supersonic PD	1%	± 9.1
	5.50%	± 11.1
Quad-Supersonic PD	1%	± 5.0
	11%	± 11.8

Table B.4: Total experimental uncertainty in temperature computed from inviscid energy equation. Areas corresponding to different percent noise are shown in Figure B.1

APPENDIX C: DATA ANALYSIS PROGRAMS

C.1. Iodine fluorescence model

```
%Hyperfine model, modified from David Stack's work to incormporate changes
%made by Eric Cecil in imodelfit.c
    % -- Josh Codoni 5/16/2011
function [Sf, Jacobian] = HyperfitJacobian5(arg1, arg2)
% Accepts an argument that is the input frequencies (mustbe a vector of
length >= 6)
% Accepts an argument that is [temperature, pressure, shift, exposure,
background]
% Arguments can be in any order. The parameter arguement may be a 2, 3, 4,or
5 vector.
% Kelvin, Atmospheres, GHz; the Sf has no units
% Sf: a column vector of Fluorescence
% Jacobian: matrix dSf_dparam, where param = [temp, pres, shift, expo, bgrnd]
%Impact shift is taken out of model
%Background is removed
%Output Sf is normalized to simplify fits to absorption spectra

if length(arg1) <= 5 % called as (param, freq)
    nmax = length(arg2);
    temp = arg1(1);
    pres = arg1(2);
    if length(arg1) > 2, shift = arg1(3); else shift = 0; end;
% %     if length(arg1) > 3, exposure = arg1(4); else exposure = 1; end;
% %     if length(arg1) > 4, background = arg1(5); else background = 0; end;
    Frequency = reshape(arg2, [nmax,1]) - shift;
else % called as (freq, param)
    nmax = length(arg1);
    temp = arg2(1);
    pres = arg2(2);
    if length(arg2) > 2, shift = arg2(3); else shift = 0; end;
%   if length(arg2) > 3, exposure = arg2(4); else exposure = 1; end;
%   if length(arg2) > 4, background = arg2(5); else background = 0; end;
    Frequency = reshape(arg1, [nmax,1]) - shift;
end

% CONSTANTS USED
Cq = 1.5;                    % Cq / A21 Hartfield Value K ^ 0.5/kPa --
Donohue used 2.1 as did Stack
Cq = Cq .* 101.3;            % Cq -> atm
Cb = 4.1962.*101.3;                % ?? 4.4 ?? GHz K ^ 0.7 / KPa Donohue
value (from Cecil)
% dhfw  not used by Eric, he includes derivitives of Voigt and dnuL / dnuG
%dhfw = .0075;
% Cimpact = .39;
% Cimpact = Cimpact .* 101.3;   % for atm

% Einstein spontaneous emission coef vs V", normalized by the same for V" =
% 43 (i.e. P13/R15). This is Jim Donohue's 4th order polynomial (?1) fit to
% fig. 8 of paper by Capelle & Broida. Considering the scatter of data,
% this all is questionable. Needless to say, his a's are not meaningful to
% 13 significant figures -- so only using float (approx 7 sig figs). If the
```

```
% quenching is tiny, this won't figure into things.
    % - Eric Cecil


%Einstein spontaneous emmision coef vs V" , approximate curve from Lehman
a0 =  4.381977209869E+00;
a1 = -1.587067053876E-01;
a2 =  2.840871548044E-03;
a3 = -2.832453672502E-05;
a4 =  1.280451088469E-07;

% READ DATA ON TRANSITIONS
    % In the old model FCF, HLF, were calculated but it
    % is simpler to use the data in the file

    % Changed the file to read Eric's hyperfine data transition sheet,
    % added dnuL and dnuG dependencies.
        % - Josh Codoni
TRANSDATA = textread('hfmodel_1storderNEQ_ms.txt','%f','headerlines',1);
TRANSDATA=reshape(TRANSDATA,9,length(TRANSDATA)/9);
J = TRANSDATA(1,:);
JP = TRANSDATA(2,:);
V = TRANSDATA(3,:);
VP = TRANSDATA(4,:);
FrequencyOfTransition = TRANSDATA(5,:); %NUT
HyperFineDegeneracy = TRANSDATA(6,:); %GHF
FrankCondonFactor = TRANSDATA(7,:); %FCF
dnunL = 0.0075;
dnunG = 0.0;

ntrans = length(V);

% Calculate HonlLondonFactor
HonlLondonFactor = 0.5*(J+JP+1.0)./(2.0*J+1.0);

% Changed 214.5 to 213.887 and 0.61 blah to 0.6147 for theta_v- J.Codoni
thetav = (213.887 - .6147*V)/.69505;                                    %
Characteristic vib. temperature
thetar = (.037372 - 1.138E-4*(V+.5))/.69505;                            %
Characteristic rot. temperature

Ev=V.*thetav;
Er=J.*(J+1).*thetar;

% constant used in computing SternVolmerFactor --Luther
SternVolmerHelper = a0 + VP.*(a1 + VP.*(a2 + VP.*(a3 + a4*VP)));

% CALCULATE IMAPACT SHIFT AND DERIVATIVES (scalars)
% dnui = Cimpact*pres/(temp^0.7);
% ddnui_dt = 0.7*Cimpact*pres/(temp.^(1.7));
% ddnui_dp = Cimpact/(temp^(0.7));

% CALCULATING BROADENING PARAMETERS (scalars)
% Note: Eric changes 0.0256 to 0.0262
ddnud_dt = 0.5*0.0262/(temp^(0.5));
ddnuc_dt = -0.7*Cb.*pres/(temp^(1.7));
ddnuc_dp = Cb/(temp^(0.7));
```

```
% CALCULATING QUENCHING PARAMETERS (scalars)
Qair = Cq * pres/temp^0.5;
dQdt = -0.5*Cq*pres/(temp^1.5); % in imodelfit.c was ^1.5; in TwoPeakModel.m
was ^0.5
dQdp = Cq/(temp^0.5);

% Jmax = (sqrt(temp/(2.*.05391))-0.5) +.5;
    %Commented out by E. Cecil

Sf = zeros(size(Frequency));
dSfdt = zeros(size(Frequency));
dSfdp = zeros(size(Frequency));
dSfdf = zeros(size(Frequency));


% Calculate Boltzman Population Fraction
etv_t = exp(-thetav/temp);
Zr = temp./(2*thetar);                                  % Rot. partition
func.
Zv = 1./(1-etv_t);                                      % Vib. Partition
func.
%    Zv=1.0;                                            % Vib. Partition
func.
%    for m = 1:11
%       Zv=Zv+exp(-(m*(214.5 - .613*m)/.69505)/temp);
%    end
% Note that the characteristic temps are defined by Vincenti &
% Kruger for the harmonic oscillator and rigid rotator models, not the
% anharmonic oscillator and vibrating rotator which give the energies shown
% above! Confusing, huh? Have no bothered to rectify this way of doing
% things yet. Should just figure the term energies and not bother with
% characteristic temps. - Eric

%    for m = 1:11
%       Zv=Zv+exp(-(m*(214.5 - .613*m)/.69505)/temp);
%    end
%Donohue uses the above calculation for Zv I don't know why the results
%from using the computation below are nearly identical the only effect
%would be if you were looking at transitions which had V > 0. -- David
%Staack
%Answer: Donohue calc. above is more "correct" and applies to anharmonic
%oscillator. But application here is v" = 0 (or maybe 1) so using analytic
%result for the partition function of the harmonic oscillator like this is
%ok. 214.5 is a mistake, though, but close enough not to matter. - Eric

%Boltzmann pop. fraction
eEv_t = exp(-Ev/temp); % just a temporary to save expensive exponentiations
eEr_t = exp(-Er/temp); % just a temporary to save expensive exponentiations

F = HyperFineDegeneracy .* (2*J+1).* eEv_t .* eEr_t ./ (Zr.*Zv);

dZrdt = 0.5./thetar;
dZvdt = etv_t.*thetav ./ (temp^2*(1-etv_t).^2);
dFdt = (2*J+1) .* HyperFineDegeneracy .* eEv_t .* eEr_t .* (...
    (Ev + Er) ./ (temp^2 * Zv .* Zr) ...
    - dZvdt ./ (Zv.^2 .* Zr) ...
```

```
    - dZrdt ./ (Zv .* Zr.^2) ...);

SternVolmerFactor = SternVolmerHelper ./ (SternVolmerHelper + Qair);

%CALCULATE STERN-VOLMER FACTOR
SternVolmerFactor = SternVolmerHelper./(SternVolmerHelper + Qair);
dSVFdt = -SternVolmerFactor./(SternVolmerHelper+Qair)*dQdt;
dSVFdp = -SternVolmerFactor./(SternVolmerHelper+Qair)*dQdp;

% Doppler + pseudo-natural (Gaussian) line width at half max
% (Latter is used to account for hyperfine splitting of a line when full
% hyperfine detail is not needed due to broadening.)
dnud = 0.0262*sqrt(temp)+dnunG;
   %Collision + natural (Lorentzian) line width at half max
dnuc = Cb*pres/(temp^0.7)+dnunL;

B = sqrt(log(2))*dnuc/dnud;          % Note, sl2 = sqrt(ln(2)) from Eric's
code
dBdt = sqrt(log(2))*(ddnuc_dt/dnud - dnuc*ddnud_dt/(dnud^2));
dBdp = sqrt(log(2))*ddnuc_dp/dnud;

% Move Transition Locations by impact shift
FrequencyOfTransition = FrequencyOfTransition;

SftConst = HonlLondonFactor .* FrankCondonFactor .* SternVolmerFactor .* F *
(pres/temp);

for i = 1:ntrans

    dnu = abs(Frequency-FrequencyOfTransition(i));

    D = 2*sqrt(log(2))*dnu/dnud;                          % Detuning
parameter

    % Calculate Voigt function & its derivatives, Y = Humdev(x,y)
    % Note: used D, B, and Y to match Eric's notation. These correspond
    % to x, y, and k in the Humdev.m code. Will correct this
    % later to match previous notation and reduce confusion. - Josh
    [Y, L, dYdD, dYdB] = Humdev2(D, B);
    % We appear to ignore L, the imaginary part. --Luther

    Sft = Y .* (SftConst(i) / dnud);     % Transition of Fluorescence
intensity
    Sf = Sf + Sft;


end

Sf = Sf;
Sf = Sf ./ max(Sf);
% Sf = Sf2 / max(Sf2) + background;

% if nargout > 1 % compute the Jacobian on demand
%   % given y = Sf(i)
%   % dSfdt
%   % dSfdp
%   % dSfdshift = dSfdf
```

```
%   % dSfdexposure = Sf
%   % dSfdbackground = 1
% %     Jacobian = [dSfdt*exposure, dSfdp*exposure, -dSfdf*exposure,
Sf/exposure, ones(nmax,1)];
% end
```

C.2. Voigt Function

```
function [ k, L, dkdx, dkdy ] = Humdev2( x, y )
%HUMDEV  Calculates the Faddeeva function and derivatives of the Voigt
%function for y >= 0
%   Based on HUMDEV.C from Eric Cecil, his was a slightly modified code
%   for the standard boxed Fortran 77 code called HUMDEV.for, which can
%   be found here: http://www.atm.ox.ac.uk/user/wells/humdev.for
%       Adapted by Josh Codoni, 5/12/2011

%   k is the Voigt function,
%   L is the imaginary part
%   dk/dx is the partial derivative of the Voigt function
%   dk/dy is the partial derivative of the Voigt function
%   n is the number of points
%   x is the input array in the x-dir
%   y is the scalar input in the y-dir (y >= 0)
%   All outputs are column vectors

% Edited by 20 Jun 2011 to accept x and y as vectors, have no loops,
% and only compute k. The goal of this edit was speed. --Luther Tychonievich

% ensure x is a column vector
n = length(x);
sx = size(x);
if sx(2) > 1
    if sx(1) > 1
        error('Expected a column vector, not x of size (%d, %d)', size(x));
    end
    x = reshape(x, [n, 1]);
end


%Assigning Constants
y0 = 1.5;
y0py0 = y0+y0;
y0q = y0.*y0;
drtpi = double(1/sqrt(pi));
c(1:6) = [1.0117281,-0.75197147,0.012557727,0.010022008,-
0.00024206814,0.00000050084806];
s(1:6) = [1.393237,0.23115241,-0.15535147,0.0062183662,0.000091908299,-
0.00000062752596];
t(1:6) = [0.31424038,0.94778839,1.5976826,2.2795071,3.0206370,3.8897249];

%Start of code
rgb =1;
rgc =1;
rgd =1;
```

```
yq = y*y;


%   Region A boundary
xlima = 146.7 - y;
%   Region B boundary
xlimb = 24.0 - y;
%   Region C boundary
xlimc = 7.4 - y;
%   CPF12 I-II boundary
xlim4 = 18.1 .* y + 1.65;

%Loop over all points, taken out for now. When compared to values listed
%in R.J. Wells 1999 paper, Reference #21 in Eric Cecil's Master's thesis,
%in the table (page 40), results would match for x1,y1, x2,y2, x4,y4 values
%but produced strange results for x3,y3 values. Will attempt to correct
%later.

% replaced all loops with matrix operations. 20/Jun/2011 --Luther

abx = abs(x);                                                    % |x|
xq = abx.^2;                                                     % x^2
if (abx > xlima),                                                % Region A
    d = 1.0 ./ (xq + yq);
    d1 = d * drtpi;
    k = d1 .* y;
    L = d1 .* x;
    d1 = d1 .* d;
    dkdx = -d1 .* (y+y) .* x;
    dkdy = d1 .* (xq - yq);
elseif (abx > xlimb),                                            % Region B
    a0 = yq + 0.5;                                               % Region A y-
dependents
    b1 = yq - 0.5;
    d0 = a0 .* a0;                                               % y^4 + y^2 + 0.25
    d2 = b1 + b1;                                                % 2y^2 - 1
    c0 = 1.5 + yq .* (1.0 - d2);                                 % 1.5 + 2y^2 - 2y^4
    c2 = a0 + a0;                                                % 2y^2 + 1
    r0 = 0.125 + yq .* (0.25 - yq .* (0.5 + yq));
    r2 = 0.25 + yq .* (5.0 + yq);
    d = 1.0 ./ (d0 + xq .* (d2 + xq));
    d1 = drtpi .* d;
    k = d1 .* (a0 + xq) .* y;
    L = d1 .* (b1 + xq) .* x;
    d1 = d1 .* d;
    dkdx = d1 .* x .* y .* (c0 - (c2 + xq) .* (xq + xq));
    dkdy = d1 .* (r0 - xq .* (r2 - xq .* (b1 + xq)));
elseif (abx > xlimc),                                            % Region C
    h0 = 0.5625+yq.*(4.5+yq.*(10.5+yq.*(6.0+yq)));               % Region B y-
dependents
    h2 = -4.5 + yq .* (9.0 + yq .*(6.0 + yq .* 4.0));
    h4 = 10.5 - yq .* (6.0 - yq * 6.0);
    h6 = - 6.0 + yq * 4.0;
    e0 = y .* (1.875 + yq .* (8.25 + yq .* (5.5 +yq)));
    e2 = y .* (5.25 + yq .* (1.0 + yq * 3.0));
    e4 = y * 0.75 .* h6;
    w0 = 1.875 + yq .* (24.25 + yq .* (27.5 + yq * 7.0));
```

```
    w2 = 5.25 + yq .* (3.0 + yq * 15.0);
    w4 = -4.5 + yq * 9.0;
    f1 = -1.875 + yq .* (5.25 + yq .* (4.5 + yq));
    f3 = 8.25 - yq .* (1.0 - yq * 3.0);
    f5 = -5.5 + yq * 3.0;
    g0 = y .* (9.0 + yq .* (42.0 + yq .* (36.0 + yq * 8.0)));
    g2 = y .* (18.0 + yq .* (24.0 + yq * 24.0));
    g4 = y .* (-12.0 + yq * 24.0);
    g6 = y * 8.0;
    u = e0 + xq .* (e2 + xq .* (e4 + xq .* y));
    d = 1.0 ./ (h0 + xq .* (h2 + xq .* (h4 + xq .* (h6 + xq))));
    k = drtpi .* d .* u;
    L = drtpi .* d .* x .* (f1 + xq .* (f3 + xq .* (f5 + xq)));
    dudy = w0 + xq .* (w2 + xq .* (w4 + xq));
    dvdy = g0 + xq .* (g2 + xq .* (g4 + xq .* g6));
    dkdy = drtpi .* d .* (dudy - d .* u .* dvdy);
elseif (abx < 0.85),                                    % Region D
    z0 = 272.1014+y.*(1280.829+y.*(2802.870+y.*(3764.966+y...       % Region
C dependents
        .*(3447.629+y.*(2256.981+y.*(1074.409+y.*(369.1989+y...
        .*(88.26741+y.*(13.3988+y)))))))));
    z2 = 211.678 + y .* (902.3066 + y .* (1758.336 + y .*...
        (2037.310 + y .* (1549.675 + y .* (793.4273 + y .*...
        (266.2987 + y .* (53.59518 + y .* 5.0)))))));
    z4 = 78.86585 + y .* (308.1852 + y .* (497.3014 + y .*...
        (479.2576 + y .* (269.2916 + y .* (80.39278 + y...
        .* 10.0)))));
    z6 = 22.03523 + y .* (55.02933 + y .* (92.75679 + y .* ...
        (53.5918 + y .* (10.0))));
    z8 = 1.496460 + y .* (13.39880 + y .* 5.0);
    p0 = 153.5168 + y .* (549.3954 + y .* (919.4955 + y .*...
        (946.897 + y .* (662.8097 + y .* (328.2151 + y .* ...
        (115.3772 + y .* (27.93941 + y .* (4.264678 + y .*...
        0.3183291)))))));
    p2 = -34.16955 + y .* (-1.322256 + y .* (124.5975 + y .*...
        (189.773 + y .* (139.4665 + y .* (56.81652 + y .* ...
        (12.79458 + y .* 1.2733163))))));
    p4 = 2.584042 + y .* (10.46332 + y .* (24.01655 + y .* ...
        (29.81482 + y .* (12.79568 + y .* 1.9099744))));
    p6 = -0.07272979 + y .* (0.9377051 + y .* (4.266322 + y .*...
        1.273316));
    p8 = 0.0005480304 + y .* 0.3183291;
    q1 = 173.2355 + y .* (508.2585 + y .* (685.8378 + y .* ...
        (557.5178 + y .* (301.3208  + y .* (111.0528 + y .* ...
        (27.6294 + y .*(4.26413 + y .* 0.3183291)))))));
    q3 = 18.97431 + y .* (100.7375 + y .* (160.4013 + y .* ...
        (130.8905 + y .* (55.88650 + y .*(12.79239 + y .*...
        1.273316)))));
    q5 = 7.985877 + y .*(19.83766 + y .*(28.88480 + y .* ...
        (12.79239 + y .* 1.909974)));
    q7 = 0.6276985 + y .*(4.26413 + y .* 1.273316);
     u = 1.7724538 .* (p0 + xq .* (p2 + xq .* (p4 + xq .* ...
         (p6 + xq .* p8))));
     d = 1.0 ./ (z0 + xq .* (z2 + xq .* (z4 + xq .* ...
         (z6 + xq .* (z8 + xq)))));
     k = d .* u;
     L = 1.7724538 .* d .* x .* (q1 + xq .* (q3 + xq .* (q5 + xq .* ...
```

```
         (q7 + xq .* 0.3183291))));
     db = x .* L + y .* k - drtpi;
     dkdy = db +db;
else                                                                    % Use
CPF12
    ypy0 = y + y0;
    ypy0q = ypy0.^2;
    mt = x*ones(1,6) - ones(n,1)*t;
    pt = x*ones(1,6) + ones(n,1)*t;
    mq = mt.^2;
    pq = pt.^2;
    mf = 1.0 ./ (mq + ypy0q);
    pf = 1.0 ./ (pq + ypy0q);
    xm = mf.*mt;
    ym = mf.*ypy0;
    xp = pf.*pt;
    yp = pf.*ypy0;

    L = (xm+xp)*c' + (ym-yp)*s';
    if (abx <= xlim4),                                  % Humlicek CPF12 Region
I
        yf1 = ypy0 + ypy0;
        yf2 = ypy0q + ypy0q;
        dkdy = 0.0;
        mfq = mf.^2;
        pfq = pf.^2;
        k = (ym+yp)*c' - (xm-xp)*s';
        dkdy = (mf+pf-yf2*(mfq+pfq))*c' + yf1*(mt.*mfq-pt.*pfq)*s';
    else                                                % Humlicek CPF12 Region
II
        yp2y0 = y + y0py0;
        cl = ones(n,1)*c;
        sl = ones(n,1)*s;
        k = (cl.*(mq.*mf-y0.*ym) + sl.*yp2y0.*xm) ./ (mq+y0q) ...
          + (cl.*(pq.*pf-y0.*yp) - sl.*yp2y0.*xp) ./ (pq+y0q);
        k = k*ones(6,1);
        k = y.*k + exp(-xq);
        db = x.*L + y.*k-drtpi;
        dkdy = db*2;
    end
end
db = y.*L - x.*k;
dkdx = 2*db;
```

C.3. Least-squares fitting routine

```
function [] = getTotalShift3( irange, jrange )
%Attempt at resolving frequency shift for velocity measurements
%No impact shift considered (removed from HyperfitJacobian).

%Input ydata must be in the form of a m x n x frequency matrix, ie m and n
%correspond to physical x and y components of a fluorescence image, the
%depth is frequency steps.
% J.Codoni 12/27/12
```

```
%b0 is the initial guess
%ub is the upper bound
%lb is the lower bound
%irange and jrange are the horizontal and vertical ranges, respectively.
%ex data_irange_jrange
%staticnorm is the normalized static cell measurement (normalize to max
%signal level)
%xdata is the frequency vector
%ydata is a i x j x k matrix where i and j are physical camera pixel
locations
%and k is the spectral data
%TandP is the pressure and temperature, will be saved in a mxnx2 matrix
%with the m, n, 1 corresponding to Temperature, the m, n, 2 corresponding
%to pressure

max_iteration = 1;
InitialGuesses = 25;

load xdata.mat
load ydata.mat
load staticnorm.mat

[l1, l2, ~] = size(ydata);

imin = min(irange);
imax = max(irange);
jmin = min(jrange);
jmax = max(jrange);

LL =
exist(sprintf('FreqI_%d_to_%d_J_%d_to_%d.mat',imin,imax,jmin,jmax),'file');
if LL == 2
    fprintf('Freq.mat exists\n')
    load(sprintf('FreqI_%d_to_%d_J_%d_to_%d.mat',imin,imax,jmin,jmax));
    load(sprintf('ShiftI_%d_to_%d_J_%d_to_%d.mat',imin,imax,jmin,jmax));
    load(sprintf('PressI_%d_to_%d_J_%d_to_%d.mat',imin,imax,jmin,jmax));
    load(sprintf('TempI_%d_to_%d_J_%d_to_%d.mat',imin,imax,jmin,jmax));
else
    fprintf('Freq.mat does not exist\n')
    freq = zeros(l1, l2);
    shift = zeros(l1, l2);
    Temp = zeros(l1, l2);
    Press = zeros(l1, l2);
end

b0 = [150 3e-2 0];
lb = [9 1e-15 -2];
ub = [300 2e-2 2];

%close all
%tic
ms = MultiStart;
problem1 =
createOptimProblem('lsqcurvefit','objective',@HyperfitJacobian5,'xdata',xdata
,'ydata',staticnorm,'x0',b0,'lb',lb,'ub',ub);
[b,~,~,~,~] = run(ms,problem1,10);
```

```
freq0 = b(3);

spectral_range=length(xdata);

flowdata = zeros(1,spectral_range);

Residual = zeros(l1,l2);

for i = irange
    for j = jrange

        if freq(i,j) == 0 || freq(i,j) == 999
            fprintf('freq in is %f\n, i is %d, j is %d',freq(i,j),i,j)

%            flowdata=zeros(1,spectral_range);

            flowdata(1,:) = ydata(i,j,1:1:spectral_range)-
ydata(i,j,spectral_range+1);

            flowdata=flowdata./max(flowdata);
            problem2 =
createOptimProblem('lsqcurvefit','objective',@HyperfitJacobian5,'xdata',xdata
,'ydata',flowdata','x0',b0,'lb',lb,'ub',ub);
            [b2,~,~,~,solution2] = run(ms,problem2,InitialGuesses);

            fval = solution2(1,1).Fval;

            fprintf('fval is %f\n',fval)

            iteration = 0;
            while iteration < max_iteration && fval > 2.5

                iteration = iteration +1;

                [b2,~,~,~,solution2] = run(ms,problem2,InitialGuesses);
                fval = solution2(1,1).Fval;
            end


            while iteration < 2*max_iteration && fval > 4.5
                iteration = iteration +1;
                [b2,~,~,~,solution2] = run(ms,problem2,InitialGuesses);
                fval = solution2(1,1).Fval;
            end

            while iteration < 3*max_iteration && fval > 20.5
                iteration = iteration +1;
                [b2,~,~,~,solution2] = run(ms,problem2,InitialGuesses);
                fval = solution2(1,1).Fval;
            end

            fprintf('Fval is %04f\n and Iteration is %d\n',fval,iteration);

            freq(i,j) = b2(3);
            shift(i,j) = freq0 - freq(i,j);
            Residual(i,j) = fval;
```

```
            if iteration == 3*max_iteration && fval > 20.5
                shift(i,j) = 999;
            end

            %toc

            Press(i,j) = b2(2);
            Temp(i,j) = b2(1);

            figure(1)
            hold off
            trial = HyperfitJacobian5(b2,xdata);
            plot(xdata,trial,'-r');
            hold on
            plot(xdata,flowdata,'-b');
            h=gcf;
%         saveas(h,sprintf('C:\\Users\\jrc8db\\Desktop\\Single Sonic PD jet
Velocity\\Vertical Angle\\Coarse Data Large\\Large Analysis, full\\fig
spectra fits\\fit_%d_%d.fig',i,j),'fig');
%         saveas(h,sprintf('C:\\Users\\jrc8db\\Desktop\\Single Sonic PD jet
Velocity\\Vertical Angle\\Coarse Data Large\\Large Analysis, full\\jpg
spectra fits\\fit_%d_%d.jpg',i,j),'jpg');
            saveas(h,sprintf('./fit_%d_%d.fig',i,j),'fig');
            saveas(h,sprintf('./fit_%d_%d.jpg',i,j),'jpg');

            close all

            minimum_j = min(jrange);
            maximum_j = max(jrange);
            minimum_i = min(irange);
            maximum_i = max(irange);


save(sprintf('FreqI_%d_to_%d_J_%d_to_%d.mat',minimum_i,maximum_i,minimum_j,ma
ximum_j),'freq');

save(sprintf('ShiftI_%d_to_%d_J_%d_to_%d.mat',minimum_i,maximum_i,minimum_j,m
aximum_j),'shift');

save(sprintf('TempI_%d_to_%d_J_%d_to_%d.mat',minimum_i,maximum_i,minimum_j,ma
ximum_j),'Temp');

save(sprintf('PressI_%d_to_%d_J_%d_to_%d.mat',minimum_i,maximum_i,minimum_j,m
aximum_j),'Press');

save(sprintf('ResidualI_%d_to_%d_J_%d_to_%d.mat',minimum_i,maximum_i,minimum_
j,maximum_j),'Residual');
        end
    end
end

% clear all
% close all
% clc

end
```

C.4. UVa cluster analysis files

C.4.1 Sampe_space.m

```
%%%%%%% sample_space.m

% Creates the meshgrid sample space used to parellize code between cluster
% nodes.

% n_half_x is half the total horizontal distance, 180 pixels in this case.
% n_tot_y is the total vertical distance, 160 pixels in this case.

% Because my flowfield is symmetric about the horizontal, the xm is split
% into two sections and marched 180 pixels out to either side.

% x0 and y0 correspond to point where the solution starts and marches out
% from. Note, these are pixel locations in the 600x400 solution area my
% dataset is reduced to. In this orientation, my model stagnation point is
% always set to 300, 201. This particular setup will begin 30 pixels below
% my model stagnation point.

%Created by Gaetano Esposito, edited by Josh Codoni 3/10/14

clear all
close all

% Stagnation point on my model, determines where solution begins marching.
xm = 300;

n_half_x = 180;
n_tot_y = 160;

% symmetric around xm
x0 = xm - n_half_x + 1;
xend = xm + n_half_x;
y0 = 171;
yend = y0 + n_tot_y - 1;


% n_sub_x * n_sub_y is equal to number of cluster nodes the job is split
% between. Note, n_half_x * 2 must be divisible by n_sub_x, n_tot_y must
% divisible by n_sub_y.

n_sub_x = 12;
n_sub_y = 10;

if mod( xend-x0+1, n_sub_x ) || mod( yend-y0+1, n_sub_y )
    error('Number of points is not compatible with analysis domain')
end
```

```
% create ranges
irange = x0:xend;
jrange = y0:yend;

% create bounds of sub-domains
deltax = (xend-x0+1)/n_sub_x;
deltay = (yend-y0+1)/n_sub_y;

irange_sub = x0:deltax:x0+(n_sub_x)*deltax;
jrange_sub = y0:deltay:y0+(n_sub_y)*deltay;

[I_RANGE,     J_RANGE]     = meshgrid( irange,     jrange );
[I_RANGE_SUB, J_RANGE_SUB] = meshgrid( irange_sub, jrange_sub );

%The following section can be uncommented, and plot flag changed to 1 to
%show marching solution of meshgrid creation. Also un-comment the pause
%command in the nested for loops.

%figure;
%plot(I_RANGE, J_RANGE, 'ko')
%hold on
%plot(I_RANGE_SUB, J_RANGE_SUB,'rx')
%xlabel('x')
%ylabel('y')

plot_flag = 0;

% -- store ranges in a cell
store_ranges = {n_sub_x*n_sub_y, 2};

for ix = 1 : n_sub_x

    for iy = 1 : n_sub_y

        % -- the structure that comes out of meshgrid is pretty cumbersome
        sub_irange = I_RANGE_SUB(iy, ix):I_RANGE_SUB(iy,ix+1)-1;
        sub_jrange = J_RANGE_SUB(iy, ix):J_RANGE_SUB(iy+1,ix)-1;

        store_ranges{(ix-1)*n_sub_y + iy, 1} = sub_irange;
        store_ranges{(ix-1)*n_sub_y + iy, 2} = sub_jrange;

        if plot_flag
            [xx, yy] = meshgrid( sub_irange, sub_jrange );

            plot(xx, yy, 'g.')
            %pause(0.0001)
        end

    end

end
```

```
save store_ranges.mat store_ranges n_sub_x n_sub_y

%#getTotalShift(store_ranges{1,1}, store_ranges{1,2})
```

C.4.2 driverTotalShift.m

```
%%%%%%%% driverTotalShift.m

function [] = driverTotalShift( index_string )

%This file runs the data analysis programs on the cluster nodes

%Compile this file to an executable on the cluster using mcc -m -v
driverTotalShift
%in Matlab

%index_string is passed to driverTotalShift from the bash script

index = str2double(index_string);

load store_ranges.mat

fprintf('running index %d\n',index);

irange = store_ranges{ index, 1 };
jrange = store_ranges{ index, 2 };

fprintf('min, max irange = %d %d\n',irange(1),irange(end));
fprintf('min, max jrange = %d %d\n',jrange(1),jrange(end));

getTotalShift3( irange, jrange )

end
```

C.4.3 create_run.bash – sends jobs to cluster nodes

```
#!/bin/bash

n_sub_x=12
n_sub_y=10
n_tot_sub=$((n_sub_x*n_sub_y))

echo "n_sub_x = $n_sub_x"
echo "n_sub_y = $n_sub_y"
echo "n_sub_sub = $n_tot_sub"


root_dir=/bigtmp/jrcodoni
```

```
script_dir=$root_dir/scripts
pbs_scripts_dir=$root_dir/pbs_scripts_supersonic_quad_top
store_dir=$root_dir/results_supersonic_quad_top
store_dir_jpg=$store_dir/jpg
store_dir_mat=$store_dir/mat
store_dir_fig=$store_dir/fig

run_dir_root=$root_dir/run_supersonic_quad_top
source_dir=/home/jrc8db/VelocitySolver/source_supersonic_quad_to
p

# create directory if doesn't exist
if [[ ! -d $script_dir ]]
then
mkdir -pv $script_dir
fi
# create directory if doesn't exist
if [[ ! -d $pbs_scripts_dir ]]
then
mkdir -pv $pbs_scripts_dir
fi
# create directory if doesn't exist
if [[ ! -d $store_dir_jpg ]]
then
mkdir -pv $store_dir_jpg
fi
# create directory if doesn't exist
if [[ ! -d $store_dir_mat ]]
then
mkdir -pv $store_dir_mat
fi
# create directory if doesn't exist
if [[ ! -d $store_dir_fig ]]
then
mkdir -pv $store_dir_fig
fi
# create directory if doesn't exist
if [[ ! -d $run_dir_root ]]
then
mkdir -pv $run_dir_root
fi

# create PBS scripts
for (( i=10; i<=$n_tot_sub; i++ ))
do
     # create directory if doesn't exist
     run_dir=$run_dir_root/$i
```

```
     if [[ ! -d $run_dir ]]
     then
     mkdir -pv $run_dir
     fi

     # copy files
     cp -v $source_dir/driverTotalShift $run_dir
     cp -v $source_dir/run_driverTotalShift.sh $run_dir
     cp -v $source_dir/*.mat $run_dir
     cp -v $source_dir/hfmodel*.txt $run_dir


     filename=$pbs_scripts_dir/pbsjob_$i.pbs

     echo "#!/bin/bash" > $filename
     echo "#PBS -l select=1:ncpus=1" >> $filename
     echo "#PBS -q nopreempt" >> $filename
     echo "#PBS -l walltime=100:00:00" >> $filename
     echo "#PBS -o $pbs_scripts_dir/pbsoutput_$i" >> $filename
     echo "#PBS -j oe" >> $filename
     echo " " >> $filename
     echo "cd $run_dir " >> $filename
     echo "./run_driverTotalShift.sh /common/matlab/R2013a $i "
>> $filename
     echo "cp -v FreqI*.mat $store_dir_mat " >> $filename
     echo "cp -v ShiftI*.mat $store_dir_mat " >> $filename
     echo "cp -v TempI*.mat $store_dir_mat " >> $filename
     echo "cp -v PressI*.mat $store_dir_mat " >> $filename
     echo "cp -v ResidualI*.mat $store_dir_mat " >> $filename
     echo "cp -v *.fig $store_dir_fig " >> $filename
     echo "cp -v *.jpg $store_dir_jpg " >> $filename
     echo " " >> $filename
     echo " " >> $filename

     qsub $filename
done
```

REFERENCES

[1] Braun, R. D., and Manning, R. M., "Mars Exploration Entry, Descent, and Landing Challenges," Journal of Spacecraft and Rockets, Vol. 44, No. 2, 2007, pp. 310–323.

[2] Zang, T. A., and Munk, M. M., et al., "Entry, Descent and Landing Systems Analysis Study: Phase 1 Report," NASA TM 2010-216720, Jul. 2010.

[3] Steinfeldt, B. A., Theisinger, J. E., Korzun, A. M., Clark, I. G., Grant, M. J., and Braun, R. D., "High Mass Mars Entry, Descent, and Landing Architecture Assessment," AIAA Paper 2009-6684, Sept. 2009.
[4] Jarvinen, P. O., and Adams, R. H., "The Aerodynamic Characteristics of Large Angled Cones with Retrorockets," NASA CR NAS 7-576, Feb. 1970.
[5] Keyes, J.W. and Hefner, J.N., "Effect of Forward-Facing Jets on Aerodynamic Characteristics of Blunt Configurations at Mach 6," Journal of Spacecraft and Rockets, Vol. 4, No. 4, 1967, pp. 533-534.
[6] Adler, M., Wright, M., Campbell, C., Clark, I., Engelund, W., Rivellini, T., "Entry, Descent, and Landing Roadmap," NASA TA09, Apr. 2012.
[7] Edquist, K.T., Berry, S.A., Rhode, M.N., Kleb, B., Korzun, A.M., Dyakonov, A.A., Zarchi, K.A., Schauerhamer, D.G., and Post, E.A., "Supersonic Retropropulsion Technology Development in NASA's Entry, Descent, and Landing Project," 9th Internation Planetary Probe Workshop, Tuolouse, France, 18-22 Jun. 2012.
[8] Edquist, K. T., Dyakonov, A. A., Korzun, A. M., Shidner, J. D., Studak, J. W., Tigges, M. A., Kipp, D. M., Prakash, R., Trumble, K. A., Dupzyk, I. C., "Development of Supersonic Retro-Propulsion for Future Mars Entry, Descent, and Landing Systems," AIAA Paper 2010-5046, June 2010.
[9] Korzun, A. M., and Braun, R. D., "Performance Characterization of Supersonic Retropropulsion for High-Mass Mars Entry Systems," Journal of Spacecraft and Rockets, Vol. 47, No. 5, pp. 836-848, 2010.
[10] Berry, S.A., Laws, C.T., Kleb, W.L., Rhode, M.N., Spells, C., Mccrea, A.C., Trumble, K.A., Schauerhamer, D.G., Oberkampf, W.L., "Supersonic Retro-Propulsion Experimental Design for Computational Fluid Dynamics Model Validation," IEEE Aerospace Conference Paper No.1499, Mar. 2011.
[11] Palaszewski, B. and Bencic, T., "Mars Entry, Descent and Landing: Experiments with Multiple Engine Supersonic Retro Propulsion Configuration," AIAA Paper 2010-6594, Joint Propulsion Conference, Nashville, TN, Jul. 2010.
[12] Moeckel, W.E., "Flow Separation Ahead of Blunt Bodies at Supersonic Speeds," NASA TN 2418, National Advisory Committee for Aeronautics, 1951.
[13] Moeckel, W.E., "Flow Separation Ahead of a Blunt Axially Symmetric Body at Mach Numbers 1.76 to 2.10," NASA RM E51I25, 1951.
[14] Love, E.S., and Grigsby, C.E., "Some Studies of Axisymmetric Free Jets Exhausting from Sonic and Supersonic Nozzles into Still Air and into Supersonic Freestreams," NASA RM L54L31, 1955.
[15] Love, E.S., and Grigsby, C.E., Lee, L.P., and Woodling, M.J., "Experimental and Theoretical Studies of Axisymmetric Free Jets," NASA TR R-6, 1959.
[16] Romeo, D., J., and Sterrett, J.R., "Exploratory Investigation of the Effect of a Forward-Facing Jet on the Bow Shock of a Blunt Body in a Mach Number 6 Free Stream," NASA TN D-1605, 1963
[17] McGhee, R.J., "Effects of a Retronozzle Located at the Apex of a 140° Blunt Cone at Mach Numbers of 3.00, 4.50, and 6.00," NASA TN D-6002, 1971.
[18] Jarvinen, P.O., and Adams, R.H., "The Effects of Retrorockets on the Aerodynamic Characteristics of Conical Aeroshell Planetary Entry Vehicle," AIAA Paper 70-219, January 1970.

[19] Drake, B.G., "Reference Mission Version 3.0: Addendum to the Human Exploration of Mars: The Reference Mission of the NASA Mars Exploration Study Team," NASA SP-6107-ADD, June 1998.
[20] Hoffman, S.J., and Kaplan, D.I., "Human Exploration of Mars: The Reference Mission of the NASA Mars Exploration Study Team," NASA Johnson Space Center Rept. SP 6107, July 1997.
[21] Wells, G.W.,Lafleur, J.M.,Verges,A.M.,Manyapu,K., Christian, J.A., Lewis, C., and Braun, R.D., "Entry, Descent, and Landing Challenges of
Human Mars Exploration," American Astronautical Society Paper 06-072, Feb. 2006.
[22] Christian, J. A., Wells, G. W., Lafleur, J. M., Verges, A. M., and Braun, R. D., "Extension of Traditional Entry, Descent, and Landing Technologies for Human Mars Exploration," Journal of Spacecraft and Rockets, Vol. 45, No. 1, 2008, pp. 130–141.
[23]Palaszewski, B., and Bencic, T., "Mars Entry, Descent, and Landing: Supersonic Retro Propulsion Experiments," AIAA Paper 2009-5263, Aug. 2009.
[24] Berry, S.A., Rhode, M.N., Edquist, K.T., and Player, C.J., "Supersonic Retropropulsion Experimental Results from NASA Langley Unitary Plan Wind Tunnel," AIAA Paper 2011-3489, Jun. 2011.
[25] Berry, S.A., Rhode, M.N., Edquist, K.T., "Supersonic Retropropulsion Experimental Results from the NASA Ames 9- x 7-Foot Supersonic Wind Tunnel," AIAA Paper 2012-2704, AIAA Fluid Dynamics Conference, New Orleans, 25-28 Jun. 2012.
[26] Codoni, J.R., and Berry, S.A., "Analysis of Dynamic Data from Supersonic Retropropulsion Experiments in NASA Langley's Unitary Plan Wind Tunnel," AIAA Paper 2012-2706, AIAA Fluid Dynamics Conference, New Orleans, 25-28 Jun. 2012.
[27] Rhode, M.N., and Oberkampf, W., "Estimation of Uncertainties for a Supersonic Retro-Propulsion Model Validation Experiment in a Wind Tunnel," AIAA Paper 2012-2707, AIAA Fluid Dynamics Conference, New Orleans, 25-28 Jun. 2012.
[28] Trumble, K. A., Schauerhamer, D. G., Kleb, W. L., Carlson, JR., Buning, P. G., Edquist, K. T., and Barnhardt, M. D., "An Initial Assessment of Navier-Stokes Codes Applied to Supersonic Retro-Propulsion," AIAA Paper 2010-5047, June 2010.
[29] Kleb, B., Schauerhamer, D.G., Trumble, K.A., Sozer, E., Barnhardt, M., Carlson, J.R., and Edquist, K.T., "Toward Supersonic Retropropulsion CFD Validation," AIAA Paper 2011-3490, Jun. 2011.
[30] Schauerhamer, D.G., Trumble, K.A., Kleb, B., Carlson, J.R., and Edquist, K.T., "Continuing Validation of Computational Fluid Dynamics for Supersonic Retropropulsion," AIAA Paper 2012-0864, Jan. 2012.
[31] Alkandry, H., "Aerodynamic Interactions of Propulsive Deceleration and Reaction Control System Jets on Mars-Entry Aeroshells," PhD Dissertation, University of Michigan, Dec., 2011.
[32] McDaniel, J.C., "Investigation of Laser-Induced Iodine Fluorescence for the Measurement of Density in Compressible Flows," PhD Dissertation, Stanford, Dec., 1981.
[33] Hiller, B., "Combined Planar Measurements of Velocity and Pressure Fields in Compressible Gas Flows using Laser-Induced Iodine Fluorescence," PhD Dissertation, Stanford, Nov., 1986.
[34] Fletcher, D.G., "Spatially-Resolved, Nonintrusive Measurements in a Nonreacting Scramjet Combustor Using Laser-Induced Iodine Fluorescence," PhD Dissertation, University of Virginia, Jan. 1989.

[35] Harfield, R.J., "Planar Measurement of Flow Field Parameters in Nonreacting Supersonic Flows with Laser-Induced Iodine Fluorescence," PhD Dissertation, University of Virginia, May, 1991.
[36] Donohue, J.M., "Experimental and Numerical Study of Ramp Injectors for Supersonic Fuel/Air Mixing," PhD Dissertation, University of Virginia, Jan. 1995.
[37] Staack, D.A., "Experimental Study of Interacting Rarefied and Continuum Flows using Planar Laser-Induced Iodine Fluorescence," M.S. Thesis, University of Virginia, Jan. 2001.
[38] Cecil, D.E., "Velocity Field Measurements in Rarefied, Hypersonic Flows of Nitrogen Using Laser-Induced Fluorescence of Iodine," PhD Dissertation, University of Virginia, Dec. 2011.
[39] Reed, E., Codoni J., McDaniel, J.C., Alkandry, H., Boyd, I.D., "Investigation of the Interactions of Reaction Control Systems with mars Science Laboratory Aeroshell," AIAA Paper 2010-1558, Jan. 2010.
[40] Codoni, J.R., Reed, E.M., McDaniel, J.C., Alkandry, H., Boyd, I.D., "Investigations of 4 Peripheral Propulsive Deceleration Jets on a Mars Science Laboratory Aeroshell," submitted to the Journal of Spacecraft and Rockets, Jul. 2012.
[41] Westblom, U., and Aldén, M., "Spatially resolved flow velocity measurements using laser-induced fluorescence from a pulsed laser," Optics Letters, Vol. 14, No. 1, 1989.
[42] Hirai, E., Teshima, K., Kurita, K., Takahara, S., "Velocity Measurement of Free Jets Using Nuclear Hyperfine Structure of I2," JSME International Journal, Series B., Vol. 40, No. 3, 1997.
[43] Munz, E.P., "The Electron Beam Fluorescence Technique," France: NATO-AGARD, AGARD-AG-132, December 1968.
[44] Humlíček J., "An efficient method for evaluation of the complex probability function: The Voigt function and its derivatives." Journal of Quantitative Spectroscopy and Radiative Transfer, Vol. 21, No. 4, pp. 309-313, April 1979
[45] Levine, I.N., *Molecular Spectroscopy,* New York, NY: John Wiley & Sons, 1975.
[46] Hiller, B., and Hanson, R.K., "Simultaneous planar measurements of velocity and pressure fields in gas flows using laser-induced fluorescence," Applied Optics, Vol. 27, No. 1, 1988.
[47] Hollo, S.D., Hartfield, R.J., and McDaniel, J.C., "Planar velocity measurement in symmetric flow fields with laser-induced iodine fluorescence," Optics Letters, Vol. 19, No. 3, 1994, pp 216-218.
[48] Cecil, D.E., "Planar Laser-Induced Iodine Fluorescence Measurements in Rarefied Hypersonic Flow Over a Reaction Control Jet Model in a Free Jet Wind Tunnel," M.S. Theis, University of Virginia, January 2004.
[49] Ashkenas, H. and Sherman, F.S., "The Structure and Utilization of Suerpsonic Free Jets in Low Density Wind Tunnels," Rarefied Gas Dynamics, Vol. 2, Academic Press, New York, 1966.
[50] DelVecchio, T. "Designing and Building a Hypersonic Wind Tunnel," Undergraduate Thesis, University of Virginia, Mechanical and Aerospace Engineering, 1999.
[51] Staack, D., McDaniel, J.C., Glass C.E., and Miller C., "Experimental Study of Interacting Rarefied and continuum Flows." AIAA Paper 2001-2762, Jun. 2001.
[52] Reed, E.M., "Planar Laser Induced Iodine Fluorescence for the Invesitgation of the Aerodynamics of Reaction Control System Jets on Mars-Entry Aeroshells," PhD Dissertation, University of Virginia, Dec. 2013.
[53] McDaniel, J.C., Codoni, J.R., Reed, E.M., Alkandry, H., and Boyd, I.D., "Propulsion Deceleration Studies using Planar Laser-Induced Iodine Fluorescence and Computational Fluid Dynamics," accepted to Journal of Spacecraft and Rockets, July 2012.

[54] Scalabrin, L.C. and Boyd, I.D., "Numerical Simulation of Weakly Ionized Hypersonic Flow for Reentry Configurations," AIAA Paper 2006-3773, June 2006.
[55] Martin, A., Scalabrin, L.C., and Boyd, I.D., "High Performance Modeling of Atmospheric Re-entry Vehicles," Journal of Physics: Conference Series, Vol. 341, 2012, Article 012002.
[56] Alkandry, H., Boyd, I.D., Reed, E.M., Codoni, J.R., and McDaniel, J.C., "Interactions of Single-Nozzle Sonic Propulsive Deceleration Jets on Mars Entry Aeroshells," AIAA Paper 2010-4888, June, 2010
[57] Reed, E., Codoni J., McDaniel, J.C., Alkandry, H., Boyd, I.D., "Investigation of the Interactions of Reaction Control Systems with Mars Science Laboratory Aeroshell," AIAA Paper 2010-1558, January 2010.
[58] Alkandry, H., Boyd, I.D., Codoni, J.R., Reed, E.M., and McDaniel, J.C., "Numerical Investigation Of Multi-Nozzle Propulsive Deceleration Jets for Mars Entry Aeroshells," Journal of Spacecraft and Rockets, Vol. 50, No. 6, 2013, pp. 1196-1206, 2012.
[59] Michael, J.B., Edwards, M.R., Dogariu, A., and Miles, R.B., "Femtosecond laser electronic excitation tagging for quantitative velocity imaging in air," Applied Optics, Vol. 50, No. 26, pp. 5158-5162, 2011.